ISSN-Printed: 2536-5010
ISSN-Online: 2536-5134

Volume 13, No 1, 2023

EJT

EUROPEAN JOURNAL OF TECHNIC

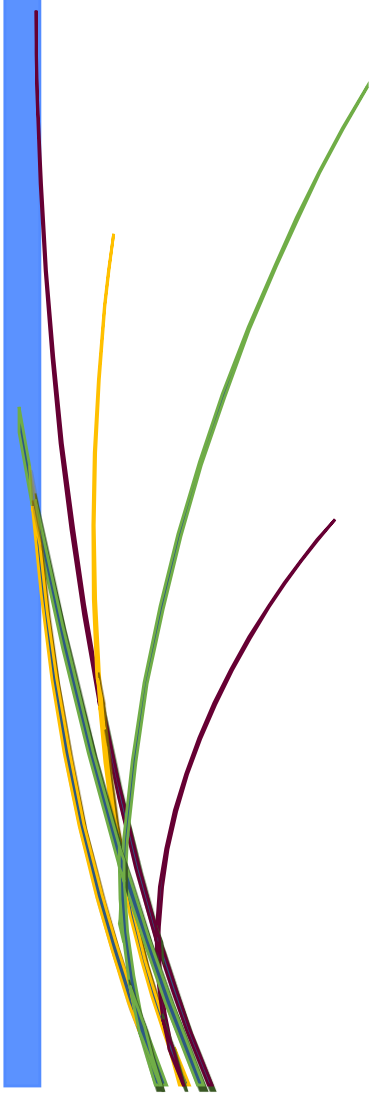

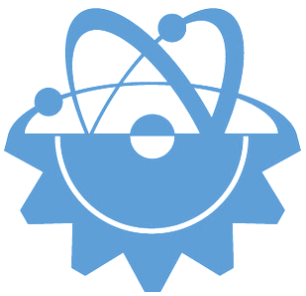

INESEG

Email (for orders and customer services enquiries): info@ineseg.org, ejt@ineseg.org
Visit our home page on www.ineseg.org

EUROPEAN JOURNAL OF TECHNIQUE (EJT)
ISSN-Printed: 2536-5010
ISSN-Online: 2536-5134

Scope: European Journal of Technique (EJT) established in 2010. It is a peer –reviewed international journal to be of interest and use to all those concerned with research in various fields of, or closely related to, Engineering disciplines. European Journal of Technique (EJT) aims to provide a highly readable and valuable addition to the literature which will serve as an indispensable reference tool for years to come. The coverage of the journal includes all new theoretical and experimental findings in the fields of Engineering or any closely related fields. The journal also encourages the submission of critical review articles covering advances in recent research of such fields as well as technical notes.

The scopes include:

- Mechanical Engineering
- Textile Engineering
- Electrical-Electronics Engineering
- Computer and Informatics Engineering
- Civil and Architecture Engineering
- Mining Engineering
- Chemical Engineering
- Metallurgical and Materials Engineering
- Environmental Engineering
- Food Engineering
- Geological Engineering
- Industrial Engineering
- Renewable Energy

EDITORIAL BOARD MEMBERS

Editor-in-Chief

- Musa YILMAZ

Publisher Of Journal

- Heybet KILIÇ

ETHICS and POLICIES

European Journal of Technique (EJT) is committed to following the Code of Conduct and Best Practice Guidelines of COPE (Committee on Publication Ethics). It is a duty of our editors to follow Cope Guidance for Editors and our peer-reviewers must follow COPE Ethical Guidelines for Peer Reviewers We expect all prospective authors to read and understand our Ethics Policy before submitting any manuscripts to our journals.

Please note that submitted manuscripts may be subject to checks using the iThenticate service, in conjunction with CrossCheck, in order to detect instances of overlapping and similar text.

The iThenticate software checks submissions against millions of published research papers, documents on the web, and other relevant sources. If plagiarism or misconduct is found, consequences are detailed in the policy.

The chief goal of our policy is threefold: to provide advice for our authors, to maintain the scholarly integrity of our journals and their content, and to detail the ethical responsibilities of EJT, our editors and authors.

We expect all authors to read and understand our ethics policy before submitting to any of our journals. This is in accordance with our commitment to the prevention of ethical misconduct, which we recognise to be a growing problem in academic and professional publications. It is important to note that most incidents of plagiarism, redundant publication, copyright infringement or similar occur because of a lack of understanding, and not through fraudulent intent. Our policy is one of prevention and not persecution.

If you have any questions, please contact the relevant editorial office, or European Journal of Technique (EJT)' ethics representative: ejtineseg@gmail.com

Download a PDF version of the Ethics and Policies [PDF,392KB].

Authors' Responsibilities

Authors should:

- Ensure that all researched work submitted is original, fully referenced and that all authors are represented accurately. The submission must be exclusive and not under consideration elsewhere.
- Provide accurate contact details for a designated corresponding author, who shall be deemed by the publisher and editor as fully responsible for the authorship of the paper and all communications concerning the ethical status and originality of the paper. This includes any queries or investigations that may arise, pre- or post publication.
- Openly disclose the source of all data and third party material, including previously unpublished work by the authors themselves. Anything that could compromise the originality of the submission should be expressly avoided and/or discussed with the editorial office in the first instance.
- Identify any third party material that they intend to include in their article, and obtain written permission for re-use in each instance from the relevant copyright holders. Such permissions should be submitted once the manuscript is accepted, or requires small changes to be accepted. For further guidance on seeking permission to use 3rd party material please see the Rights and Permissions section.
- Openly disclose any conflict of interest - for example, if publication were to benefit a company or services in which the author(s) has a vested interest.

- Expect to formally agree publication terms which defines the author and the publishers rights for the work. Visit our website for further information.
- Expect the editor to scan submissions using plagiarism detection software at iThenticate to check a paper's originality before sending out for review.
- Fully correspond and comply with the editor and publisher in any requests for source data, proof of authorship or originality in a timely manner, providing reasonable explanation for discrepancies or failures to disclose vital information.
- Fully co-operate with any consequent investigations if the editor and/or publisher are dissatisfied with the evidence available or the explanations provided.
- Expect transparency, efficiency and respect from the publisher and the editor during the submissions process.
- Remain in good communication with both the publisher and the editor.
- When necessary, submit corrigenda in a timely and responsible fashion.
- Co-operate fully with the publication of errata and with the retraction of articles found to be unethical, misleading or damaging.
- Remain in good communication with the editor(s), the publisher and any co-authors.

Editors' Responsibilities

Editors should:

- Read and understand COPE guidelines as well as EJT's ethics policy, and follow them during all editorial processes.
- Protect the reputation of their journal(s) and published work by only publishing content of the highest quality and relevance in a timely and responsible manner.
- Carry out thorough, objective and confidential peer review for original article submissions that pass the initial quality check and editorial assessment, in adherence with COPE guidelines and EJT' ethics policy.
- Detail and justify any article types which will not be peer reviewed (e.g. editorials, opinion pieces etc.).
- Provide a transparent review and publication process as far as is possible, with full respect and care paid to the author(s).
- Provide advice and give reasonable explanation and updates to authors during the submissions process and once a decision has been made.
- Allow authors the right to appeal any editorial decision.
- Only accept papers based on the original merit, quality and relevance of their content.
- Support authors in queries concerning the originality of their submissions and request the support of EJT if necessary.
- Advise the publisher of any third party material which has been included for which they do not believe sufficient permission has been cleared.

- Be ready and prepared to publish corrections, corrigenda, errata when necessary, as well as retract articles that (the editor and EJT) deem unethical, misleading or damaging.
- Remain in good communication with both the publisher and the author(s).

Reviewers' Responsibilities

Reviewers should:

- Adhere to EJT's policy of confidential peer review of their journals. This includes, but is not restricted to, keeping their identity hidden from authors and not externally distributing any work that is passed to them for their eyes only.
- Only accept invitations to review work that is relevant to their own expertise and speciality.
- Review submitted work in a responsible, impartial and timely manner.
- Report any suspected ethical misconduct as part of a thorough and honest review of the work.
- Avoid the use of unnecessarily inflammatory or offensive language in their appraisal of the work.
- Accept the commitment to review future versions of the work and provide 'follow up' advice to the editor(s), if requested.
- Seek advice from the editor if anything is unclear at the time of invitation.
- Remain in good communication with both the publisher and the editor.

EJT's Responsibilities

EJT will:

- Protect the reputation of our journals and published work by only publishing content of the highest quality and relevance in a timely and responsible manner.
- Provide detailed information concerning both our understanding of publication ethics and our implementation of the same. Emphasise a desire for prevention, not eventual detection, of ethical misconduct.
- Uphold our COPE membership (or of such similar organisations) and keep our editorial offices, publishing staff and society partners up-to-date with their guidelines and policies, adapting our own where appropriate (and publicising any update).
- When necessary, request proof of originality/accuracy from the corresponding author of any work submitted to any of our journals.
- Use plagiarism detection software when necessary for any submission to any journal at any stage of the submissions and publication process.
- Provide a transparent submissions and publication process, with full respect and care paid to the author. This includes detailed and dedicated instructions to authors for each journal, outlining referencing style, accepted article types and submission processes.
- Investigate thoroughly any suggestion of ethical misconduct detected during any stage of the submissions process. This can include, but is not restricted to, the following: plagiarism, redundant publication, fabrication or misuse of data and authorial disputes.

- When necessary, retract articles that we deem to be unethical, misleading or damaging.
- When necessary, publish errata, corrigenda and retractions in a timely and responsible fashion, detailing the decision online in an open access format and publishing in print as soon as possible.
- Remain in good communication with editors, authors, reviewers and society partners (where applicable).

Further reading

- Authorship of the paper: Authorship should be limited to those who have made a significant contribution to the conception, design, execution, or interpretation of the reported study.
- Originality and plagiarism: The authors should ensure that they have written entirely original works, and if the authors have used the work and/or words of others that this has been appropriately cited or quoted.
- Data access and retention: Authors may be asked to provide the raw data in connection with a paper for editorial review, and should be prepared to provide public access to such data.
- Multiple, redundant or concurrent publication: An author should not in general publish manuscripts describing essentially the same research in more than one journal or primary publication. EJT do not view the following uses of a work as prior publication: publication in the form of an abstract; publication as an academic thesis; publication as an electronic preprint. Information on prior publication is included within each EJT and its journal Guideline for Authors.
- Acknowledgement of sources: Proper acknowledgment.
- Disclosure and conflicts of interest: All submissions must include disclosure of all relationships that could be viewed as presenting a potential conflict of interest.
- Fundamental errors in published works: When an author discovers a significant error or inaccuracy in his/her own published work, it is the author's obligation to promptly notify the journal editor or publisher and cooperate with the editor to retract or correct the paper.
- Reporting standards: Authors of reports of original research should present an accurate account of the work performed as well as an objective discussion of its significance.
- Hazards and human or animal subjects: Statements of compliance are required if the work involves chemicals, procedures or equipment that have any unusual hazards inherent in their use, or if it involves the use of animal or human subjects.
- Use of patient images or case details: Studies on patients or volunteers require ethics committee approval and informed consent, which should be documented in the paper.

EJT has also accessed and learned from the existing policies of other publishers and leading experts as well as open access articles that detail and define ethical misconduct.

- 'Plagiarism and the law', Joss Saunders, Learned Publishing, 23:279-202: http://www.ingentaconnect.com/content/alpsp/lp/2010/00000023/00000004/art00002
- iThenticate Plagiarism Resources: http://www.ithenticate.com/resources/6-consequences-of-plagiarism

Publisher of Journal

Heybey Kilic Dicle University, Turkey / TU Delft, Netherland

Vol 13, Number 1, 2023
European Journal of Technique (EJT)
ISSN: 2536-5134

CONTENTS

European Journal of Technique

journal homepage: https://dergipark.org.tr/en/pub/ejt

Vol.13, No.1, 2023

Enhancing Algorithm Design Education: Interactive Learning with Jupyter Notebooks

Oguzhan Topsakal[1*]

[1*]Florida Polytechnic University, 33805, Lakeland, Florida, USA. (e-mail: otopsakal@floridapoly.edu).

ARTICLE INFO

Received: Jan., 04. 2023
Revised: Jun., 27. 2023
Accepted: Jun, 30. 2023

Keywords:
Algorithm
Design
Approach
Technique
Jupyter Notebook
Interactive
Teaching
Education
Learning

Corresponding author: *Oguzhan Topsakal*

ISSN: *2536-5010* | e-ISSN: *2536-5134*

DOI: https://doi.org/10.36222/ejt.1320404

ABSTRACT

Interactive learning environments play a crucial role in facilitating effective education. Traditional approaches to teaching algorithm design techniques often lack interactivity, resulting in a limited learning experience. In this article, we propose the utilization of Jupyter Notebooks, renowned for their versatility in combining code, visualizations, and explanations, as a powerful tool for enhancing understanding and promoting an engaging learning experience in teaching algorithm design techniques. We provide a comprehensive structure for a Jupyter Notebook page, encompassing problem descriptions, brute force solutions, algorithm design techniques, application areas, and references, to present a thorough solution for computer science problems using these design techniques. Our study includes experiments conducted with computer science students, demonstrating the practical application of Jupyter Notebooks in algorithm design education. Furthermore, we share sample Jupyter Notebooks for popular algorithm design techniques, including Divide & Conquer, Greedy, Dynamic Programming, and Backtracking. Importantly, we emphasize the significance of interactive comparisons between brute force solutions and algorithm design techniques, which foster valuable learning opportunities by providing insights into performance improvements, complexity analysis, validation, optimization strategies, trade-offs, and a deeper understanding of algorithmic principles. In conclusion, we propose the integration of Jupyter Notebooks as a potent tool for teaching algorithm design approaches, empowering learners to actively engage with the material, visualize complex concepts, and collaborate effectively. By incorporating Jupyter Notebooks into algorithm design education, instructors can enhance students' comprehension, cultivate critical thinking skills, and facilitate a profound understanding of algorithmic principles and optimization strategies.

1. INTRODUCTION

The famous quote, "Tell me and I forget, teach me and I may remember, involve me and I learn," underscores the pivotal role of interaction in effective learning. Algorithm design, being an abstract concept, is best taught through active involvement. Algorithm design approaches offer techniques for solving computer science problems, resulting in improved performance in terms of time complexity. [1,2] However, the conventional teaching methods employed in classrooms and textbooks primarily revolve around examples of computer science problems with limited or no interactive elements. [3] Consequently, much of the learning diminishes over time.

To address this issue, we propose the utilization of Jupyter Notebooks—an open-source web-based interactive computing environment—as a valuable tool for enhancing understanding and facilitating effective teaching of algorithm design approaches and time complexity analysis. [4] Jupyter Notebooks provide users with a flexible platform for creating and sharing interactive documents called notebooks. They support multiple programming languages, including Python, making them versatile for various data analysis and scientific computing tasks.

By leveraging the interactive and exploratory workflow offered by Jupyter Notebooks, learners can actively engage in running code snippets, visualizing results, and iteratively modifying their analyses. Jupyter Notebooks empower users to seamlessly combine code, visualizations, and explanatory text within a single document, fostering an interactive and comprehensive learning experience.

In this study, we have developed Jupyter Notebook pages that incorporate detailed descriptions, code implementations, and visualizations to present practical examples of algorithm design approaches (techniques). These notebooks serve as a powerful methodology for teaching algorithm design, enabling learners to actively participate in interactive sessions and gain a deep understanding of the approaches employed. We strongly believe that the adoption of Jupyter Notebooks as a standard

practice for teaching algorithm design will greatly enhance the educational experience and contribute to improved learning outcomes.

This article advocates for the use of Jupyter Notebooks as an invaluable tool to promote understanding of algorithm design approaches and time complexity analysis through interactive learning sessions. By offering a platform that integrates code, visualizations, and explanatory text, Jupyter Notebooks empower learners to delve into algorithmic problem-solving, fostering a deeper comprehension of the subject matter. It is our hope that the methodology presented here, employing Jupyter Notebooks for teaching algorithm design, becomes widely embraced to enhance the teaching and learning experience in algorithm design education.

2. RELATED RESEARCH

Efforts have been made to enhance algorithm teaching through the utilization of analogies and metaphors [5,6]. For instance, the book "Explaining Algorithms Using Metaphors" aims to equip teachers with metaphors and analogies to facilitate the comprehension of algorithmic concepts by students. [6] This comprehensive resource offers guidance on various subjects, including Graph Algorithms, Computational Geometry, and Strings and Sequences. Each subject is accompanied by background information, metaphorical explanations, analytical insights, teaching experiences, and relevant exercises.

In addition to algorithm teaching, Jupyter Notebooks have emerged as valuable collaboration and teaching tools across multiple disciplines, such as architecture [7], mathematics [8], and geography [9]. Castelo-Branco et al. proposed the utilization of Jupyter Notebooks in architecture to foster collaborative work and seamlessly integrate text, formulas, data, code, and graphics, thereby preserving the design narrative and supporting reproducibility [7]. Ketcheson highlights the benefits of Jupyter Notebooks in a Masters-level numerical analysis course, sharing detailed examples based on personal teaching experiences [8]. Similarly, Reades leveraged Jupyter Notebooks to teach geocomputation modules to Geography undergraduates [9].

Numerous educators have shared their best practices for utilizing Jupyter Notebooks in teaching [9-11]. Johnson critically examines the strengths and weaknesses of Jupyter notebooks for education, drawing on extensive experience teaching various courses, and provides a set of recommended best practices [10]. Leitão and Teixeira propose Jupyter Notebooks as a tool to foster the development of innovative teaching methodologies [11].

In the field of computer science, Jupyter Notebooks have also gained recognition and endorsement. For example, Liubschenko and Parkomenko explore the pedagogical and technical challenges of using notebooks as an educational tool, evaluating their effectiveness based on educational criteria such as complexity, interactivity, and utility [12]. Glick and Mache employ Jupyter Notebooks to create an open-access course on high-performance computing, reporting improved interactivity and enhanced outcomes [13]. Hamouda et al. develop interactive Jupyter Notebooks as a tool for teaching recursion, resulting in improved performance in recursion exam questions compared to students using traditional instruction methods [14]. Birster adopts individual Jupyter Notebook pages at different levels of Bloom's Taxonomy to enhance engagement among computer science students [15].

The widespread adoption and endorsement of Jupyter Notebooks across various disciplines, including computer science, reinforce its effectiveness as a versatile tool for teaching and collaboration. These experiences and best practices contribute to the growing body of evidence supporting the use of Jupyter Notebooks in educational contexts.

3. METHODOLOGY

This section outlines the methodology employed in teaching algorithm design approaches using Jupyter Notebooks. The algorithm design approaches are categorized into four main categories: divide & conquer, greedy, backtracking, and dynamic programming. A general description of each design approach and the corresponding steps involved in applying the approach is provided.

To exemplify the application of these design approaches, multiple Jupyter Notebooks were prepared, each focusing on a specific computer science problem such as traveling salesman, tug-of-war, longest common string, and closest pair of points. Each Jupyter Notebook page comprises several sections, including:

1. Introduction of the Computer Science (CS) Problem:
    - A comprehensive description of the problem,
    - Sample input and output cases,
    - Visuals, such as images or short videos, to depict the problem visually,
2. Brute Force Approach to Solve the CS Problem:
    - Description of the brute force solution
    - Visualization of the asymptotic complexity, showcasing the time required for executing the brute force algorithm as a function of the input size,
    - Graphical representations, such as Figure 1, demonstrating the time complexity of the brute force solution, e.g., O(n^2) for the 'Closest Pair of Points' problem,
3. Applying one of the Algorithm Design Approaches:
    - Step-by-step instructions to solve the computer science problem using the chosen algorithm design technique,
    - Visuals elucidating the algorithm design technique employed,
    - Pseudocode representing the solution using the design technique in plain English,
    - Python implementation code for applying the approach, including detailed comments for better comprehension,
    - Driver code with sample inputs, enabling the presentation of results on the Jupyter Notebook page,
    - Asymptotic complexity analysis of the solution, highlighting the time and space complexity optimizations achieved,

4. Application Areas of the CS Problem:
    - Identification and enumeration of the practical application areas associated with the computer science problem under consideration,
    - For instance, the 'closest pair of points' problem can find application in determining facility location optimization, enabling the selection of optimal locations for new facilities or services based on proximity to existing locations or customer demand,

Additionally, references to external resources are provided for further exploration and understanding of the computer science problem and the algorithmic approach utilized.

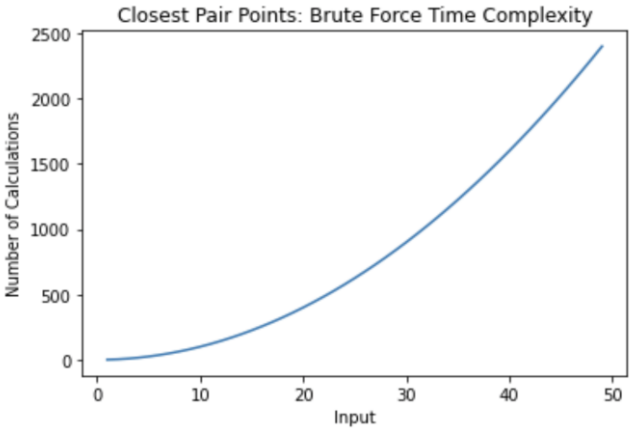

Figure 1. The asymptotic time complexity of brute force solution for the closest pair of points computer science problem.

The steps involved in each algorithm design approach category are summarized in Table 1. However, the steps might need to be tailored to the specific computer science problem being discussed. By offering detailed explanations, pseudocode, and Python implementation code, learners gain insights into the optimization strategies and techniques used to develop efficient algorithms. Moreover, the Jupyter Notebooks facilitate the visual representation of the problem, enabling learners to grasp the input-to-output transformation. The inclusion of the brute force solution as a baseline allows for comparative analysis, showcasing the improvements achieved through the algorithm design techniques.

The Python implementation of the algorithm for the given computer science problem is provided, utilizing the designated algorithm design technique. The implementation includes comprehensive code comments to enhance understanding and can be presented in one or multiple code cells within the Jupyter Notebook. Subsequently, a separate code cell encompasses the driver code, incorporating sample inputs. Upon running the driver code, the Jupyter Notebook page displays the resulting outputs. To analyze the algorithm's performance, the driver code can be executed with inputs representing increasing input sizes. The execution times for each input size can be recorded and plotted on a graph.

For example, Figure 2 illustrates the theoretical and experienced execution times for the Closest Pair of Points problem. The theoretical execution time (O(nlogn)) based on the input size, is depicted under the 'Ideal Graph' section at the bottom, and the experienced execution time is represented at the top of Figure 2. Similarly, Figure 3 presents the theoretical and experienced execution times for the Box Stacking problem.

This proposed structure of a Jupyter Notebook strives to present a comprehensive and interactive learning experience, allowing learners to understand algorithm design approaches and their practical application.

TABLE I
MAIN STEPS OF ALGORITHM DESIGN APPROACHES

Design Category	Steps
Divide & Conquer	**Divide**: Break down the problem into smaller, more manageable subproblems. **Conquer**: Solve the subproblems recursively or by applying a base case. **Combine**: Merge the solutions of the subproblems to obtain the final solution to the original problem.
Greedy Approach	**Initialization**: Set up the initial solution or state. **Determine the Greedy Choice**: Make the locally optimal choice at each step, assuming it will lead to a globally optimal solution. **Feasibility Check**: Verify if the greedy choice is valid. **Update**: Update the current solution with the chosen greedy choice. **Termination**: Determine when to stop and return the final solution.
Backtracking	**Choose**: Select a candidate for the current step or decision. **Constraints Check**: Verify if the chosen candidate satisfies the problem constraints. **Apply**: Apply the chosen candidate to the current step and move to the next step. **Recurse**: Recursively call the algorithm on the next step. **Backtrack**: Undo the previous step and go back to explore other candidates if the current candidate does not lead to a valid solution. **Termination**: Determine when to stop and return the final solution.
Dynamic Programming	**Determine the objective**: Clearly define the problem and determine the objective and constraints. **Identify Overlapping Subproblems**: Identify the subproblems that overlap or are repeated in the problem-solving process. **Formulate Recurrence Relation**: Define a recurrence relation that expresses the solution to a larger problem in terms of the solutions to its subproblems. **Create a Memorization Table or Array**: Set up a data structure to store the solutions to subproblems to avoid redundant computations. **Solve Bottom-Up or Top-Down**: Choose either a bottom-up or top-down approach to iteratively or recursively solve the problem by building on the solutions to subproblems. **Build the Final Solution**: Construct the final solution by combining the solutions to subproblems according to the recurrence relation.

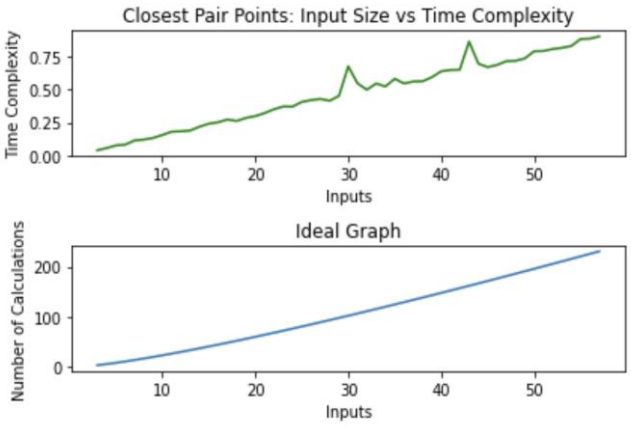

Figure 2. The theoretical and experienced execution times for the Closest Pair of Points problem.

Overall, this methodology empowers learners to actively engage with the material, experiment with different approaches, and acquire a deeper understanding of algorithmic principles and optimization strategies.

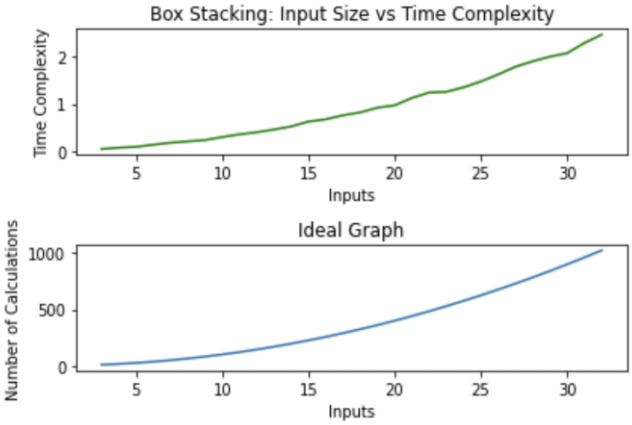

Figure 2. The theoretical and experienced execution times for the Box Stacking problem are presented on a Jupyter Notebook page.

4. EXPERIMENTS

In the algorithm design and analysis course, students specializing in Computer Science were instructed to select a computer science problem of their choice and employ one of the algorithm design techniques to present its solutions. To facilitate their presentations, the aforementioned sections were provided as a structured template, guiding the creation of Jupyter notebook pages. Some of the students granted permission to publish their refined Jupyter Notebook pages, which are now available on a dedicated website[1] [16].

Moreover, the website serves as a comprehensive resource, organizing well-known computer science problems into various algorithm design techniques. Each problem is accompanied by a concise description. The website's extensive list comprises a total of 118 computer science problems, with 27 categorized under dynamic programming, 41 under backtracking, 30 under divide and conquer, and 24 under greedy algorithms. This website aims to provide a valuable platform for showcasing the Jupyter Notebooks as a practical educational tool for algorithm design techniques in solving diverse computer science problems and to contribute to the academic community by fostering collaboration and sharing algorithmic insights.

5. DISCUSSION

Utilizing Jupyter Notebooks for teaching algorithm design approaches can significantly enhance understanding and facilitate the development and exploration of algorithms. Jupyter Notebooks provides an interactive environment where learners can write, execute, and modify code snippets in real-time. This allows the student to experiment with different algorithms, tweak parameters, and observe the immediate results. The interactive nature of Jupyter Notebooks promotes an iterative and exploratory approach to algorithm design. Jupyter Notebooks allow you to include rich text, markdown cells, and visualizations alongside your code. This helps provide detailed explanations, document the thought process, describe the algorithm steps, and include mathematical equations or diagrams to clarify concepts. The ability to combine code and explanations in a single document enhances understanding and promotes self-contained documentation. Moreover, Jupyter Notebooks support the integration of various data visualization libraries, such as Matplotlib or Seaborn. This enables you to visualize data, plot graphs, or display intermediate results during algorithm execution. Visualizations help you grasp patterns, observe algorithm behavior, and gain insights into the underlying data structures or problem-solving techniques. The implementation can be spread into various code cells, which can execute code cells step-by-step, observing the intermediate results at each stage. This is particularly useful for complex algorithms or iterative processes, allowing you to examine the algorithm's progress, verify intermediate computations, and identify any potential issues or bugs. Another great benefit of Jupyter Notebooks is enabling users to share them easily through cloud-based servers such as Google Colab, allowing for collaboration and knowledge exchange among colleagues, researchers, or instructors. The ability to collaborate and receive input from others can enhance your understanding and help refine your algorithms. Jupyter Notebooks also promote reproducibility by enabling others to reproduce your algorithms, verify your findings, or build upon your work.

The Jupyter Notebooks make it possible to review the theoretical and practical outputs of asymptotic complexity results side by side, as seen in Figure 2, and help to achieve a better understanding of the concepts. To better understand the asymptotic complexity, Jupyter Notebooks offer an interactive, visual, and collaborative learning experience. By combining code execution, visualizations, mathematical equations, explanations, and documentation in a single document, Jupyter Notebooks enhance your comprehension of complexity analysis concepts and provide a flexible platform for exploration, analysis, and sharing.

The proposed content for teaching algorithm design approaches via interactive Jupyter Notebooks encompasses sections to compare the brute force solution with the solution achieved by applying an algorithm design technique. Comparing the brute force solution with the solution achieved by applying an algorithm design technique provides insights into performance improvements, complexity analysis, validation, optimization strategies, trade-offs, and learning opportunities. It enables you to evaluate and appreciate the benefits of algorithm design techniques in solving computational problems efficiently and effectively. These benefits can be explained as follows:

- *Performance Evaluation*: By comparing the two solutions, you can assess the performance improvement achieved through the algorithm design technique. This includes evaluating factors such as execution time, memory usage, and overall efficiency. Comparing the performance metrics allows you to quantify the gains achieved by employing the algorithm design technique and determine its effectiveness in optimizing the solution.

[1] Interactive Examples of Algorithm Design Techniques: https://sites.google.com/view/algorithm-design-approaches/

- *Complexity Analysis*: Comparing the brute force solution with the algorithm design technique provides an opportunity to analyze the time and space complexity of both approaches. It helps you understand how the algorithm design technique reduces the computational requirements compared to the brute force solution. This analysis enhances your understanding of algorithmic efficiency and scalability based on the input size.
- *Validation and Verification*: Comparing the solutions helps validate the correctness of the algorithm design technique. By verifying that the results obtained from both approaches are equivalent, you can gain confidence in the correctness of the optimized solution. This verification process is crucial to ensure that the algorithm design technique produces accurate and reliable results and provides the expected efficiency.
- *Insight into Optimization*: Analyzing the differences between the brute force solution and the optimized solution offers insights into the optimization strategies employed by the algorithm design technique. You can identify the key optimizations or algorithmic improvements that lead to enhanced performance. Understanding these optimizations helps you grasp the underlying principles and techniques used to refine algorithms and improve efficiency.
- *Trade-offs and Constraints*: Comparing the two solutions allows you to explore trade-offs between various factors, such as time complexity, space complexity, accuracy, or implementation complexity. The brute force solution might provide a baseline that guarantees correctness but might not be feasible for larger problem instances due to its inefficiency. The optimized solution achieved through the algorithm design technique can offer a balance by addressing these constraints and providing a more practical solution.
- *Learning Opportunity*: The comparison between the brute force solution and the optimized solution can serve as a valuable learning experience. It helps you understand the importance of algorithmic efficiency, explore different algorithm design techniques, and appreciate the impact of optimizations on solving complex problems. By analyzing the differences and studying the optimized solution, you can enhance your algorithmic thinking and problem-solving skills.

6. CONCLUSION

In conclusion, the use of Jupyter Notebooks as a platform for teaching algorithm design is a valuable tool for enhancing understanding and promoting effective learning experiences. By combining code execution, visualizations, and explanations in a single document, Jupyter Notebooks offer an interactive and versatile environment for exploring algorithms and analyzing their asymptotic complexity.

We demonstrated how Jupyter Notebooks can be utilized to teach algorithm design approaches effectively. By categorizing the approaches into distinct categories and providing examples of Jupyter Notebook pages, learners are guided through the process of understanding and implementing different algorithmic techniques. The structure of the Jupyter Notebook pages, including problem description, brute force solutions, algorithm design techniques, application areas, and references, ensures a comprehensive learning experience.

The experiments conducted with computer science students further validate the efficacy of using Jupyter Notebooks for algorithm design education. The students' engagement in creating and presenting their own algorithmic solutions using Jupyter Notebooks showcases the benefits of interactive exploration, visualization, step-by-step execution, and collaboration. The integration of theoretical and practical outputs of asymptotic complexity analysis within the notebooks enhances learners' understanding of algorithmic concepts.

We also emphasize the importance of comparing brute-force solutions with algorithm design techniques. Such comparisons provide insights into performance improvements, complexity analysis, optimization strategies, and trade-offs. Learners gain a deeper understanding of algorithmic efficiency, scalability, and problem-solving techniques through this comparative analysis.

Overall, this article advocates for the broader adoption of Jupyter Notebooks in teaching algorithm design approaches. The interactive and collaborative nature of Jupyter Notebooks, along with their ability to integrate code, visualizations, explanations, and documentation, significantly enhance the comprehension and application of algorithmic concepts. By embracing Jupyter Notebooks as a pedagogical tool, educators can create a more engaging and effective learning environment, enabling learners to actively participate, explore, and master algorithm design approaches.

ACKNOWLEDGEMENT

We would like to thank Taylor Preston and Joshua Murphy for their help in editing selected Jupyter Notebooks and also thank Florida Polytechnic University Computer Science students who let their Jupyter Notebooks be utilized on this study's website.

REFERENCES

[1] Neapolitan, R., & Naimipour, K. (2010). Foundations of algorithms. Jones & Bartlett Publishers.
[2] Cormen, T. H., Leiserson, C. E., Rivest, R. L., & Stein, C. (2022). Introduction to algorithms. MIT press.
[3] Yadav, A., Gretter, S., Hambrusch, S., & Sands, P. (2016). Expanding computer science education in schools: understanding teacher experiences and challenges. Computer science education, 26(4), 235-254.
[4] Project Jupyter, https://jupyter.org/ (accessed Jun. 17, 2023).
[5] Forišek, M., Steinová, M. (2013). Explaining Algorithms Using Metaphors. Springer Briefs in Computer Science. Springer, London. https://doi.org/10.1007/978-1-4471-5019-0_1.
[6] Forišek, M., & Steinová, M. (2012, February). Metaphors and analogies for teaching algorithms. In Proceedings of the 43rd ACM technical symposium on Computer Science Education (pp. 15-20).
[7] Castelo-Branco, R., Caetano, I., Pereira, I., & Leitão, A. (2020, November). The collaborative algorithmic design notebook. In Int. Conf. of the Architectural Science Association (pp. 1056-1065).
[8] Ketcheson, D. I. (2014). Teaching numerical methods with IPython notebooks and inquiry-based learning. Proceedings of the 13th Python in Science Conference. Retrieved from http://hdl.handle.net/10754/346689.
[9] Reades, J. (2020). Teaching on jupyter. Region, The Journal of Ersa, 7(1), 21-34.
[10] Johnson, J. W. (2020, October). Benefits and pitfalls of jupyter notebooks in the classroom. In Proceedings of the 21st Annual Conference on Information Technology Education (pp. 32-37).

[11] Cardoso, A., Leitão, J., & Teixeira, C. (2019). Using the Jupyter notebook as a tool to support the teaching and learning processes in engineering courses. In The Challenges of the Digital Transformation in Education: Proceedings of the 21st International Conference on Interactive Collaborative Learning (ICL2018)-Volume 2 (pp. 227-236). Springer International Publishing.

[12] V. Liubchenko and H. Parkhomenko, "The Involvement of Jupyter Notebooks as an Educational Tools: A Case Study," 2021 IEEE 16th International Conference on Computer Sciences and Information Technologies (CSIT), LVIV, Ukraine, 2021, pp. 147-150, doi: 10.1109/CSIT52700.2021.9648674.

[13] Glick, B., & Mache, J. (2018). Using Jupyter notebooks to learn high-performance computing. Journal of Computing Sciences in Colleges, 34(1), 180-188.

[14] Hamouda, S., Edwards, S. H., Elmongui, H. G., Ernst, J. V., & Shaffer, C. A. (2018). RecurTutor: An interactive tutorial for learning recursion. ACM Transactions on Computing Education (TOCE), 19(1), 1-25.

[15] Birster, C. A. (2017). Engagement in Foundational Computer Science Courses Through Supplementary Content for Algorithms. arXiv preprint arXiv:1801.06047.

[16] Applications of Algorithm Design Approaches to Computer Science Problems Presented via Interactive Jupyter Notebook Pages, https://sites.google.com/view/algorithm-design-approaches/ (accessed June 17, 2023)

BIOGRAPHY

Oguzhan Topsakal received his B.S. in Computer Engineering in 1996 from Istanbul Technical University, Turkey. He received his M.S. and Ph.D. in Computer Science from the University of Florida in 2003 and 2007. After gaining extensive experience in the software industry, Dr. Topsakal is currently an assistant professor in the Computer Science department at the Florida Polytechnic University since 2018. He teaches courses related to Machine Learning, Algorithm Design, Databases, and Mobile Development. Dr. Topsakal's research interests include algorithm design and applications of machine learning and deep learning.

European Journal of Technique

journal homepage: https://dergipark.org.tr/en/pub/ejt

Vol.13, No.1, 2023

Increasing The Tensile Strength of Adhesive T-Type Joints with Bio-Inspired 3D Printed Inserts

Mirari Ğunav Geçit[1], Tolga Topkaya[2*]

[1] Batman University, Mechanical Engineering Department, Batman, Turkey. (mirarigecit@gmail.com)
[2*] Batman University, Mechanical Engineering Department, Batman, Turkey. (tolga.topkaya@batman.edu.tr)

ARTICLE INFO

Received: Feb., 24. 2022
Revised: Jan, 10. 2023
Accepted: Jan, 10. 2023

Keywords:
Adhesive
T-joint
Additive Manufacturing
3D Printing
Tensile Test

Corresponding author: *Tolga Topkaya*

ISSN: *2536-5010* | e-ISSN: *2536-5134*

DOI: https://doi.org/10.36222/ejt.1078345

ABSTRACT

In the present study, insert materials manufactured with a 3D printer were used to increase the strength of T-type adhesive joints, which have an important area of use in aviation and aerospace applications. Experiments were carried out for 3 different overlap lengths and bending radius values. In addition to the unreinforced samples, 4 different insert material designs were used for each overlap length: solid-reinforced model, hollow reinforced model, vertically reinforced model, and horizontally reinforced model. PLA was used as insert material and AL 5754 and 3M DP460 as adherend and adhesive respectively. As a result of the experiments, it was determined that the use of reinforcement material increased the joint strength significantly. It has been determined that the maximum strength increase was observed on the horizontally reinforced insert used sample.

1. INTRODUCTION

Joining process needed for combining materials to construct the structures. Different joining techniques can be used depending on application area and material type. While joining with rivets or bolts is preferred for the creation of heavy structures [1], [2], also, welding or soldering can be used for suitable materials [3]. Adhesive joints are preferred especially for low-weight applications and flat surface needs [4]. Different geometric designs are applied to increase joint strength because adhesive materials are weak against peeling stress. [5]. Temiz investigated bending behavior of bi-adhesively joined double strap joints [6]. Bahrami et al investigated the effect of notched adherends on the tensile strength of single lap adhesive joints [7]. Khaliki et al investigated the effect of joint geometry on the failure modes and behavior of sandwich T-joints [8]. Solmaz and Topkaya compared adhesively, pinned, and hybrid joints tensile strength [9].

Surface modifications can be applied to increase the bond strength. Adhered surface can be abraded with mechanical abraders [10] or laser etching technique can also be applied [11]. Cardoso et al. investigated the effect of surface pre-treatment on the strength of CFRP T-joints [12]. With the developing nano material technology, adhesive joint strength can be improoved with nano particles [13]. Çetkin investigated tensile strength behavior of graphene nano particle (GNP) and nano fiber reinforced adhesive joints [14]. Gholami et al. investigated fracture behavior of multi wallet carbon nano tube (MWCNTs) and graphene oxide nanoplatelets (GONPs) reinforced adhesive joints [15].

T and L type connections are preferred in applications where non-parallel adherends are joined. T-type and L-type connections are prone to complex stresses due to their geometry. Supports can be embedded in the adherends to minimize stresses [16]. The stress concentrations can be prevented, and joint strength increased in T-type and L-type connections with smoother transitions [17]. However, attention should be paid to the effect of filling materials on sample weight [18]. Barzegar et al. investigated bending behavior of T-type joints. They reported that increasing the fiber content on the adherends increased strength of samples [19].

In this study, tensile strength behavior of T-type joints investigated experimentally. For increasing the joint strength 3D printed inserts used in delta regions. 4 different insert designs and 3 different overlap lengths were used to investigate the effect of insert geometry. Aluminum alloy (AL-5754) and 3M DP460 two-part epoxy adhesive was used as adherend and adhesive materials respectively.

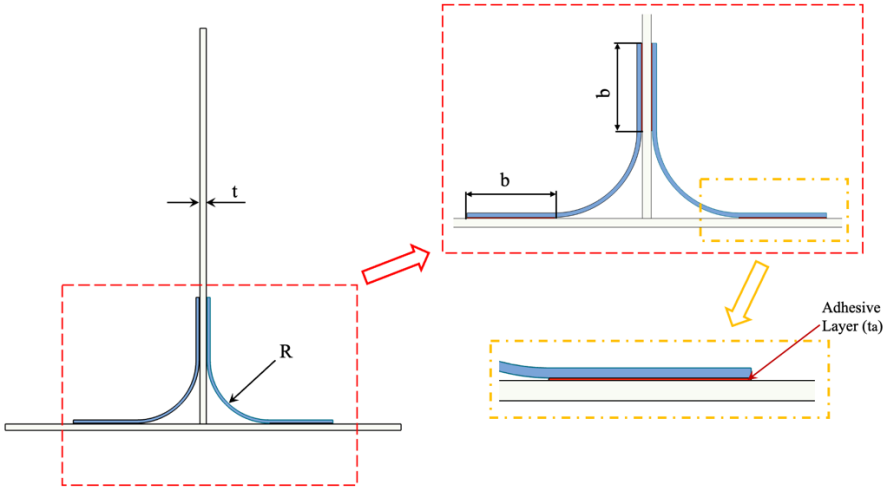

Figure 1. Dimensions of the test samples

2. MATERIALS AND METHODS

2.1. Materials and joint geometry

AL-5754 aluminum alloy was used as adherend material, and a two-part epoxy adhesive (DP460 from 3M) was used in the experiments. Mechanical properties of adherend and adhesive are given in table 1.

TABLE I
MECHANICAL PROPERTIES OF MATERIALS [20], [21]

Property	AL-5754	3M DP460 Adhesive
Young's Modulus (GPa)	70300	2077.1
Poisson's Ratio	0.33	0.38
Tensile Strength (MPa)	245	44.616

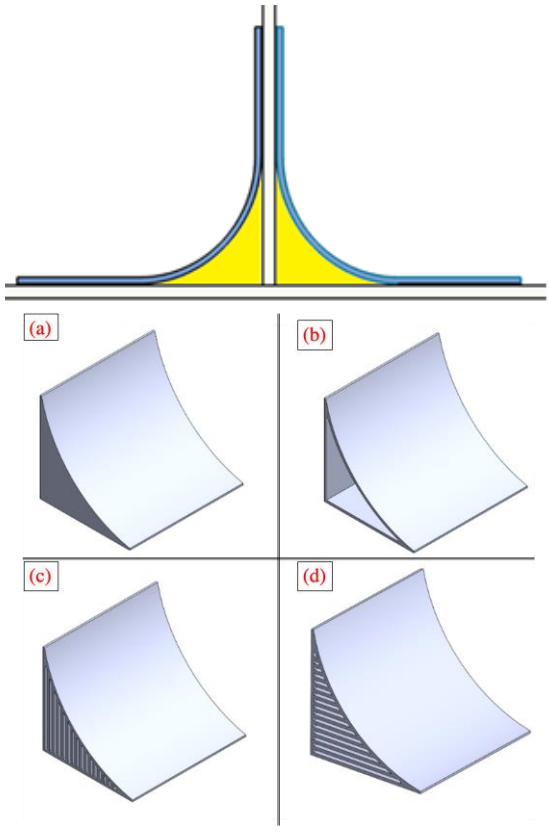

Figure 2. Delta regions and designed inserts a. solid reinforced model (SM) b. hollow reinforced model (HM) c. vertical reinforced model (VRM) d. horizontal reinforced model (HRM)

Four types of T-type joint have been used during the experiments. Dimensions of the T joints are given in Fig. 1 The dimensions of the vertical and horizontal adherends are identified as length (l=250 mm), thickness (t=2 mm) and width (w=25 mm). Adhesive layer thickness (ta) was selected as 0.25 mm. The dimensions of the support materials are defined as overlap length (b= 10, 20 and 30 mm), the bend radius (R= 5 mm, 10 mm, and 15 mm).

2.2. Joint preparation and Experiments

Bonding surfaces were abraded with using 180 grid sandpapers. Then, the adherends and the supports were cleaned of oil and dirt with acetone. After the acetone used has evaporated from the surface, the bonding process with adhesive is completed. In order to provide the sample dimensions, a mold produced with a 3D printer was used during bonding applications. The delta regions between the bending regions of the support materials and the horizontal and vertical adherends were filled with inserts produced with a 3D printer using PLA filament. 5 different connection models were produced: non-reinforced model (NM), solid-reinforced model (SM), hollow reinforced model (HM), vertically reinforced model (VRM), horizontally reinforced model (HRM).

For filling the delta regions four different inserts were designed and printed with Creality CR 10S Pro brand 3D printer. Printer settings were selected as 100 % for infill, 0.2 mm as layer height, and 50 mm/s as printing speed. Delta regions of T joint and designed insert materials are given in Fig. 2.

Samples were tested with Shimadzu universal testing equipment using 5 kN loadcell. The crosshead speed was selected as 1 mm/min. Test data was recorded at 10 Hz. For fixing the samples a homemade fixture was manufactured. The distance between lower support screws was selected as 125 mm. Every test repeated three times and average values used. Experimental setup is given in Fig. 3.

Figure 3. Experimental setup and application of the force

3. RESULTS AND DISCUSSION

Displacement as a function of applied force for different reinforcement material geometries of the samples with 10 mm overlap length and bending diameter samples is given in Fig. 4. Tensile failure load the of non-reinforced model (NM) was observed as 83.906 N. The failure load of the solid insert reinforced model (SM) is increased by 322% and it has 278.906 N value. Hollow insert reinforced models (HM) failure load is increased 645% according to the NM model and 542.031 N failure load is observed. The failure load of sample reinforced with vertically reinforced insert (VRM) is 588.594 N and the failure load of sample reinforced with horizontally reinforced insert (HRM) is 646.938 N. The damage load of VRM and HRM samples increased by 702% and 771%, respectively, compared to the NM sample. According to Burns et al., cracking starts at low load levels due to stress concentration in traditional samples, while bio-inspired T-joints have higher failure loads [22].

The applied force – displacement graph for different insert material geometries with a 20 mm overlap length and bending diameter is shown in Fig. 5. The NM has a tensile failure load of 77.031 N. Compared to the NM model, the failure load of the SM is increased by 440 %. HM, VRM, and HRM have tensile failure loads as 633.438 N, 772.66 N, and 858.906 N, respectively. Maximum failure load increase observed in HRM, the failure load increase is 1115% according to NM.

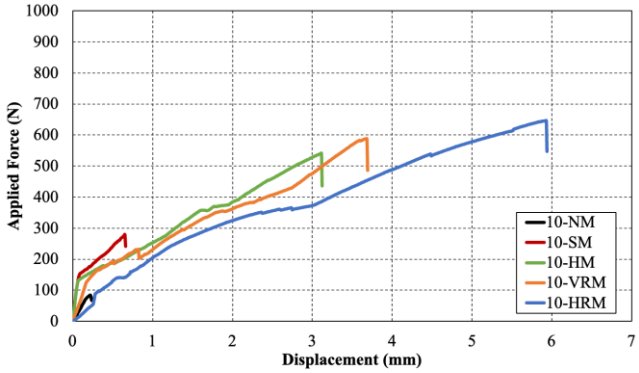

Figure 4. The effect of reinforcement material geometry on specimens' strength for 10 mm overlap length and radius diameter

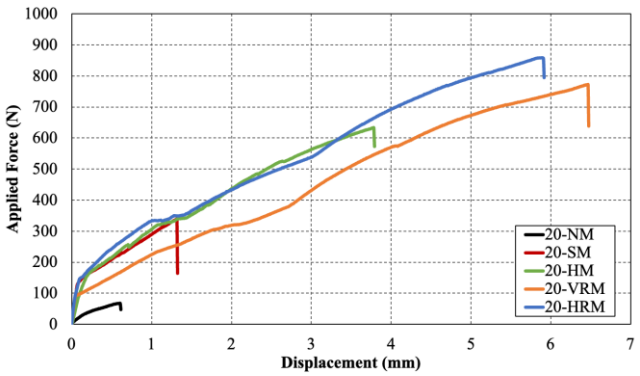

Figure 5. The effect of reinforcement material geometry on specimens' strength for 20 mm overlap length and radius diameter

Fig. 6 shows the applied force – displacement graph of 30 mm overlap length and bending diameter samples for different reinforcement geometries. Failure load of NM is observed as 63.125 N. failure loads for SM and HM are 498.438 N and 712.969 N respectively. The failure load of VRM is 910.938 N, and the failure load of HRM is 922.344 N. The damage load of VRM and HRM samples increased by 1443% and 1461%, respectively, compared to the NM sample.

Failure loads and sample weights are given in Fig. 7. Maximum sample weights are observed on SM while minimum sample weights are observed on non-reinforced samples. VRM and HRM models has same weights. Sample weights increased with increasing overlap length and bending diameter.

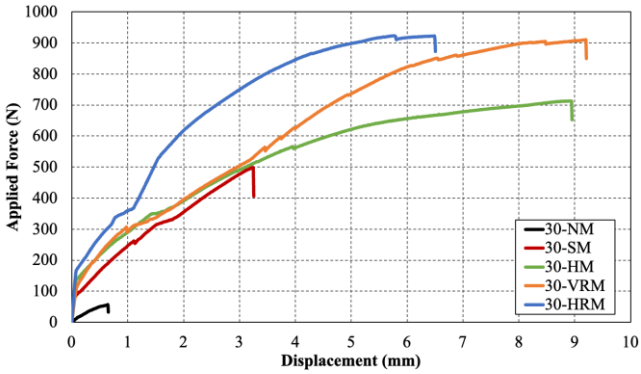

Figure 6. The effect of reinforcement material geometry on specimens' strength for 30 mm overlap length and radius diameter

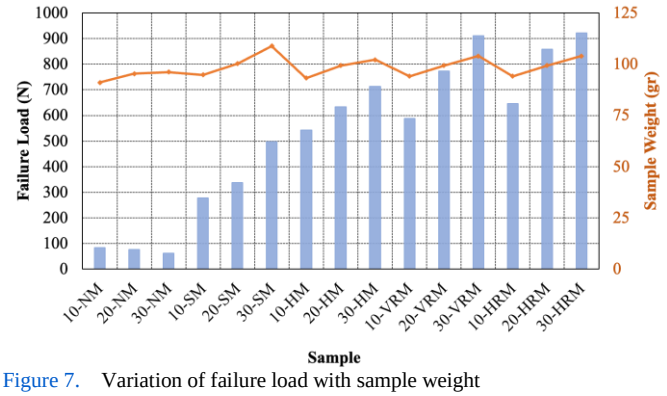

Figure 7. Variation of failure load with sample weight

Failure surfaces for non-reinforced model (NM) is given in Fig. 8. It has been determined that the main failure type is cohesion failure for all overlap lengths and bending diameters. Although adhesion failure was also observed in some parts of the joints, this type of failure was limited.

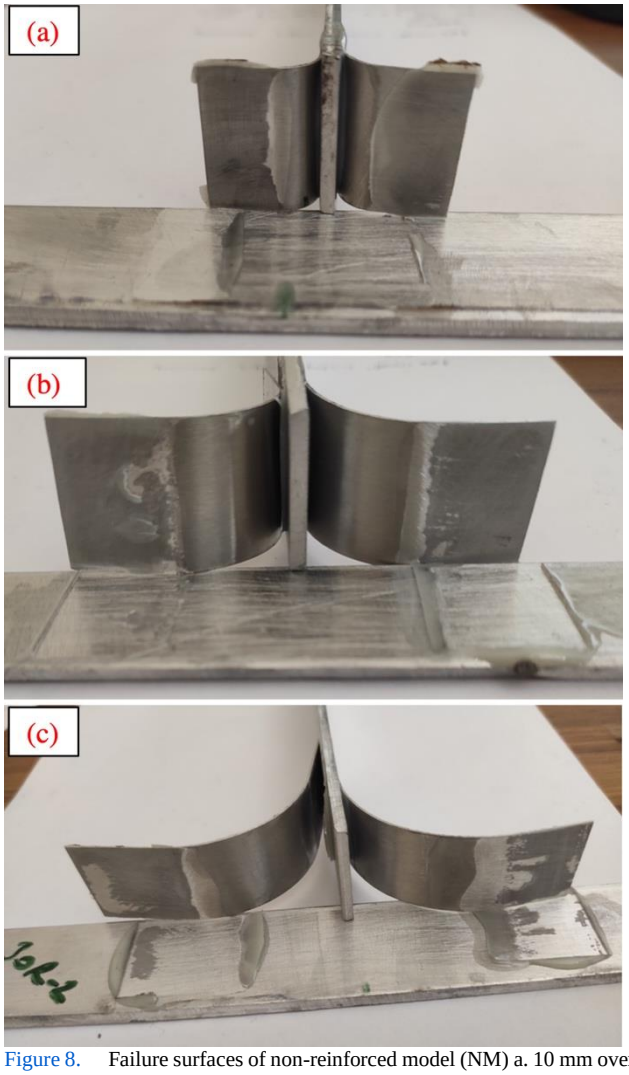

Figure 8. Failure surfaces of non-reinforced model (NM) a. 10 mm overlap length b. 20 mm overlap length c. 30 mm overlap length

Fig. 9 shows the failure surfaces of SM, HM, VRM and HRM with 20 mm overlap length. Cohesion failure is the main failure type for SM. It was determined that the adhesive material remained on the reinforcement material and separated from the aluminum adherend. This situation was evaluated to mean that the adhesive material adheres better to the reinforcing material. Cohesion failure was observed as main failure type for HM. There is minor damage on the insert material. The size of the damage seen in the insert material increased in HM samples with 20 mm overlap length and bend diameter. During the test, damage occurred on the left insert material, and then permanent joint failure occurred. In the specimen with 30 mm overlap length and bend diameter, both reinforcement materials on the right and left sides were damaged. If the thickness of the reinforcement material is higher than 0.25 mm, it is evaluated that the reinforcement material will not be damaged, and the joint strength will take higher values. Cohesion failure is observed as a main failure type for VRM samples. Adhesion failure type is also observed between reinforcement material and horizontal adherend interface for 30 mm overlap length and bending radius. It was observed that the main failure type was cohesion failure for 10 mm overlap length and bend diameter for HRM samples. In the sample with 20 mm overlap length and bend diameter, cohesion failure was observed in a limited area, while insert material damage was also observed. In the sample with 30 mm overlap length and bend diameter, it was determined that the adhesion failure covered a significant area, while the right insert material was damaged. Burns et al. reported that despite higher failure loads observed in bio-inspired samples, earlier onset of damage initiation [23].

No damage was observed in the 3D printed insert materials in any of the SM and VRM samples. The 3D printed inserts were damaged at all overlap lengths of the HM specimens. As the overlap length increased in the HRM specimens, the amount of damage seen in the 3D printed reinforcements increased.

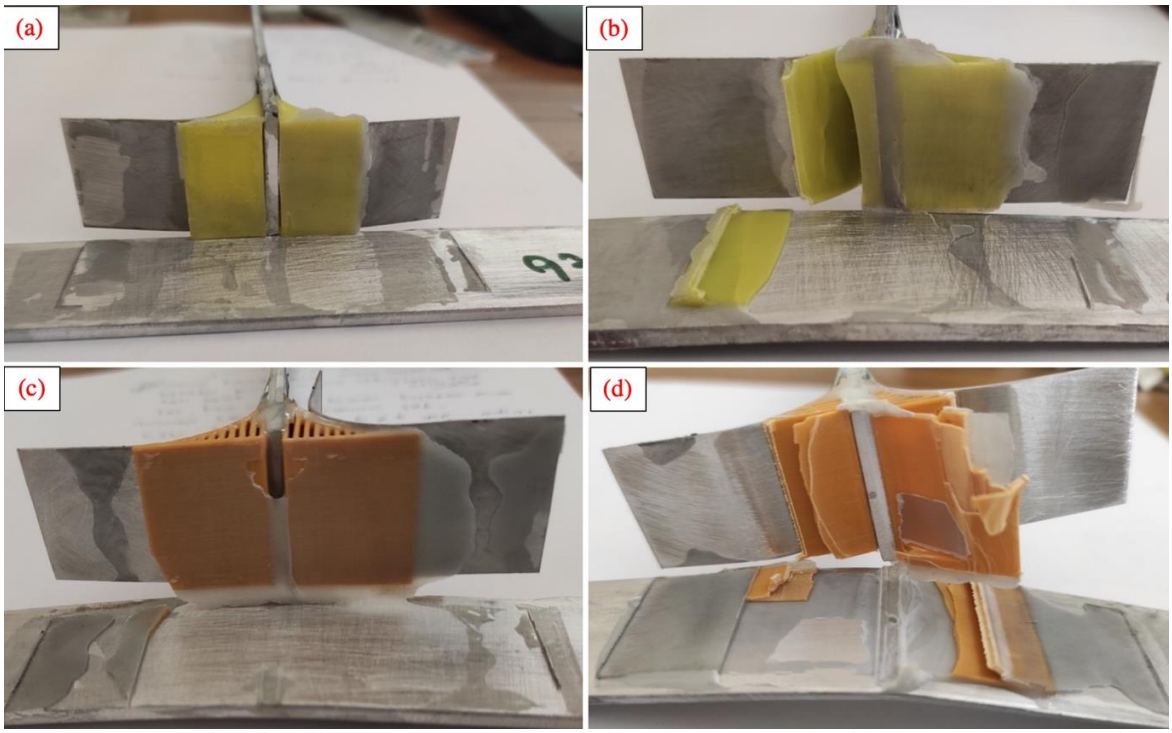

Figure 9. Failure surfaces for different insert designs a. solid-reinforced (SM), b. hollow reinforced (HM), c. vertically reinforced (VRM), d. horizontally reinforced (HRM).

4. CONCLUSION

Tensile strength of adhesive T-type joints with 3D printed inserts at the delta region were investigated experimentally. Following conclusions can be made according to limited studies results.

• In the samples without insert material, the strength of the sample decreased with increasing the overlap length and bend diameter. The increase of the bend diameter caused this situation by increasing the moment value in the adhesive layer.

• The specimen strength increased with increasing overlap length and bend radius in the samples with 3D printed inserts.

• The maximum increase in strength was observed in the samples with solid inserts compared to the non-reinforced samples with an overlap length of 30 mm and a bend diameter. The amount of increase is 790%.

• In the samples with hollow insert material, the increase for 10 mm overlap length and bend diameter is 646%, the increase for 20 mm overlap length and bend diameter is 822%, and the increase for 30 mm overlap length and bend diameter is 1130%.

• The highest increase in strength was observed in the samples with vertically and horizontally reinforced inserts The maximum failure load was observed in the sample with horizontally reinforced insert and 30 mm overlap length and bend diameter. This model provided a 1461% increase in strength compared to the non-reinforced model.

REFERENCES

[1] U. A. Khashaba, T. A. Sebaey, and A. I. Selmy, "Experimental verification of a progressive damage model for composite pinned-joints with different clearances," International Journal of Mechanical Sciences, vol. 152, pp. 481–491, Mar. 2019, doi: 10.1016/j.ijmecsci.2019.01.023.

[2] A. A. Abd-Elhady, S. Mousa, W. H. Alhazmi, H. E. M. Sallam, and M. Atta, "Effects of composite patching on cyclic crack tip deformation of cracked pinned metallic joints," Journal of Adhesion, vol. 97, no. 16, pp. 1561–1577, 2021, doi: 10.1080/00218464.2020.1803843.

[3] E. Çetkin, Y. H. Çelik, and Ş. Temiz, "Effect of welding parameters on microstructure and mechanical properties of AA7075/AA5182 alloys joined by TIG and MIG welding methods," Journal of the Brazilian Society of Mechanical Sciences and Engineering, vol. 42, no. 1, Jan. 2020, doi: 10.1007/s40430-019-2119-7.

[4] J. P. A. Valente, R. D. S. G. Campilho, E. A. S. Marques, J. J. M. Machado, and L. F. M. da Silva, "Geometrical optimization of adhesive joints under tensile impact loads using cohesive zone modelling," International Journal of Adhesion and Adhesives, vol. 97, Mar. 2020, doi: 10.1016/j.ijadhadh.2019.102492.

[5] M. A. Morgado, R. J. C. Carbas, E. A. S. Marques, and L. F. M. da Silva, "Reinforcement of CFRP single lap joints using metal laminates," Composite Structures, vol. 230, no. September, p. 111492, 2019, doi: 10.1016/j.compstruct.2019.111492.

[6] Ş. Temiz, "Application of bi-adhesive in double-strap joints subjected to bending moment," Journal of Adhesion Science and Technology, vol. 20, no. 14, pp. 1547–1560, 2006, doi: 10.1163/156856106778884262.

[7] B. Bahrami, M. R. Ayatollahi, M. J. Beigrezaee, and L. F. M. da Silva, "Strength improvement in single lap adhesive joints by notching the adherends," International Journal of Adhesion and Adhesives, vol. 95, no. June, p. 102401, 2019, doi: 10.1016/j.ijadhadh.2019.102401.

[8] S. M. R. Khalili, A. Ghaznavi, and A. Ghaznavi, "Effect of joint geometry on the behavior and failure modes of sandwich T-joints under transverse static and dynamic loads," Journal of Adhesion, vol. 91, no. 3, pp. 154–176, Mar. 2015, doi: 10.1080/00218464.2013.855881.

[9] M. Y. Solmaz and T. Topkaya, "Progressive failure analysis in adhesively, riveted, and hybrid bonded double-lap joints," Journal of Adhesion, vol. 89, no. 11, 2013, doi: 10.1080/00218464.2013.765800.

[10] A. Rudawska, "Selected aspects of the effect of mechanical treatment on surface roughness and adhesive joint strength of steel sheets," International Journal of Adhesion and Adhesives, vol. 50, pp. 235–243, Apr. 2014, doi: 10.1016/j.ijadhadh.2014.01.032.

[11] E. G. Baburaj, D. Starikov, J. Evans, G. A. Shafeev, and A. Bensaoula, "Enhancement of adhesive joint strength by laser surface modification," International Journal of Adhesion and Adhesives, vol. 27, no. 4, pp. 268–276, Jun. 2007, doi: 10.1016/j.ijadhadh.2006.05.004.

[12] J. v. Cardoso, P. v. Gamboa, and A. P. Silva, "Effect of surface pre-treatment on the behaviour of adhesively-bonded CFRP T-joints," Engineering Failure Analysis, vol. 104, no. June, pp. 1188–1202, 2019, doi: 10.1016/j.engfailanal.2019.05.043.

[13] İ. Saraç, H. Adin, and Ş. Temiz, "A research on the fatigue strength of the single-lap joint joints bonded with nanoparticle-reinforced adhesive," Welding in the World, vol. 65, pp. 635–642, 2021, doi: 10.1007/s40194-020-01063-2/Published.

[14] E. Çetkin, "Determination of the effects of GNP and nano-fibers on bonding joints," Journal of Manufacturing Processes, vol. 71, pp. 27–36, Nov. 2021, doi: 10.1016/j.jmapro.2021.09.013.

[15] R. Gholami, H. Khoramishad, and L. F. M. da Silva, "Glass fiber-reinforced polymer nanocomposite adhesive joints reinforced with aligned carbon nanofillers," Composite Structures, vol. 253, no. July, p. 112814, 2020, doi: 10.1016/j.compstruct.2020.112814.

[16] S. Akpinar, M. D. Aydin, Ş. Temiz, and A. Özel, "3-D non-linear stress analysis on the adhesively bonded T-joints with embedded supports," Composites Part B: Engineering, vol. 53, pp. 314–323, Oct. 2013, doi: 10.1016/j.compositesb.2013.04.049.

[17] R. Akrami, S. Fotouhi, M. Fotouhi, M. Bodaghi, J. Clamp, and A. Bolouri, "High-performance bio-inspired composite T-joints," Composites Science and Technology, vol. 184, no. September, p. 107840, 2019, doi: 10.1016/j.compscitech.2019.107840.

[18] L. A. Burns, A. P. Mouritz, D. Pook, and S. Feih, "Strength improvement to composite T-joints under bending through bio-inspired design," Composites Part A: Applied Science and Manufacturing, vol. 43, no. 11, pp. 1971–1980, 2012, doi: 10.1016/j.compositesa.2012.06.017.

[19] M. Barzegar, M. D. Moallem, and M. Mokhtari, "Progressive damage analysis of an adhesively bonded composite T-joint under bending, considering micro-scale effects of fiber volume fraction of adherends," Composite Structures, vol. 258, Feb. 2021, doi: 10.1016/j.compstruct.2020.113374.

[20] M. Y. Solmaz and T. Topkaya, "The flexural fatigue behavior of honeycomb sandwich composites following low velocity impacts," Applied Sciences (Switzerland), vol. 10, no. 20, 2020, doi: 10.3390/app10207262.

[21] İ. Saraç, H. Adin, and Ş. Temiz, "Experimental determination of the static and fatigue strength of the adhesive joints bonded by epoxy adhesive including different particles," Composites Part B: Engineering, vol. 155, no. July, pp. 92–103, 2018, doi: 10.1016/j.compositesb.2018.08.006.

[22] L.A. Burns, A.P. Mouritz, D. Pook, S. Feih, "Strength improvement to composite T-joints under bending through bio-inspired design" Composites: Part A, vol. 43 1971-1980, 2012, doi: 10.1016/j.compositesa.2012.06.017.

[23] L. A. Burns, A.P. Mouritz, D. Pook, S. Feih, "Bio-inspired design of aerospace composite joints for improved damage tolerance" Composite Structures, vol. 94 995-1004, 2012, doi: 10.1016/j.compstruct.2011.11.005.

BIOGRAPHIES

Mirari Ğunav Geçit obtained her BSc degree in mechanıcal engineering from Harran University in 2018. She received the MSc. diploma in Mechanical Engineering from the Batman University in 2021. Her research interests are solid mechanics, adhesive materials, additive manufacting and composite materials.

Tolga Topkaya graduated from Department of Mechanical Engineering at Fırat University in 2007. He gained his Ph.D. degree at the same university in 2017. He is working as Assistant Professor at Department of Mechanical Engineering, Batman University. He is a postdoctoral researcher in Aerospace Engineering Department at the University of Illiniois at Urbana Champaign. His main research fields are composites, biomechanics and adhesion and adhesives.

European Journal of Technique

journal homepage:https://dergipark.org.tr/en/pub/ejt

Vol.13, No.1, 2023

Efficiency Analysis in Solar Air Heaters with Attached Internal Fins

Fevzi GÜLÇİMEN[1], Hakan KARAKAYA[2], Aydın DURMUŞ[3]

[1*]Munzur University, Mechanical Engineering Department, Tunceli, Turkey.(e-mail: fgulcimen@gmail.com).
[2]Batman University, Mechanical Engineering Department, Batman, Turkey.(e-mail: hakan.karakaya@batman.edu.tr).
[3]Istanbul Aydin University, Department of Mechanical Engineering, 34295 Istanbul,Turkey.(e-mail: aydindurmus@aydin.edu.tr).

ARTICLE INFO

Received: Oct., 11. 2022
Revised: Jan, 26. 2023
Accepted: Jan, 26. 2023

Keywords:
Solar air heater
Exergy loss
Efficiency
Heat transfer

Corresponding author:*Hakan Karakaya*

ISSN:*2536-5010* | e-ISSN: *2536-5134*

DOI: https://doi.org/10.36222/ejt.1186879

ABSTRACT

In this study, an original solar air collector model, in which the flow environment was fixed with fins for three different angles at the flow channel's height, was designed. Fixing fins in the flow environment lengthens the flow channel since the fins prevent boundary layer formation in a flow channel. Apart from this, enlarged surface effect exists along with the effects of the fins, the air temperature at the outlet rises. The effects of fixed fins, for 30°, 45° and 60° angles, on the efficiency of collector were investigated. The collectors were made as standard collector sets with measurements 0.93x1.93 m^2 the flow channels of which have been modified. With the help of results obtained from the experiments, efficiency, Nusselt number, Reynolds number values were calculated; and they were compared to each other along with the literature. In the collectors designed for this study, it was observed that the heat transfer increased with the decrease of the fins angles.

1. INTRODUCTION

The systems aiming to increase fluid heat by employing solar energy are called solar collectors. Simply stated, the working principles of these systems can be described as follows: Some portion of solar radiation falling on a surface is absorbed by the collector itself. By means of the absorbed energy, heat transfer is made possible for fluids via convection and transmission. Furthermore, heat transfer occurs from the outer surface to the environment in connection with heat falling on the surface of collectors. The difference between this absorbed radiation and the heat lost to the given off to the environment is useful solar energy; and this energy is used to heat the fluid.

According to the type of fluid used, the collectors can be classified into two categories: fluid and gas collectors. While air is generally used in gas collectors, water (or water with antifreeze) is used in fluid collectors. When compared in terms of efficiency, water collectors are known to be more efficient than air collectors.

By using the passive method, it is aimed to increase collector thermal performance in air collectors that have different surface geometries considered for them. The thermal performance of the collector is known to improve when the flow channel of the heated fluid is lengthened or the turbulence effect in the flow channel is increased to increase the convection coefficient. Due to the physical properties of air, the thermal performance of available solar air collectors is poor. Solar air collectors are widely used for drying agricultural products and forest industry, building heating, and floor heating. A great many studies have been conducted on solar air collectors. In these studies, not only increasing the heat efficiency of the system but also decreasing its costs are taken into consideration.

Nomenclature

A_c	collector surface area (m^2)
c_p	specific heat (J/kg.K)
D_h	hydraulic diameter (m)
F_R	heat gain factor (-)
I	total solar radiation (W/m^2)
Nu	Nusselt number (–)
Q_u	useful heat gain (W)
Re	Reynolds number (–)
T	temperature (K)
T_s	surface temp. of the absorber (K)
U	channel perimeter exposed to air (m)
U_L	total heat loss coeff. of the collec.(-)
V	average velocity of air (m/s)
h	heat convection coefficient ($W/m^2.K$)
k	heat conduction coefficient (W/m.K)

η	efficiency of air collector (–)
m	mass flow rate of air (kg/s)
v	kinematic viscosity of air (m^2/s)

Subscripts

e	environment
i	inlet
o	outlet

Yeh and Lin (1996) investigated the changes between collector size and collector efficiency experimentally and theoretically in their studies for collectors in which air flow was on the black surface [1]. Parker et al. (1998) carried out experiments for three different collectors where air flow was on the absorber surface, under the absorber surface, or both on and under the absorber surface using V grooved absorber plates. In these studies, the heat performance and efficiency of collectors were examined [2]. In their studies, Yeh et al. (2002) conducted experiments for three different flow-rates and 5 different fin sizes in which there was air-flow under the absorber, and on the absorber; and both under and on the absorber. As a result of the experiments, they found the highest efficiency as 70% [3]. Paisorn and Kontragool (2003) investigated the heat transfer characteristics and thermal performances of 5 different planar collectors experimentally. In empirical results, while normal collectors had the lowest performance, the fifth model, with air inlet on the absorber and air outlet under the entrance, had the highest [4]. In his study, Ammari (2003) conducted experiments on thermal performance of a collector where air flow was from the side surface of the collector. Experiments revealed that the thermal efficiency for 50 lt/sec was 72% for four different flow rates [5]. Tyagi et al. (2007) carried out a study on parameters (exergy, ambient temperature, radiation value), which are effective on efficiency, for different flow-rates using instantaneous radiation values [6]. Karim and Hawlader (2004;2006) determined V grooved collector as the most efficient one in the study they improved and conducted on 3 different collectors, and they performed experiments on drying by means of these collectors [7-8]. Badran et al.(2008) conducted a study of convection coefficient between absorber surfaces and fluid pipes by means of a novel method they developed[9]. Hobbi et al.(2009) carried out experiments adding bent straps, springs, and conical parts to the flow environment to increase heat transfer, and observed significant increases in heat transfer [10]. Ramani et al.(2010) conducted experiments on a double pass air collector where absorber surface had pores [11]. El Sawi et al.(2010) carried out experiments on collectors in which the absorber surface was different. They found out that zigzag designed absorber surface had significant increases on heat efficiency [12]. Kurtbas and Durmus(2004), Akbulut and Durmus(2010), Karakaya and Durmus(2012)performed several experiments on drying by designing different collectors [13-15]. Nematollahi et al.(2014) investigated a dual function solar collector that combines air and water [16]. Akgul (2016) conducted thermal analysis for a novel solar air heater. The results show that conical springs improve thermal effectiveness [17].

Nima et al. (2017) investigated the impact of trying to add porous metal blocks to solar water collector risers in Iraq's climatic conditions. The beneficiary component was lower than the concinnity component for all simulations due to the insertion of the froth blocks, which also caused a significant increase in water pressure loss across the collector to roughly 153 percent [18]. By maintaining the pressure loss steady for various air mass and mass flow rates, Dabra and Yadav (2018) created a precise model in a JAVA simulation software to improve the distance and perimeter of concentric coextensive glass tubes (CCGT). Air flow input levels of 0.0053, 0.0074, 0.0095, and 0.0118 kg/s require more pumping power at high pressure losses [19].

Wenceslas optimized a flat-plate solar collector for thermosyphon solar water heaters (2019). Using the optimization results, a flat-plate solar collector was built using locally accessible materials. Additionally, it has been found that increasing the insulator's thickness to about 0.05 m causes a significant decrease in the heat loss portions and, as a result, an increase in the system's edge. The aluminum absorber plate would perform similarly to the bobby version if its thickness were increased to 0.005 m [20]. Farhan et al. (2022) created in MATLAB terra into predict the thermal and hydraulic efficiency of a V-groove solar air collector (VSAC) merged with transverse wedge-shaped caricatures (TWSR) underneath the absorption plate. When compared to the smooth configuration, the proposed design has a heat gain enhancement of around 9 and a highest rate of heat hydraulic efficiency of 9.6 when the mass in flow rate is 0.084 kg/s [21].

Goel et al. (2022) developed a better, smoother design for a parabolic trough solar collector (PTSC) that can help with a variety of exploration goals, including parametric advancements, energy performance, and enhancement. Furthermore, when compared to estimates from other models, the presented model is more appropriate than numerous other models and capable of thermos precise body. The suggested model is more truthful, comprehensive, less sophisticated, and acceptable over a broad selection than other designs. [22].

In this study, an original solar air collector model was designed whose flow environment was fixed with fins at three different angles and flow channel heights, was designed. The effects of fins fixed at 30°, 45° and 60° angles on efficiency and heat transfer were investigated.

2. EXPERIMENTAL SET

The heating unit, measurement unit, and control unit comprise the experimental set. Solar air collectors are used in the heating unit. The measurement unit is made up of a data collector and heat and speed probes that are linked to it. The control unit includes a fan for mass flowrate, an adjustable AC signal inverter, and a Pentium IV computer. Figure 1 depicts a schematic view of the experimental set as well as details.

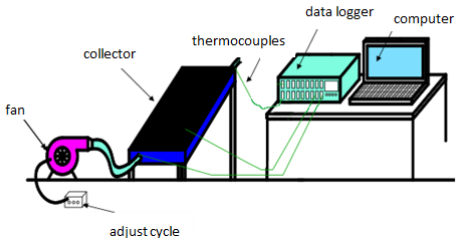

Figure 1. Experimental setup

Solar air collectors were used in the heating unit to heat the drying air. Normal collector measurements (0.93x1.93 m2) of solar air collectors were manufactured. (Figure 2). It was designed with a collector air flow channel height of 10 cm and fins fixed at the same height with 30º, 45º, and 60º angles, respectively.

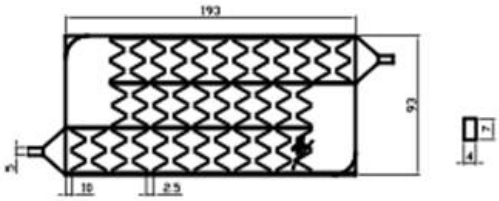

Figure 2. Flow environment and collector dimensions

The fins were separated by 10 cm. The surface of the absorber was made of 0.6 mm thick galvanized sheet. A transparent layer of 4mm in thickness glass was used to reduce the heat from the absorber plate. The sides and bottom of the collector were covered with 10 cm thick fiberglass isolator material. The absorber surface was painted matte black.

Figure 3 shows photos of the solar air collector and flow channel. Furthermore, the positions of angled fins fixed in the flow channel are clearly shown. Solar air collectors were built as standard collectors with 0.93x1.93 m^2 dimensions, but the flow channels were altered. Fins with three different angles at the flow channel's height were fixed in the collector's flow channel. Initially, the effect of fins fixed at 30º, 45º, and 60º angles on collector efficiency was investigated. It is necessary that the instantaneous radiation values belonging to the days when the experiments should be known in order that the collector efficiencies can be calculated. As a result, instant heating values were measured and recorded during the days when experiments were conducted using a Kipp-Zonen solar meter set at an angle of 38º. The temperature values were measured with the help of thermocouples fixed at 5 points in total, 3 of which were on the solar air collector, 1 of which was at the inlet, and 1 at the outlet of the collector. The temperature values were determined using T-type copper-constant thermocouples with a thickness of 0.5 mm.

At one end of the thermocouples, while the copper and constant ends were connected, connecting element ZA9000FST was mounted properly to the other end. The heat values were determined by connecting this element to an ALMEMO 5990-0 model data collector.

Figure 3. Flow environment and collector image

The heat values, which a data collector connected to a Pentium IV PC measured at 30 minute intervals, were then recorded into the computer. Pressure losses in the solar air collector designed for these experiments were also measured. Employing a FDA612MR model pressure module, pressure losses were obtained. Together with heat values, pressure loss values were determined for each flow rate of air mass.

The air mass flow rate to be heated was measured by adjusting the fan rotation speed. In order to change fan speed to the desired speed, a speed frequency convertor of the Telemecanique Altivar 31(ATV31HU15M2) type, with 1,5 kW power, 220 V entrance voltage, 50/60 Hz entrance frequency, 0.5 Hz and 500 Hz exit frequency intervals, and a nominal output current of 8 A, was used. The fan speed was changed according to the measured air speed using FVA645TH3 Thermo-anemometer flow sensor.

3. ANALYSES

3.1. Analysis of energy and efficiency

To heat the air, solar air collectors were used in the experiment. The air inlet-outlet temperature difference (T) in solar air collectors, which is well known, varies as follows;

$$(\Delta T) = f(V, I, A_c, \tau\alpha, F_R, U_L) \quad (1)$$

The linked and free parameters in equation 1 change in relation to various factors in their own right. The purpose of this research was to enhance collector efficiency using passive methods. In relation to variables, collector efficiency is expressed as follows:

$$\eta = \frac{Q_u}{I\,A_c} = \frac{F_R\,I(\tau\alpha) - F_R U_L (T_i - T_o)}{I} \quad (2)$$

The useful energy used to calculate collector efficiency, Qu, can be determined using the equation below:

$$Q_u = \dot{m} C_p (T_o - T_i) \quad (3)$$

If solar air collectors are regarded as heat convertors, literature comparison can be carried out for heat transfer. For this aim, it is essential that Nusselt number be fixed. As known, Nusselt number is equal to the heat gradient on the surface;

$$Nu = \frac{d\theta}{dy}\Big|_{y=collector} = \frac{hD_h}{k} \quad (4)$$

Equation 4 provides the amount of heat gain that it conveys due to the air mass flow rate. In addition, this equation is equal to the heat quantity obtained with regard to the air convection coefficient.

$$Q = hA_c LMTD = \dot{m}\, C_p \Delta T \quad (5)$$

Here, *LOSF* is the logarithmic heat difference. D_h and *LOSF*

are obtained via the following equations:

$$D_h = \frac{4\,A}{U} \qquad (6)$$

$$LMTD = \frac{(T_s - T_i) - (T_s - T_o)}{\ln\left(\frac{(T_s - T_i)}{(T_s - T_o)}\right)} \qquad (7)$$

In such systems, flow type has an important effect on heat transfer. Flow type is determined by means of a dimensionless Reynolds number.

$$Re = \frac{V\,D_h}{\nu} \qquad (8)$$

The average temperature ((To+Ti)/2) was used to calculate the external properties of air [13, 23-25].

3.2.Error Analysis

It is well known that the errors stem from constant errors, manufacturing errors, and random errors during the measurement of heat, speed, and pressure in the experiments of solar air collectors. In order that the total error of any parameter whose measurement is done can be determined, the total error value can be computed via equation 19 by taking constant errors, manufacturing errors, and random errors into consideration [14].

$$W = [(x_1)^2 + (x_2)^2 + \ldots\ldots\ldots\ldots (x_\infty)^2]^{1/2} \qquad (19)$$

The following results were calculated using the above equation.

Total error due to temperature measurement: (± 0.173 ºC)

Total error due to time measurement:

(±0.141 min.)

Total error from speed measurement:

(± 0.104 m/s)

Total error due to pressure measurement:

(± 0.0025 mbar) [13, 23-25].

4. RESULTS AND DISCUSSIONS

As previously stated, fins are fixed in the flow environment in such a way that they make 30º, 45º, and 60º angles in order to increase the collector's efficiency. As it is well known, fixing fins in the flow environment lengthens the flow channel by preventing the formation of a boundary layer in the flow channel. Aside from that, the enlarged surface effect exists due to the effects of fins, and as a result, the air outlet temperature rises.

Initially, at three different flow-rates, heat transfer experiments were conducted for all three collectors. The heating values belonging to the days, when collector experiments are carried out, are given in Figure 4. It is important to emphasize that experiments were performed for at least three days for each flow rate. On the other hand, comparisons were made for the days that provide approximately the same heating values and they are presented in this study.

As can be seen, between the dates of 8 – 23 August, the heating values in the Elazig region start at 450 W/m^{2}K at morning hours, and reach its peak value between 12-14 with nearly 760 W/m^{2}K. Radiation values begin to fall sharply after 16.00 p.m., and by 18.00, they are approximately 200 W/m2K.

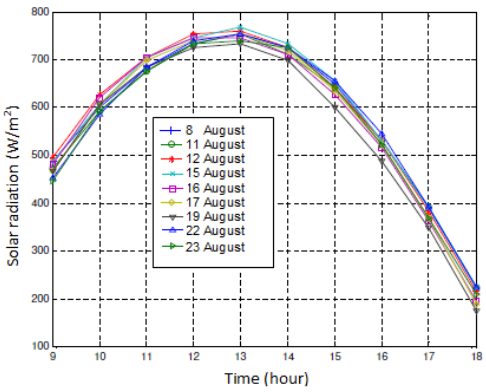

Figure 4. Variations in radiation values from day collector experiments were carried out according to the time of day.

Figure 5 shows the collector efficiency of 0.012 kg/s calculated from the data in Equation 2. As it can be seen, the fins angle and collector efficiency are directly proportional. Depending on the radiation values, the collector's efficiency ranges from 23.5% at 09.00 to 34% at 12.00 for α =60°. This maximum efficiency value obtained for α =30° becomes 42.5% for α =45° and 39% for α =60° becomes 34%, respectively.

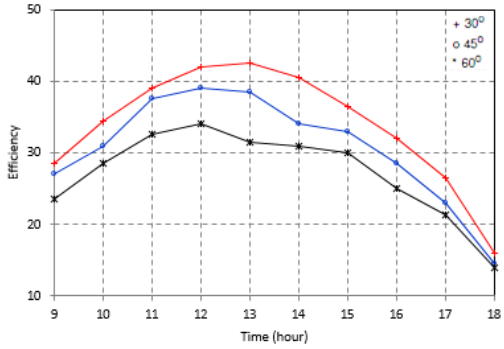

Figure 5. For ṁ = 0.012 kg/s, instant collector efficiency varies with time of day.

Considering the fact that the efficiency values of classical plane-plate solar collectors alternate between 20-25%, it is seen that the efficiency values obtained for collectors were significantly increased. If the mass flow rate is *ṁ = 0.026 kg/s*, maximum efficiency becomes 52% for α =30°, 45% for α =45°and 37% for α =60°, respectively.

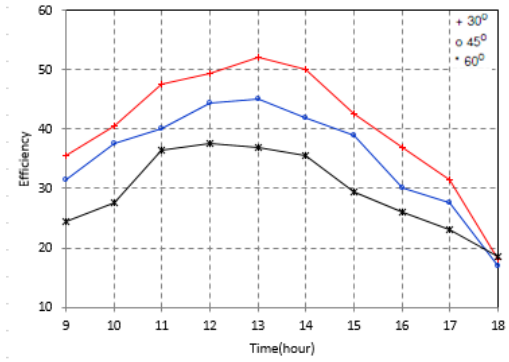

Figure 6. For ṁ = 0.026 kg/s, instant collector efficiency varies with time of day.

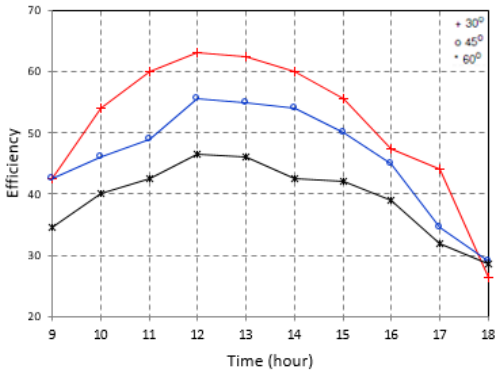

Figure 7. For$\dot{m}$ = 0.033 kg/s, instant collector efficiency varies with time of day

When Figure 6 and Figure 7 are examined, it will be observed that the efficiency value does not create a full parabola according to the hours of the day, and there are some deviations at some hours. This demonstrates that there are regional clouds on the days when the experiments are carried out. The maximum efficiency value obtained for α =30° becomes 63% for α =45° and 55.5% for α =60° becomes 46.5%, respectively.

This demonstrates the significance of incorporating a specific fin style into the collector flow channel. In other words, as the fin surfaces in the fixed flow environment become upright for flow direction, the collector efficiency increases at the same rate. If the effect of fins in the flow environment on air exit temperature is considered, it will be seen that as the fin angle is lessened, the collector efficiency increases. Figure 8 depicts the air entrance-exit rates and changes in collector surface temperatures throughout the day.

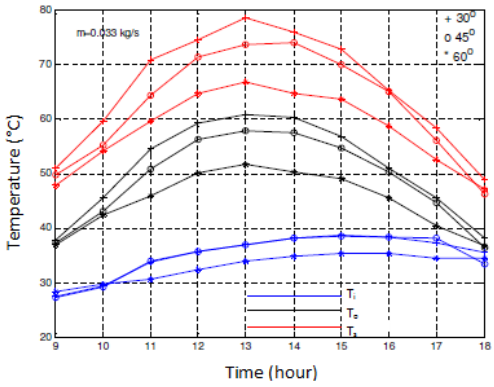

Figure 8. For $\dot{m}$ = *0.033 kg/s*, Temperature alterations according to time of day

When considering the energy balance of solar air collectors, the energy supplied to the system in unit time ($I.A_C$) accumulates on the collector's surface. In this system, with the increase in energy received (Q_u), decrease in the accumulating surface temperature is an anticipated physical behavior.

As previously stated, as the mass flow rate of air increases, so does the energy received from the system. As seen in Figure 9 and 10, there is an inverse relationship between energy gain from the system and collector surface temperature.

In other words, as the heat gain increases, the collector surface temperature decreases. This is valid for approximately equal radiation values. However, there is a direct correlation between heat gain and collector entrance-exit temperature difference (ΔT).

On the other hand, there is an inverse relationship between air mass flow rate and collector entrance-exit temperature.

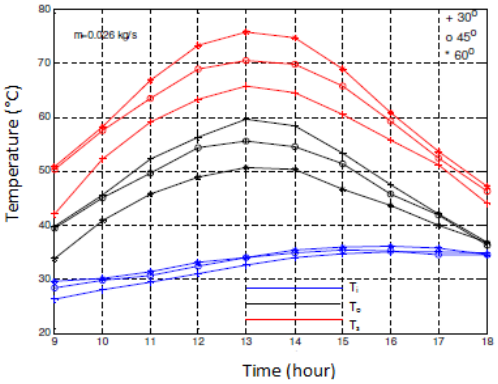

Figure 9. For $\dot{m}$ = *0.026 kg/s*, Temperature changes depending on the time of day

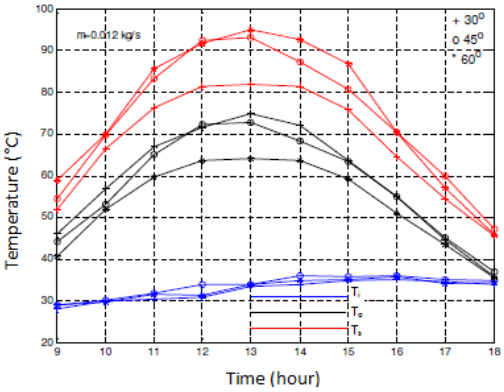

Figure 10. For $\dot{m}$ = *0.012 kg/s*, Temperature changes depending on the time of day

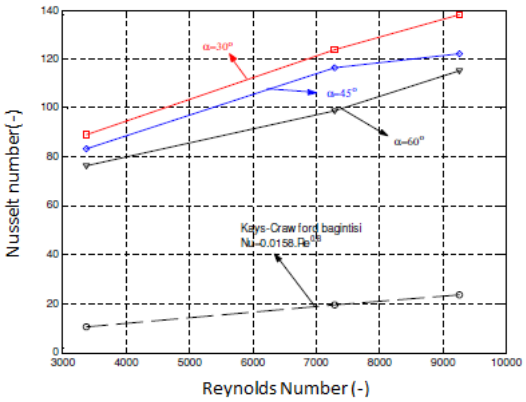

Figure 11. Change of average Nusselt number according to Reynolds number

As shown in Figure 11, the average Nusselt number Kays-Crawford equation is used for a channel with an isolated region on one side and a uniform heat flux on the other. Depending on the mass flow rate, the Reynolds number in the collector varies between 3371 and 9270. Depending on the Reynolds number, the Nusselt number changes between 76 and 115 for α=60° and between 83 and 121 for α=45° and between 89 and 138 for α=30°, respectively. As previously stated, as the Reynolds number increases, so does the effect of the fin angle.

In such systems, heat transfer can be increased at a significant rate by employing passive methods.

As is seen, the average Nusselt number increases approximately 5 times for α =60°, and almost 6 times for

α=45º, and nearly 6.5 times for α=30º in comparison to the theoretical Nusselt number.

As a result of the way the fins are placed in the collector, increased collector efficiency has been observed as the angle of the fins decreases. In addition, with the increase in flow rate, increased collector efficiency was observed.

In the experiments performed in the case of fins, the maximum efficiency was obtained as 63% for α =30°, $\dot{m}$ =0.033 kg/s, and the minimum efficiency was 34% for α =60°, $\dot{m}$ =0.012 kg/s.

Acknowledgement

The authors would like to express their gratitude to the **Frat University Research Foundation (FUNAF)** for their financial support.

REFERENCES

[1] H. Yeh, and T. Lin, "The effect of collector aspect ratio on the collector efficiency of upward- type flat-plate solar air heaters," Energy, vol. 21, no.10, pp. 843-850, 1996.

[2] B.F. Parker et al., "Thermal performance of three solar air heaters," Solar Energy, vol.13, no.7, pp. 543-547, 1998.

[3] H.M. Yeh, C.D. Ho, J.Z. Hou, "Collector efficiency of double-flow solar air heaters with fins attached," Energy, vol. 27, no.8, pp.715-727, 2002.

[4] N. Paisorn, and K. Bancho, "Theoretical study on heat transfer characteristics and performance of the flat-plate solar air heaters," International Comm. Heat Mass Transfer, vol. 30, no. 8, pp.1125-1136, 2003.

[5] H.D. Ammari, "A mathematical model of thermal performance of a solar air heater with slats," Renewable Energy, vol. 28, no.10, pp. 1597-1615, 2003.

[6] S.K. Tyagi et al., "Exergy analysis and parametric study of concentrating type solar collectors," International Journal of Thermal Sciences, vol.46, no.12, pp. 1304-1310, 2007.

[7] M.A. Karim, and M.N.A. Hawlader, "Development of solar air collectors for drying applications," Energy Conversion and Management, vol. 45, no. 3, pp. 329–344, 2004.

[8] M.A. Karim, and M.N.A. Hawlader, "Performance evaluation of a v-groove solar air collector for drying applications," Applied Thermal Engineering," vol.26, no.1, pp. 121–130, 2006.

[9] A.A. Badran et al., "On the measurement of bond conductance in solar collector absorber plate," Energy Conversion and Management," vol.49, no.11, pp.3305–3310, 2008.

[10] A. Hobbi, , and K. Siddiqui, "Experimental study on the effect of heat transfer enhancement devices in flat-plate solar collectors," International Journal of Heat and Mass Transfer," vol.52, no.19-20, pp. 4650–4658, 2009.

[11] B.M. Ramani, A. Gupta, R. Kumar, "Performance of a double pass solar air collector," Solar Energy, vol. 84, no.11, pp.1929–1937, 2010.

[12] A.M. El-Sawi et al., "Application of folded sheet metal in flat bed solar air collectors," Applied Thermal Engineering, vol.30, no.8-9, pp.864–871, 2010.

[13] İ. Kurtbas, and A. Durmus, "Efficiency and exergy analysis of a new solar air heater," Renewable Energy, vol.29, no.9, pp.1489-1501, 2004.

[14] A. Akbulut, and A. Durmus, "Energy and exergy analyses of thin layer drying of mulberry in a forced solar dryer," Energy, vol.35, no.4, pp.1754–1763, 2010.

[15] H. Karakaya, and A. Durmus, "Investigation of efficiency and exergy loss in plate heat exchangers having spiral surface profiles," Energy Educatıon Scıence and Technology, vol.28, no.2, pp.577-590, 2012.

[16] O. Nematollahi, P. Alamdari, M.R.Assari, "Experimental investigation of a dual purpose solar heating system," Energy Conversion and Management, vol.78, pp.359-366, 2014.

[17] M. Abuska, M.B. Akgül, "Experimental Study on Thermal Performance of a Novel Solar Air Collector Having Conical Springs on Absorber Plate" Arab J Sci Eng., vol. 41, pp.4509–4516, 2016.

[18] M.A. Nima, M.A. Ali, "Effect of Metal Foam Insertion on Thermal Performance of Flat-Plate Water Solar Collector Under Iraqi Climate Conditions," Arab J Sci Eng, vol. 42, pp. 4863–4884, 2017.

[19] V. Dabra, A. Yadav, "Effect of Pressure Drop and Air Mass Flow Rate on the Performance of Concentric Coaxial Glass Tube Solar Air Collector: A Theoretical Approach," Arabian Journal for Science and Engineering, vol. 43, pp. 4549–4559, 2018.

[20] K.Y. Wenceslas, T. Ghislain, "Experimental Validation of Exergy Optimization of a Flat-Plate Solar Collector in a Thermosyphon Solar Water Heater," Arabian Journal for Science and Engineering, vol. 44, pp. 2535–2549, 2019.

[21] A.A. Farhan, H.E. Ahmed, M.A. Mussa, "Thermal–Hydraulic Performance of a V-Groove Solar Air Collector with Transverse Wedge-Shaped Ribs," Arabian Journal for Science and Engineering, to be published. https://doi.org/10.1007/s13369-021-06442-5.

[22] A. Goel, G. Manik, , O.P. Verma, "Designing a Robust Analytical Model of a Parabolic Trough Solar Collector Through In-depth Analysis of Convective Heat Transfers," Arabian Journal for Science and Engineering, vol.47, pp.6535–6557, 2022.

[23] F. Gulcimen, "Drying of the mint and sweet basil with new designed air collectors and determining of drying parameters," PhD thesis, Institute of science, Firat University, Elazig, Turkey, 2008.

[24] F. Gülcimen, H. Karakaya, A. Durmus, "Drying of sweet basil with solar air collectors," Renewable Energy, vol. 93, pp. 77-86, 2016.

[25] F.P. Incropera, D.P. DeWitt, Fundamentals of Heat and Mass Transfer, Istanbul, Turkey: Literature Publications, 2001.

BIOGRAPHIES

Fevzi Gülçimen is M.Sc. and the Ph.D. degree in Mechanical Engineering from Fırat University, Institute of Science and Technology. His research interests are Renewable Energy Systems; Solar Energy Systems, Heat and Mass Transfer.

Hakan Karakaya currently Works as an Associate Professor at BatmanUniversity, Faculty of Engineering and Architecture. Major research interests are energy conversion, optimum insulation thickness, solar energy applications and heat and mass transfer.

Aydın Durmuş is presently working as Professor &Mechanical Engineering, Faculty of Engineering & Istanbul Aydin University, Turkey. He has more than 33 years of teaching and research experience. His research interest is Renewable Energy Systems; Clean Energy Systems, Heat and Mass Transfer, Energy Conservation, Solar Energy Applications; CFD, Environmental Engineering & Management. He has published more than 100 papers in International / National Journals and conferences.

European Journal of Technique

journal homepage: https://dergipark.org.tr/en/pub/ejt

Vol. 13, No. 1, 2023

Assessment of Risky Buildings according to the Regulation for Determination of Risky Buildings (RDRB 2019): The Case of Şanlıurfa

İsmail Ümit ÇIKMAN[1*], Mehmet Emin Öncü[2], Şermin KOÇYİĞİT[3]

[1*]Dicle University, Technical Sciences Vocational School, Diyarbakır,Türkiye. (e-mail: umit.cikman@dicle.edu.tr).
[2] Dicle University, Civil engineering Department, Diyarbakır, Türkiye. (e-mail: oncume@dicle.edu.tr).
[3] Dicle University, Technical Sciences Vocational School, Diyarbakır,Türkiye.(e-mail: sermin.kocyigit@dicle.edu.tr).

ARTICLE INFO

Received: Oct., 10. 2022
Revised: Feb, 03. 2023
Accepted: Feb, 27. 2023

Keywords:
Risky buildings
RDRB
Earthquake
Risk assessment

Corresponding author: *İsmail Ümit ÇIKMAN*

ISSN: *2536-5010* | e-ISSN: *2536-5134*

DOI: https://doi.org/10.36222/ejt.1187068

ABSTRACT

The majority of risky structures in Türkiye's building stock were constructed before 2000. It has been discovered that buildings constructed before the year 2000 lack engineering services and cannot fulfill the requirements of current regulations. Buildings constructed before 2000 are clearly incapable of providing the required performance and ductility in the event of an earthquake. Therefore, based on the Regulation for Determination of Risky Buildings (RDRB 2019), field studies were conducted on existing buildings built before 2000 in the Siverek district of Şanlıurfa. a two-stories reinforced concrete building designed in accordance with field study data was analyzed by following the risk analysis stages for low-rise reinforced concrete buildings in RDRB 2019. An elemental risk analysis was performed on 16 columns, which are vertical elements of the structure, and then a floor-based risk assessment was performed. As a consequence, it was concluded that the building designed in accordance with condition before 2000 was at risk.

1. INTRODUCTION

Türkiye is located in an active earthquake zone due to its geographical position. Since there are no ways for determining the precise time of earthquakes, our country will inevitably be impacted by natural disasters such as earthquakes, together with considerable loss of life and property. Türkiye is located on active fault zones such as the East Anatolian Fault (EAF), the North Anatolian Fault (NAF) and the Anatolian-Aegean Subduction Zone (AASZ) [1]. The Pacific Seismic Belt accounts for 81% of all earthquakes in the world, whereas the Alpine-Himalayan Seismic Belt accounts for 17% [2]. Because of its position, Türkiye is located on the Alpine-Himalayan Seismic Belt. The Earthquake Zones Map reveals that 92% of our country is in earthquake zones, 95% of our population lives with earthquake risk, 98% of large-scale industrial enterprises, and 93% of our dams are located in earthquake risk areas [3]. As a result of the major earthquakes that took place in our country, it has been shown that existing buildings in the regions are highly vulnerable to earthquake risk. [4] As a result, conducting risk assessments rapidly and efficiently is critical in order to figure out how this unsafe building stock might react to earthquakes. Otherwise, more catastrophic loss of life and property would be inevitable. Regulation for Determination of Risky Buildings (RDRB), which were initially published in 2013 and whose final version came into force in 2019, should be thoroughly investigated in this context, and existing building stocks should be evaluated within the scope of this regulation. Recent studies on this subject can be listed as follows. Ayhan and at all [5] made a risk assessment in the city center of Siirt and calculated the building performance scores in the light of the information obtained from 5 buildings whose demolition decision was taken by the administration. Considering the performance scores obtained for the 5 structures, they found that there was a 25 base score between the lowest and highest scores. The scores of the 2 buildings were the same, and the obtained scores determined that there was an important preliminary study in determining the risk priority in the buildings. Türkoglu and Atalay Meydanli [6] evaluated the seismic performance of Piyalepasa Mansion in Eregli as an example in their study. They created a three-dimensional analytical model of the building according to the measurements and observations made in situ. Considering the earthquake parameters selected specifically for the location of the building, the calculation methods defined in the regulations were applied. In the analyzes made, displacements and internal forces caused by the structure's own weight and earthquake forces were determined and compared

the earthquake safety of the building determined according to both regulations (RYTEIE and TBDY). In his study, Alicioglu [7] examined the buildings in Yunusemre and Sehzadeler districts of Manisa province according to RYTEIE. In the field studies of risky building detection, it has been determined that most of the building stock in the districts consists of reinforced concrete buildings built in 2000 and before. In line with the data obtained by examining the concrete compressive strengths, reinforcement classes, reinforcement layouts, column sizes and floor plans of 325 existing reinforced concrete buildings in the city center of Manisa, which were built between 1957 and 2001 within the scope of urban transformation, a prototype building representing the buildings in the city center of Manisa was created. He has determined the risk situations by conducting a survey of the prototype building and the buildings that have not been identified as risky buildings. With the risk assessment made for the prototype building, it has been determined that the existing reinforced concrete buildings with two or more floors carry earthquake risk. Turkel and Tekeli [8] made a risk assessment of 100 existing reinforced concrete residential buildings according to RYTEIE. The x and y directions of the buildings were analyzed with Sta4-Cad v.13, a ready-made package program used in the market. They envisaged five different material classes for each existing building: A, B, C, D and E. A total of 1000 buildings were analyzed. They determined the effectiveness of material properties in the risk assessment of reinforced concrete buildings. In addition, suggestions were made for risk assessment without the need for structural modeling and computer analysis. Using the Idecad software, Altın Karayahşi [9] investigated the earthquake resistance of 15 public buildings. Linear Performance Analysis and Risky Structure Analysis were used in the models under the impact of a four-way earthquake and found that the results in both analysis methods were similar. Korkmaz [10] carried out a risk analysis of a four-stories reinforced concrete structure using the Japanese Seismic Index Method (JSIM) and the RDRB 2013. The results of the two methods were compared, and similar and different sections were identified. The causes of the similarities and differences are discussed. Finally, Altın Karayahşi emphasized that the Japanese Seismic Index Method (JSIM) may be used in our country as well. Okuyucu and at all [11]. A total of 1194 reinforced concrete structures in the Palandoken district of Erzurum were examined, and as 18 of the structures had 8 floors or more, they were excluded from the scope of RYTEIE during the risk assessment phase. As a result of the statistical analysis of the building performance scores, the buildings were distributed to 5 different risk groups. They concluded that, according to RYTEIE, 7.2% of the 1177 reinforced concrete structures evaluated were high risk, 62.4% moderate risk, 7.3% low risk, 22% safe and 0.7% very safe. Ekinci [12] investigated an eight-stories building built in 1984 in Ankara using RDRB 2013. Ekinci conducted the benefit-cost analysis of the building based on urban transformation principles, and as a consequence of the analysis, it was decided to reconstruct the building, despite the fact that retrofitting was more cost-effective than rebuilding. In a study, Can [13] described the FEMA 310, ATC-21 (Rapid Visual Screening of Building for Potential Seismic Hazards), and Japanese Seismic Index Method (JSIM), all of which are rapid assessment methods, in general. On the other hand, Can thoroughly review the RDRB and the Earthquake Screening Method (ESM), and examined the results by taking into account a total of 20 risky and 2 risk-free buildings, including thirteen buildings constructed before 1975 and 7 buildings after 1975 according to RDRB, based on ESM. As a consequence, it can be determined that both methods produced similar results for reinforced concrete structures up to six-stories and that the ESM was more cost and time efficient. It can also be emphasized that, as a result of the preliminary work with the ESM, safe buildings would be separated and risky buildings would be prioritized. Isik and Tozlu [14] selected the ground classes, carrier system type and apparent building quality parameters of an existing five-storey reinforced concrete building as variables by using the first stage evaluation method, which is included in the principles regarding the identification of risky structures that entered into force in 2013 and according to these variables. Calculated building performance scores. They compared the calculated performance scores and interpreted the effects of the selected variables on the building performance scores. In their post-earthquake damage assessment studies on a building built in Kadıköy District of Istanbul Province in 1991, Hacımustafaoğlu et al., [15] used the rapid screening method and made observational analysis. As a consequence, they determined that the rapid screening method may be used in the identification of risky buildings in post-earthquake damage assessment studies, leading to fast and cost-effective identification. Gürbüz and Tekin [16] emphasized the necessity of determining the risk status of existing buildings in order to be prepared for an earthquake. In this framework, they calculated the performance scoring based on an imagined region on the map, in accordance with the regulation on the "Methods that Can Be Used to Determine the Regional Earthquake Risk Distribution of Buildings," which came into effect in 2013. Işık [17] compared the conditions that appeared utilizing the Japanese Seismic Index, Canadian Seismic Screening, and P25 Rapid Assessment methods to a school building that was entirely demolished in the 2011 Van earthquake. Işık and Tozlu [18] calculated the performance score and current status of an existing five-stories reinforced concrete structure based on the 1st Stage Assessment Method within the scope of RDRB, which went into effect in 2013. Risk analysis was carried out in the Siverek district of Şanlıurfa in this study. A low-rise reinforced concrete building was designed based on the average values obtained from the buildings. Following that, a risk assessment was done in accordance with the RDRB 2019, and the steps to be followed in risk assessment were thoroughly examined.

2. MATERIAL AND METHOD

The designed building was examined as a result of field investigations on existing buildings constructed before 2000 in the Siverek district of Şanlıurfa. The designed building comprises two stories and has a reinforced concrete frame system. The risk analysis was carried out in accordance with the steps determined for low-rise reinforced concrete buildings based on RYTEIE 2019. The risk assessment of the columns, which are represented as vertical elements, was completed first, followed by the risk assessment of the building on a floor-by-floor basis, in accordance with the obtained data and the analysis steps determined in RYTEIE 2019. If any floor was determined to be risky, the whole building was considered as risky.

2.1. General Information on the Inspected Building:

Table 1 shows general information about the building to be designed. A risk structure analysis was done based on the static project.

TABLE I
GENERAL INFORMATION OF THE DESIGNED BUILDING

Map Spectral Acceleration Coefficients	SS = 0.386 S1 = 0.135
Local Soil Class	ZA
Soil Bearing Coefficient	Ks=4000t/m³
Local Site Effect Coefficients	Fs = 0.800 F1 = 0.800
Design Spectral Acceleration Coefficients	SDS=SS×FS=0.386×0.800=0.309 SD1=S1×F1=0.135×0.800=0.108

For the building to be designed, the floor to be examined was assigned as the ground floor, and a survey was done on this floor. Another parameter, the carrier system knowledge level, was determined as a comprehensive knowledge level. The survey of the inspected building was carried out using various measuring devices, and Figures 1(a), (b), (c), and (d) show images of the survey processes.

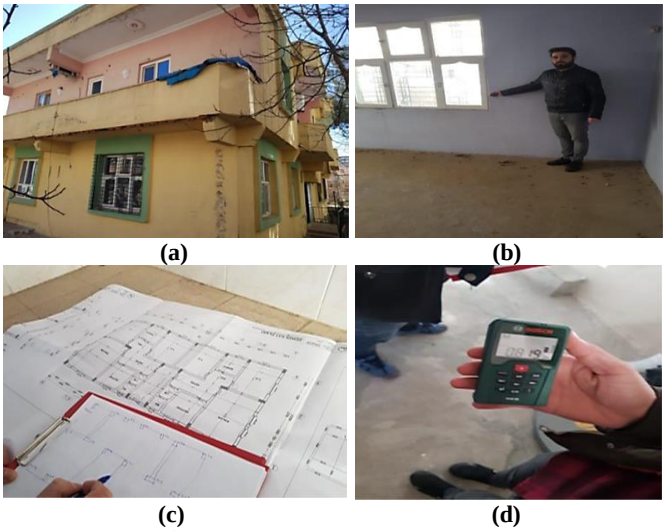

(a) **(b)** **(c)** **(d)**

Figure 1. Images of the survey process

To determine the reinforcements of the inspected building, X-ray scanning, a non-destructive method, was performed on six of the existing columns, and the reinforcement arrangement was determined by scratching half of these columns. Table 2 shows the identified reinforcements. Furthermore, the building's beams were 20 x 20 cm in size, and the reinforcements were 4 Ø 12 mm and Ø 8/25 mm, respectively.

TABLE 2.
COLUMN REINFORCEMENT RATIOS

Floor	No	Size (cm)	Longitudinal reinforcement (mm)	Stirrup (mm)	Compression	Corrosion
Ground	1	30X30	8 Ø 14	Ø 8/25	Non	Non
Ground	3	30X30	8 Ø 14	Ø 8/25	Non	Non
Ground	7	30X30	8 Ø 14	Ø 8/25	Non	Non

In order to determine the existing concrete strength of the building in Figure 2, a test hammer reading, which is a non-destructive examination method, was done from 8 different columns and concrete sampling was performed from 4 columns in Figure 3. Table 3 also shows the values of the core samples collected.

TABLE 3.
CORE VALUES OF THE BUILDING

Sample Name	Floor Location	Core Values (MPa)
Core 1	Ground Floor	7.84 MPa
Core 2	Ground Floor	7.35 MPa
Core 3	Ground Floor	6.69 MPa
Core 4	Ground Floor	7.54 MPa
Arithmetic Mean		7.36 MPa
Reduction Parameter (RDRB 4.1.11)		0.85
Conversion parameter mean current concrete value to be taken as Compressive Strength		6.63 MPa

Figure 2. Non-destructive examination method

Figure 3. Coring process

The calculation steps given in Table 4 were used for the analysis process of the designed building. Ecm: Existing concrete modulus of elasticity, (EI)e: Effective flexural stiffness, (EcmI)o: Flexural stiffness of gross section, fcm: Existing concrete compressive strength, Gcm: Existing concrete shear modulus.

TABLE 4.
CALCULATION STEPS TO BE USED FOR THE ANALYSIS

Effective bending stiffnesses	In beams: $(EI)e=0.3(EcmI)_0$ In columns: $(EI)e=0.5(EcmI)_0$
Concrete modulus of elasticity	$E_{cm}=5000\sqrt{fcm}=5000\sqrt{6.63}=12874.393$ MPa
Shear modulus	$G_{cm}=0.4Ecm=0.4x12874.393=5149.757$ MPa

The reinforcement class was determined as S220 for transverse and longitudinal reinforcements.

Figures 4a and 4b show the identification of the reinforcement diameter with a calliper and the identification of stirrup spacing with a tape measure on the scratched columns.

(a) **(b)**

Figures 4a and 4b. Images of the reinforcement identification processes

Figure 5 shows a three-dimensional view of a structure designed by us that is not exactly the same size and dimensions as the average values obtained.

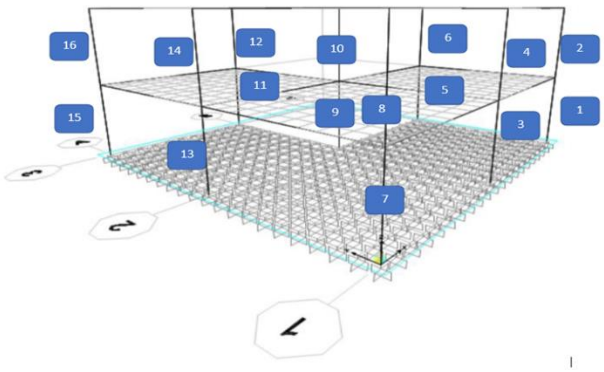

Figure 5. 3D view of the building with risk assessment

2.1.1. Risk Assessment of Colon No: 1

While identifying the risky building, the risk of the elements should be assessed first. The risk of the columns, which are expressed as vertical elements, was assessed for this purpose. As seen in column no:1, risk situations of the elements were calculated one by one. The examination steps are mentioned in the details below in this context.

Column (Ground Floor):

Axial Load Calculation:

The axial load of the column was obtained under (G+nQ+Ex/6) loading.

Nk: Column axial force obtained under vertical loads and reduced earthquake effects

n: 0.3 (live load reduction factor)

G (Dead load impact) = -66.684 kN,

Q (Live load impact) = -22.750 kN

Ex (Earthquake load effect) = -41.775 kN

Nk (G+nQ+Ex/6) = -80.427 kN

Calculation of Column Moments:

Internal forces were obtained under (G+0.3Q+Ex) loading at the upper and lower ends of the column.

Upper:

G_{22} = -7.455 kNm, G_{33} = -6.849 kNm

Q_{22} = -2.132 kNm, Q_{33} = -1.954 kNm

Ex_{22} = -1.319 kNm, Ex_{33} = -40.688 kNm

M_{22e} = (-7.455) + 0.3*(-2.132) + (-1.319) = -9.414 kNm

M_{33e} = (-6.849) + 0.3*(-1.954) + (-40.688) = -48.123 kNm

M_{22e}: (Column/wall moment around 2-2 axis under vertical loads and earthquake effects)

M_{33e}: (Column/wall moment around 3-3 axis under vertical loads and earthquake effects)

Lower:

G_{22} = 3.731 kNm, G_{33} = 3.344 kNm

Q_{22} = 1.060 kNm, Q_{33} = 0.961 kNm

Ex_{22} = -1.180 kNm, Ex_{33} = 113.171 kNm

M_{22e} = (3.731) + 0.3*(1.060) + (-1.180) = 2.869 kNm

M_{33e} = (3.344) + 0.3*(0.961) + (113.171) = 116.803 kNm

2.1.2. Calculation of Column Moment Capacities:

For the calculation of the moment capacities in the columns, firstly, the ratio of the internal forces obtained above to each other and the slopes of the lines for the upper and lower were found. The raw values of the capacity moments obtained under certain axial load values were then obtained. M_{22} and M_{33} capacity moments were determined for every 15 degrees between 0 and 90 degrees by interpolating based on the raw values obtained and the axial load (Nk) value we found. Table 5 shows the determined values, which were used to create an interaction diagram. Figure 6 shows the effect diagram. The coordinates of the intersections of the diagram and the lines give the column/wall plastic moments M_{22p} and M_{33p}.

Upper:

$$\tan\theta_d = M_{22}/M_{33} = -9.414/-48.123 = 0.1956$$

Lower:

$$\tan\theta_d = M_{22}/M_{33} = 2.896/116.803 = 0.0246$$

Table 5. M_{22p} and M_{33p} values corresponding to axial force for column no: 1

	M_{33}	M_{33}	M_{33}	M_{33}	M_{33}	M_{33}	M_{33}
P	0º	15º	30º	45º	60º	75º	90º
80.472	39.718	37.756	33.332	25.491	16.626	7.436	0
	M_{22}	M_{22}	M_{22}	M_{22}	M_{22}	M_{22}	M_{22}
P	0º	15º	30º	45º	60º	75º	90º
80.472	0	7.436	16.626	25.491	33.332	37.756	39.718

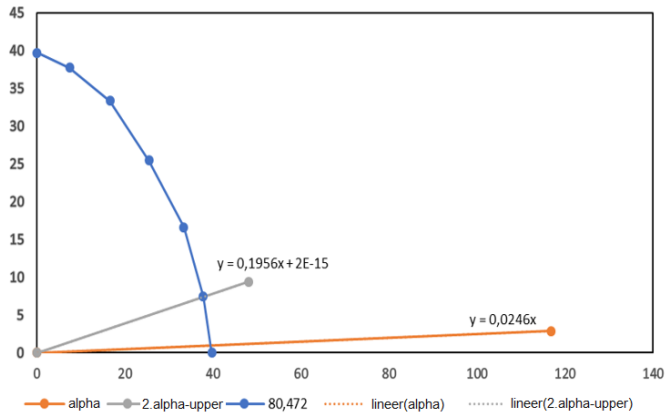

Figure 6. M_{22}-M_{33} interaction diagram for column no: 1

Upper	**Lower**
M_{22p} = -7.388 kNm	M_{22p} = 0.971 kNm
M_{33p} = -37.769 kNm	M_{33p} = 39.462 kNm

The Ve (Shear force calculated under vertical loads and earthquake effects) Calculation:

The shear force value was found as below by writing in situ in the combination of the internal forces (G+0.3Q+Ex/2) obtained.

G_{22} = -3.397 kN, G_{33} = -3.729 kN,

Q_{22} = -0.972 kN, Q_{33} = -1.064 kN

Ex_{22} = -51.286 kN, Ex_{33} = -0.047 kN

V_{22e} = (-3.397) + 0.3*(-0.972) + (-51.286/2) = -29.332 kN

V_{33e} = (-3.729) + 0.3*(-1.064) + (-0.047/2) = -4.072 kN

The Vr (Shear force of column, beam or wall section) Calculation:

$f_{ctm} = 0.35\sqrt{6.63} = 0.90$ MPa, $f_{ywm} = 220$ MPa, $c_c = 20$ mm, $A_{s22} = 151$ mm^2, $A_{s33} = 151$ mm^2
$S_{22} = S_{33} = 250$ mm (orta), b = 300 mm, $h_l = 300$ mm

(f_{ctm}: Existing concrete tensile strength, As: area of transverse reinforcement, fywm: Current yield strength of transverse reinforcement, Cc: Distance from the outer surface of the element to the outermost centre of longitudinal reinforcement, s: Spacing of transverse reinforcement, hı: Element length in 2-2 direction, b: element length in the 3-3 direction)

$\zeta = 1+0.07\ N_K/A_c$: column under compressive force (ζ: Column axial force factor)
$\zeta = 1+0.07\ N_K/A_c$: column under tensile force (A_c : Gross column cross-sectional area)

$$V_{22U} = 0.5 f_{ctm} b(h_ı - c_c)\zeta + A_{s22} f_{ywm} \frac{(hı - cc)}{s22} + V_{manto} \leq 0.22 f_{cm} b h_ı$$

$$V_{33U} = 0.5 f_{ctm} h_l (b - c_c)\zeta + A_{s33} f_{ywm} \frac{(hı - cc)}{s33} + V_{manto} \leq 0.22 f_{cm} b h_l$$

V_u: Uniaxial column/wall shear capacity

$0.22\ f_{cm} b h_ı = 131.274$ kN

$$V_{22u} = 0.5 * 0.90 * 300 * 280 * (1 + 0.07 * 80.472/90) + 151 * 220 * 280/250 = 77.372kN \leq 131.274kN$$

$$V_{33u} = 0.5 * 0.90 * 300 * 280 * (1 + 0.07 * 80.472/90) + 151 * 220 * 280/250 = 77.372kN \leq 131.274kN$$

V_{33u}=0.5*0.90*300*280*(1+0.07*80.472/90)+151*220*280/

250 = 77.372 kN ≤ 131.274 kN

$$V_r = V_{22u} V_{33u} = \sqrt{\frac{(V_{22e})^2 + (V_{33e})^2}{(V_{33u} V_{22e})^2 + (V_{33e} V_{22u})^2}}$$

$$V_r = 77.372 * 77.372 \sqrt{\frac{(-29.332)^2 + (-4.072)^2}{(77.372 * (-29.332))^2 + (-4.072 * 77.372)^2}} = 77.372kN$$

2.1.3. Ve Calculation (BA (Beam articulation) / CA (Column articulation) analysis):

In order to determine the beam articulation or column articulation in the column, first of all, the beam moments, M_{aki} values and directions of the beams connected to the column, calculated under 1.4G+1.6Q loading, were determined. The direction of the earthquake effect, Ex at that end of the beam is determined; if both are in the same direction, the plastic end moment of the beam can be taken $M_{pki} = M_{aki}$, but if they are in opposite directions, $M_{pki}=M_{aki}/3$. Then, M_{pkx} and M_{pky} values are determined, respectively, and then M_{pk22} and M_{pk33} values are determined according to the angle value.

Upper

$$M_{ak1} = -12.504kNm, \quad Ex \Rightarrow M_{pk1} = -12.504kNm$$

$$M_{ak2} = -14.153kNm, \quad Ex \Rightarrow M_{pk2} = -4.718kNm$$

$$M_{pkx} = -12.504kNm, \ M_{pky} = -4.718kNm$$

$$M_{pk22} = M_{pkx} \cos\theta - M_{pky} \sin\theta,$$

$$M_{pk22} = (-12.504)\cos 0 - (-4.718)\sin 0 = -12.504kNm$$

$$M_{pk33} = M_{pkx} \sin\theta + M_{pky} \cos\theta,$$

$$M_{pk33} = (-12.504)\sin 0 + (-4.718)\cos 0 = -4.718kNm$$

After these processes, the lower column upper-end moments and the upper column lower-end moments of the columns connected to the junction area are determined under the effect of the earthquake (Ex); then, the column/wall moment M_{22k} and M_{33k} values around the 2-2 and 3-3 axis transferred to the column/wall by the plastic articulation of the beams are obtained.

$$M_{22}^{upper} = -1.319kNm, \ M_{33}^{upper} = -40.688kNm,$$

$$M_{22}^{lower} = 4.435kNm, \ M_{33}^{lower} = 26.358kNm,$$

$$M_{22k} = M_{pk22} = \frac{\left|M_{22}^{upper}\right|}{\left|M_{22}^{üst}\right| + \left|M_{22}^{lower}\right|},$$

$$M_{22k} = -(-12.504)\frac{1.319}{1.319+4.435} = 2.866kNm$$

$$M_{33k} = M_{pk33} \frac{\left|M_{33}^{upper}\right|}{\left|M_{33}^{üst}\right| + \left|M_{33}^{lower}\right|},$$

$$M_{33k} = -4.718 \frac{40.688}{40.688+26.358} = -2.863kNm$$

Lower

Since there is a foundation connection and there is no beam, M_{22k} and M_{33k} values will be taken as M_{22p} and M_{33p} values.

$$M_{22k} = 0.971kNm$$
$$M_{33k} = 39.462kNm$$

The M_{22k} and M_{33k} values for the upper and lower ends are placed in the interaction diagram. Figure 7 shows the interaction diagram. If the values remain inside the diagram, beam articulation (BA) is identified; otherwise, column articulation (CA) is identified. As a result, if the BA condition is determined, the column end moments M_{22k} and M_{33k} will be used in the calculation, and if the CA condition is determined, the M_{22p} and M_{33p} values will be used in the calculation. Critical end moments of the upper and lower ends chosen based on the BA or CA status determined at the lower and upper ends, will be taken as $M_{22kr}^{\ upper}$, $M_{33kr}^{\ upper}$, $M_{22kr}^{\ lower}$, $M_{33kr}^{\ lower}$, respectively.

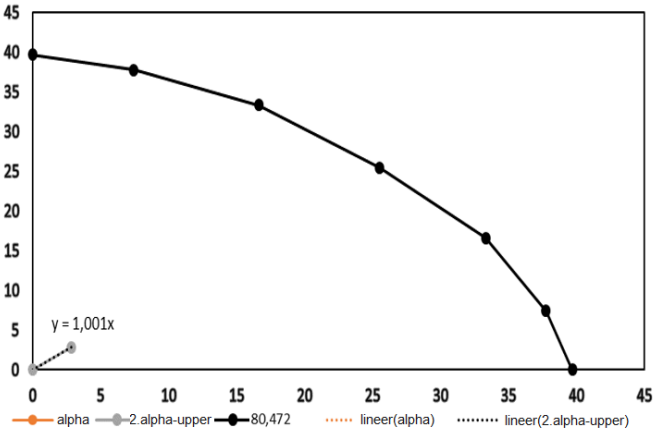

Figure 7. BA and CA status in M_{22} and M_{33} interaction diagram for column no: 1

M22k and M33k values at the upper and lower ends of the column were obtained as follows.

Upper End $M_{22k} = 2.866kNm$, $M_{33k} = -2.863kNm$, $M_{22p} = 20.794kNm$

Lower End $M_{22k} = 0.971kNm$, $M_{33k} = 39.462kNm$, $M_{22p} = 0.971kNm$

By comparing the M_{22k} and M_{22p} values obtained for the upper end of the column, it was determined whether the BA or CA was determined. Since there is no beam at the lower end, the CA situation was directly examined.

Upper End

$M_{22p} = 20.794kNm > M_{22k} = 2.866kNm (BA)$

Lower End Kiriş bulunmamaktadır. **(CA)**

$M_{22kr}^{upper} = 2.866kNm$, $M_{33kr}^{upper} = -2.863kNm$, $M_{22kr}^{lower} = 0.971kNm$, $M_{33kr}^{lower} = 39.462kNm$,

$$V_{22e} = \frac{\left|M33_{kr}^{upper}\right| + \left|M33_{kr}^{lower}\right|}{\ell n}$$

$$V_{33e} = \frac{\left|M22_{kr}^{upper}\right| + \left|M22_{kr}^{lower}\right|}{\ell n}$$

ℓn: Beam net length or column net length

Critical end moments of selected upper and lower ends were respectively M_{22kr}^{upper}, M_{33kr}^{upper}, M_{22kr}^{lower}, and M_{33kr}^{lower} as above.

$$V_{22e} = \frac{2.863+39.462}{2.8} = 15.116kN$$

$$V_{33e} = \frac{2..866+0.971}{2.8} = 1.370kN$$

Vr Calculation (BA/CA Analysis):

$f_{ctm} = 0.35\sqrt{6.63} = 0.90\ MPa$, $f_{ywm} = 220MPa$, $c_c = 20mm$

$A_{s22} = 151mm^2$, $A_{s33} = 151mm^2$,

$S_{22} = S_{33} = 250mm$ $(middle)$, $b = 300mm$, $h_1 = 300mm$

$\zeta = 1 + 0.07 N_K / A_c$: under column compressive force

$\zeta = 1 + 0.07 N_K / A_c$: under column tensile force

$$V_{22u} = 0.5 f_{ctm} b(h_1 - c_c)\zeta + A_{s22} f_{ywm} = \frac{(h_1 - c_c)}{s_{22}} + V_{manto} \le 0.22 f_{cm} b h_i$$

$$V_{33u} = 0.5 f_{ctm} h_i (b - c_c)\zeta + A_{s33} f_{ywm} = \frac{(h_1 - c_c)}{s_{33}} + V_{manto} \le 0.22 f_{cm} b h_i$$

$0.22 f_{cm} b h_i = 0.22 * 6.63 * 300 * 300 = 131.274kN$

$V_{22u} = 0.5 * 0.90 * 300 * 280 * (1 + 0.07 * 80.472/90) + 151 * 220 * 280/250 = 77.372kN \le 131.274kN$

$V_{33u} = 0.5 * 0.90 * 300 * 280 * (1 + 0.07 * 80.472/90) + 151 * 220 * 280/250 = 77.372kN \le 131.274kN$

$$V_r = V_{22u} V_{33u} \sqrt{\frac{(V_{22e})^2 + (V_{33e})^2}{(V_{33u} V_{22e})^2 + (V_{33e} V_{22u})^2}}$$

$$V_r = 77.372 * 77.372 \sqrt{\frac{(-29.332)^2 + (-4.0.72)^2}{(77.372 * (-29.332))^2 + (-4.072 * 77.372)^2}} = 77.372kN$$

In the above steps, Ve and Vr values were calculated for R analysis and BA/CA status, respectively. In the next step, in order to determine the Ve/Vr value, these two situations will be compared as stated below and the minimum values will be taken as a basis during the process.

Ve/Vr Calculation:

$$\frac{V_e}{V_r} = \sqrt{\frac{(V_{22e})^2 + (V_{33e})^2}{(V_{22r})^2 + (V_{33r})^2}}$$

$R\ Analizi \rightarrow V_e = 29.332kN$, $V_r = 77.372kN$

$$V_e/V_r = \frac{\sqrt{29.332^2 + 4.072^2}}{77.372} = 0.383$$

$BA/CA \rightarrow V_e = 15.116kN$, $V_r = 77.372kN$

$$V_e / V_r = \frac{\sqrt{15.116^2 + 1.370^2}}{77.372} = 0.196$$

$V_e/V_r = Min(V_e/V_r) \Rightarrow$ $V_e/V_r = 0.196$, $V_e = 15.116kN$, $V_r = 77.372kN$

2.1.4. Determination of Element Class:

The element class was selected by first identifying which section of the column classification table (RYTEIE 2019) would be inspected based on the Ve/Vr ratio. The element class was determined in the table for situations that meet the stirrup

spacing, hook situation, and transverse reinforcement area requirements, as well as situations that do not.

$(A_{sh}/s_{bk})_{22} = 151/250/260 = 0.0023,$
$(A_{sh}/s_{bk})_{33} = 151/250/260 = 0.0023,$
$V_e/V_r = 0.196$
$S = 250mm \geq 100mm, 135°hook,$
$A_{sh}/s_{bk} * f_{ywm}/f_{cm} = 0.0023 * 220/6.63 = 0.076$
(A_{sh}: The sum of the projections of the cross-sectional area values of all stirrup arms and distance pieces in the column or wall head zone along the height corresponding to the transverse reinforcement spacing, s: Transverse reinforcement spacing, b_k: distance between the outermost transverse reinforcement axes)
Considering the above parameters, the element class was determined as B according to the column classification table (RYTEIE 2019).

2.1.4. Determination of Limit Values:

According to the column group that is suitable for the determined element class, limit values will be found for the columns from the limit value m_{limit} of the Impact/capacity ratio and limit value $(\delta/h)_{limit}$ of the effective relative stories drift ratio (RYTEIE 2019). Linear interpolation will be made for intermediate values.

$Nk/(f_{cm}Ac) = 80.472/(6.63*0.09*1000) = 0.135,$
$A_{sh}/(s_{bk}) = 151/250/260 = 0.0023,$
$m_{sınır} = 2.878$
The $(\delta/h)_{limit}$ was determined as 0.016.

Determination of Risk Status:

Upper End

Impact $\{M_{22} = -9.414kNm, M_{33} = -48.123kNm$
Capacity $\{M_{22} = -7.388kNm, M_{33} = -37.769kNm$

$M = 49.035kNm$
$M_p = 38.485kNm$

Lower End
Impact $\{M_{22} = 2.869kNm, M_{33} = 116.803kNm$
Capacity$\{M_{22} = 0.971kNm, M_{33} = 39.462kNm$

$M = 116.838kNm$
$M_p = 39.474kNm$

Upper End
$m = 49.035/38.485 = 1.274 < 2.878$
Lower End
$m = 116.838/39.474 = 2.960 < 2.878(\delta/h) = 0.0645/3 = 0.0215 < 0.016$

The m_{limit} and $(\delta/h)_{limit}$ values determined with the determined m and (δ/h) values are compared for the two ends of the column as stated above, and if any condition is exceeded, the **element** will be considered as **risky**. The risk conditions of the other columns were made according to the steps followed in above column no: 1, and all columns were found to be risky.

3. RISK ASSESSMENT OF THE BUILDING

The element risk assessment of the building designed by us was completed, and the ground and first floors were subjected to a risk assessment to review the building's risk assessment. Based on this, the variables required for the analyses were determined as below and the risk conditions of the floors were identified. Because any of the floors investigated poses a risk, the building is considered as risky.

3.1. Ground Floor Assessment:

Sum of the axial load obtained from G + nQ loading: 9250000 N
Total number of columns on the floor: 8
Total column area on the floor: (300*300*8) = 720000 mm^2
Total axial compressive stress: (925000/720000) = 1.285 Mpa
Average axial compressive stress: (1.285/8) = 0.161 Mpa
Floor shear force limit value: 0.35
The sum of the shear forces of the elements exceeding the risk limit: 438.349 kN
Total floor shear force: 438.349 kN
438.349/438.349 = 1 > 0.35 **The floor is risky**

3.2. 1st Floor Assessment:

Sum of the axial load obtained from G + nQ loading: 382500 N
Total number of columns on the floor: 8
Total column area on the floor: (300*300*8) = 720000 mm^2
Total axial compressive stress: (382500/720000) = 0.531 Mpa
Average axial compressive stress: (0.531/8) = 0.066 Mpa
Floor shear force limit value: 0.35
The sum of the shear forces of the elements exceeding the risk limit: 269.121 kN
Total floor shear force: 269.121 kN
269.121/269.121 = 1 > 0.35 **The floor is risky**.

3. CONCLUSION

This study aimed to examine and determine the risk status of buildings constructed before 2000 in the Siverek district of Şanlıurfa province. A reinforced concrete structure with two stories was designed for this purpose, and its risk assessment was performed. The existing concrete strength and reinforcement status of the designed building is considerably beyond the scope of the current regulation and insufficient. The risk assessment of the building examined in this study was carried out in accordance with the principles of low-rise reinforced concrete structures established in RYTEIE (2019). The structure is made up of 16 columns and is supported by a frame system. The risk of each of these vertical elements was assessed, risk analysis was performed inside each floor, and the risk status of the building was established. The current version (published in 2019) of RDRB, which entered into force in 2013, will enable a more comprehensive examination of the risk structure analysis by making various additions to the current version of the Earthquake Hazard Maps of Turkey. It is remarkable that the features of our country's building stock are identical to those found in the literature and field studies. As a result, it is suggested that the building stock built before and after 2000 be inspected in accordance with the recent regulations.

REFERENCES

[1] Yön, B., Onat, O., Öncü, M. E., and Karaşin, A. Failures of masonry dwelling triggered by East Anatolian Fault earthquakes in Turkey. Soil Dynamics and Earthquake Engineering, 133, 106126. 2020.
[2] A. Ünal. Reinforcement of reinforced concrete frames not designed according to TDY 2007 with a toothed shear wall. Selcuk University Graduate School of Natural and Applied Sciences. Konya. 2012.
[3] TMMOB Chamber of Geological Engineers (jmo.org.tr)
[4] Ulutas H. Comparison of DBYBHY (2007) and TBDY (2018) Earthquake Regulations in terms of Section Damage Limits. European Journal of Science and Technology. vol 17. pp. 351-359. 2019.
[5] Ayhan, Ersin, Gültekin AKTAŞ, and Abdulhalim KARAŞİN. "Evaluation of some buildings in Siirt according to the risky building detection regulation." Dicle University Engineering Faculty Journal of Engineering 12.1. 89-98. 2021.
[6] Turkoglu, Akin. and Meydanli Atalay. H., "Determination of Earthquake Safety of a Historic Masonry Building in the Scope of TBDY-2018 and RYTEIE-2019." Düzce University Journal of Science and Technology 10.4: 1926-1938. 2022.
[7] Alicioglu, M. B. Earthquake Risk of Existing Reinforced Concrete Buildings in the Center of Manisa. Journal of Disaster and Risk, 5(1), 138-150. 2022.
[8] Türkel, Y. E., and Tekeli, H. Earthquake risk assessment of residential reinforced concrete buildings. Journal of Polytechnic, 21(3), 669-680. 2018.
[9] S. Altın Karayahshi. Comparison of Existing Building Evaluation and Risky Building Evaluation in Public Buildings. Master Thesis. Celal Bayar University Institute of Science and Technology. Manisa. 2016.
[10] Z. Korkmaz. Comparison of the "Japanese Seismic Method" and the "Detection Principles of Risky Structures 2013" Regulation in Determining the Earthquake Performance of Buildings. Master Thesis. Maltepe University Institute of Science and Technology, Istanbul. 2017.
[11] Okuyucu, D., Savaş, G. K., Gedik, B., Şuşarlıoğlu, M. F., and Tarık, K. A. Determination of regional earthquake risk distribution of buildings by street scanning method: Erzurum–Yenişehir sample. Fırat University Journal of Engineering Sciences, 30(1), 219-231. 2018.
[12] E. Ekinci. Urban Transformation Studies and Cost Analysis for Risky Building Stock in Turkey: A Case Study. Master Thesis. Gazi University Institute of Science and Technology. Ankara. 2018.
[13] S. Can. Evaluation of Risky Buildings by Earthquake Safety Screening Method. Master Thesis. Istanbul Technical University, Institute of Science and Technology. Istanbul. 2019.
[14] Işık, E. and Tozlu, Z., "Calculating Building Performance Score Using Different Variables." Bitlis Eren University Journal of Science 4.2. 161-172. 2015.
[15] Hacımustafaoglu. S.F. Altan. M.F. Naim. S. Determination of Risk Situations of Risky Buildings by Observational Analysis. Aurum Journal of Engineering Systems and Architecture. vol. 5.1 pp. 109-118.
[16] Gürbüz. A. and Tekin. M. Determination of Regional Earthquake Risk Distribution of Existing Buildings by Performance Ranking Method. Celal Bayar University Journal of Science. vol. 11.1 pp. 37-48. 2015.
[17] Işık. E. Calculation of the Performance Score of a Damaged Reinforced Concrete Building. International Anatolia Academic Online Journal. vol. 3, 2, pp. 47-52. 2015.
[18] Işık. E. and Dusty. Z. Calculation of Building Performance Score Using Different Variables. Bitlis Eren University Journal of Science. vol. 4.2 pp. 161-172. 2015.

BIOGRAPHIES

İsmail Ümit ÇIKMAN born in 1994 in Şanlıurfa, Siverek. He graduated from Harran University, Department of Civil Engineering in 2017. Later, he completed his master's degree in Dicle University, engineering faculty, civil engineering department, building department in 2020. Currently, he continues his doctorate education in the Department of Materials at Bartın University, Department of Civil Engineering. In addition, after working as an Instructor in Afyon Kocatepe University, Faculty of Engineering, Civil Engineering, he is now working as an Instructor in Dicle University Technical Sciences Vocational School, Construction Department, Construction Technology Program. His fields of study are earthquake resistant building design, examination of risky structures and building materials.

Mehmet Emin ÖNCÜ received the B.Sc. degree in Civil Engineering in 1994 from Harran University. He received his M.Sc degree in Civil Engineering in 2000 from Atatürk University, and his Ph.D. degree in Civil Engineering in 2008 from Fırat University. Currently, he works as Associate Professor at Dicle University, Diyarbakır, Turkey. His research focuses on nonlinear analysis, performance-based seismic design and evaluation, risky structures, historical structures, repair and retrofitting of structures.

Şermin KOÇYİĞİT born 1978, received her Msc and PhD at the University of Firat, Elazığ, Turkey, in 2004 and 2016, respectively, while working in the institute of science and technology, building education department. At present, she is employed at the University of Dicle. Her fields of interests include materials science, hydraulic, risky structures, building materials.

European Journal of Technique

journal homepage: https://dergipark.org.tr/en/pub/ejt

Vol.13, No.1, 2023

Investigation of Static and Dynamic Analysis of Asynchronous Motors in the Cement Industry

Hayrullah Cagtay ALKAYA[1*] and, Sertac GORGULU[2]

[1*] Burdur Mehmet Akif Ersoy University, The Graduate School of Natural and Applied Sciences, 2130127009, Burdur, Turkey. (e-mail: alkayacagtay@gmail.com).
[2] Burdur Mehmet Akif Ersoy University, Dep. of Electrical - Electronics Eng., Burdur, Turkey. (e-mail: sgorgulu@mehmetakif.edu.tr).

ARTICLE INFO

Received: Dec., 26. 2022
Revised: Jan., 12. 2023
Accepted: Jan., 15. 2023

Keywords:
Predictive maintenance
Asynchronous motor
Dynamic analysis
Static analysis
Vibration
Cement

Corresponding author: *H.Çağtay ALKAYA*

ISSN: *2536-5010* | e-ISSN: *2536-5134*

DOI: https://doi.org/10.36222/ejt.1223666

ABSTRACT

Today, with the developing technology, it is important to establish facilities suitable for industry 4.0 in order to reduce CO_2 emissions in factories, ensure efficiency, and automatically monitor the systems. Cement Factories are at the forefront of energy-intensive sectors. The cement industry is constantly focused on production, high energy demand and unforeseen failures lead to high-cost loss and systemic crises with the decrease in production/sales targets. Predictive maintenance, which is one of the maintenance methods, is aimed to solve the problems by determining the failure sources that may occur economically by examining and analyzing the physical parameters such as vibration, temperature, frequency changes, amperes, and spectra of the asynchronous motors in the field in trend data. In this study, dynamic and static analysis of large power asynchronous motors with a stator voltage of 6300V in cement plants are analyzed with the help of advanced measuring instruments. As a result of the analyses, a general evaluation study was carried out on the actions to be implemented in the maintenance plan by identifying the types of failures that may occur in advance.

1. INTRODUCTION

As the number of industries increases with the developing technology in Turkiye and the world, energy demands also increase [1]. Each increase brings with it the proliferation and development of energy production facilities together with excess consumption. In Turkiye, cement industrial facilities are among the most energy-intensive sectors.

In the cement industry, various maintenance methods have been developed to operate the process according to the standards, to ensure the continuity of production, to eliminate the risks of occupational accidents, and to prevent energy losses [2]. The machine equipment used in this industry has an important place in the process as they operate under heavy drive and load, and predictive maintenance, which is one of the maintenance methods, plays an important role since the failure of the equipment will negatively affect production [3].

The machines operated in the units within the enterprise should be monitored and reported in certain plans and periods, and as a result of the analyses, when an undesirable situation is encountered, the machine equipment and the unit should be taken into the stop plan and maintenance work should be started [4]. In case of malfunction, the operation of the equipment will lead to weakening in the process, low quality of the material produced, unplanned stoppage of the unit, and consequently cost loss.

Approximately half of the electrical energy obtained from power generation facilities in Turkiye is consumed in such industrial facilities. Approximately 70% of the electrical energy used in these facilities is consumed by electric motors [5, 6].

Since asynchronous motors are essential in the cement industry and use the majority of electrical energy, electrical and mechanical maintenance controls must be carried out for asynchronous motors to operate efficiently and to avoid losses in process and production. These controls are carried out by condition monitoring and analysis methods [7].

With electrical condition monitoring and analysis methods, unbalanced phase losses, overload, short circuits between phases, short circuit and open windings, tilted rotor faults, broken rotor bars, and insulation faults can be detected [8].

Mechanical condition monitoring and analysis methods can detect faults such as unbalance, bearing failure, mechanical looseness, gear failure, coupling misalignment, and axis disturbance [9].

Predictive maintenance can be characterized as a set of efforts to compare, analyze and interpret engineering limits by measuring and examining trend data such as vibration, temperature, pressure, voltage, increases in the amperes drawn by the motors of the equipment in active operation, and to provide the most economical and fastest solution to the problems that may become malfunctioning [10, 11].

There are some criteria for data interpretation during field studies and analysis. Engineering activities and limit definitions must be done correctly. Although the physical parameters of the measuring equipment are known, the working environment and process data must also be well-analyzed [12].

Establishing the necessary infrastructure for the efficient implementation and operation of predictive maintenance activities is important for the continuity of production and the efficiency of the process [13]. The benefits of this maintenance activity are;

- Minimizing costs in maintenance and repair activities
- Maximum product quality and process efficiency
- Reduced downtime of equipment
- Ensuring energy efficiency by complying with the work plan of the maintained unit
- Reducing breakdowns and keeping equipment ready for operation
- Increasing the reliability levels of equipment
- Optimization of spare parts by timely estimation of parts planned to be replaced
- The most efficient use of the labor force
- Reducing and eliminating OHS risks
- Achieving maximum efficiency from the capital spent for the operation by ensuring the efficiency of the equipment.

To determine and evaluate the instant operating conditions of the equipment in industrial facilities and to carry out maintenance activities within the plans, fault detection with vibration analysis, fault detection with thermal camera measurements, damage detection with oil analysis, damage detection with visual analysis, damage detection with sound analysis are transferred to the computer environment with the processing of the signals after the data collection system operations. Following these studies, the actions to be taken are determined [14].

Predictive maintenance appears as a philosophy of care. Evaluating the analyses in a computer environment and turning the studies carried out in the field into practice and receiving the returns in terms of efficiency-cost are studies that all units in the industry should contribute. Predictive maintenance work should be seen as teamwork rather than being applied alone [2, 14].

In the global and national cement industry, there are asynchronous motors, compressed air compressors, multistage gearboxes, low and high-capacity fans, and material handling equipment operating with low and high voltage. Due to the high installation and operating costs of this equipment, the system must be used until the end of its useful life [2, 14]. One of the key points of increasing equipment efficiency is to monitor and analyze the system data before failures occur and to eliminate problems by root-cause analysis. During the evaluation of analyses, it will not be sufficient to act on a single data point. Clearer and more positive results are obtained if process data is analyzed as well as multiple data and evaluated by considering environmental and ambient conditions [15].

Within the scope of this study, the dynamic analysis of the asynchronous motor with a stator voltage of 6300V operating under heavy load and drive in the Crusher-1 unit and the static analysis of the asynchronous motor of the Cement Mill-3 unit were examined and the areas for improvement were identified and the points where maintenance is required were determined.

2. MATERIAL AND METHODS

In this study, static and dynamic tests and analysis of the main drive motors and system fans with a stator voltage of 6300V belonging to the units used in a large cement factory industrial plant will be carried out. The components of the measurement operation of these motors are the asynchronous motor, the data acquisition system, and special equipment for data processing. Pruftechnik Vibscanner 2 model portable data collector vibration device, SKF Static Motor Analyzer Meger-Baker device, and thermal camera equipment will be used.

2.1. Characteristics of the Equipment to be used in Dynamic Analysis

In the field study of vibration measurements in dynamic plants, a device with universal software that facilitates easier, more powerful condition monitoring by analyzing vibration signals and process variables by simultaneously measuring overall values, spectra, and time signals in 3 axes, depending on filter settings, with 3-channel route-free measurements with a sampling rate of up to 131 kHz per channel, was used as a data collector. The label data of the asynchronous motors to be measured will be defined for the device to be used and the work will be started after the measurement points are determined. Once collected, the data will be computerized for signal processing [16].

Figure 1. Vibration FFT Analyzer [16]

2.2. Features of Equipment to be used in Static Analysis

In static tests, insulation resistance, insulation conditions, and short circuit analysis of the windings of a motor are required to maximize the efficiency of asynchronous motors. In our field applications, a special device with easy portability, maximum test voltage between 4–40 kV, record storage capacity of approximately 400 coils, source current maximum of 600 mA, overcurrent error 1.2 mA, ease of data transfer by USB and universal software were used. After the asynchronous motors to be measured are de-energized and safety applications are completed, the operation will be run following that the

connections are made on the motor supply terminals. Once the data is collected, it will be transferred to a computer for signal processing [17].

Figure 2. Static Motor Analyzer SKF Baker DX Series [17]

3. RESULTS AND DISCUSSION

3.1. Investigation of Vibration Analysis of Asynchronous Motors with Dynamic Testing

The crusher-1 main drive motor is an important piece of equipment belonging to the unit that crushes the raw materials coming to the factory. In order to operate the motor efficiently, electrical and mechanical maintenance work must be carried out in certain periods. The shape of the motor, from which the vibration data is collected, is horizontal and connected to the steel frame with foot bolts. The front and rear bearings of the induction motor consist of grease-lubricated ball bearings. It is connected to the system it drives by a belt-pulley system. Shim plates are evenly distributed on the motor legs for vibration control. The tag values of the motor are given in Table I.

TABLE I.
CRUSHER-1 MOTOR TAG INFORMATION

Tag Information	Tag Values
Brand	WSW
Type	Orr34635-6
Power	450 kW
Handover	988 rpm
Stator Voltage	6300 V

Vibration measurement values of the main drive motor are given in Table II.

TABLE II.
CRUSHER-1 MAIN DRIVE MOTOR VIBRATION MEASUREMENT VALUES

	Vibration value mm/s	
	Motor	Load
DE Horizontal	5.441	1.360
DE Vertical	2.605	2.333
DE Axial	3.835	1.456
NDE Horizontal	6.116	
NDE Vertical	4.827	
NDE Axial	3.727	

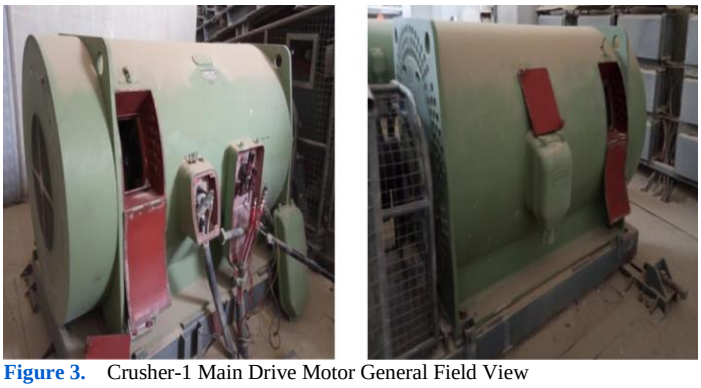

Figure 3. Crusher-1 Main Drive Motor General Field View

Figure 4. Crusher-1 Motor DE Horizontal Vibration Analysis

DE Horizontal measurement shows a dominant signal corresponding to 1X layer of the RPM. This signal can be characterized as unbalanced. Since the motor is integrated into the load with a belt-pulley system, the belt-pulley settings should be checked and recalibrated. Although it is observed as unbalanced in the 1X layer, other factors should also be examined. In the literature, the change in vibration values of 1X times over time is referred to as “light rotor rubbing”. For this reason, it would be useful to measure and check the bearing cover clearances. Other reasons to suspect friction failure are due to DE vertical and DE axial measurements. Light rubbing can be triggered by geometric misalignment problems (shaft misalignment due to thermal expansion), and specific load and temperature values.

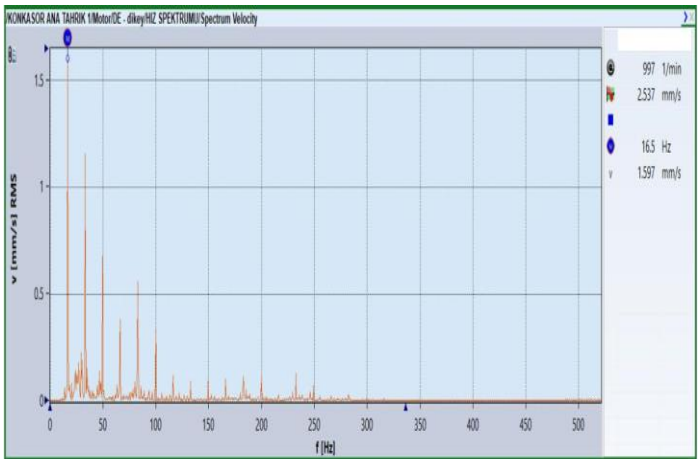

Figure 5. Crusher-1 Motor DE Vertical Vibration Analysis

DE vertical measurement shows high signals predominantly at the 1X layer and as a side factor at the 2X, and 3X layers. Bearing cover clearance needs to be checked and also balancing adjustments need to be made.

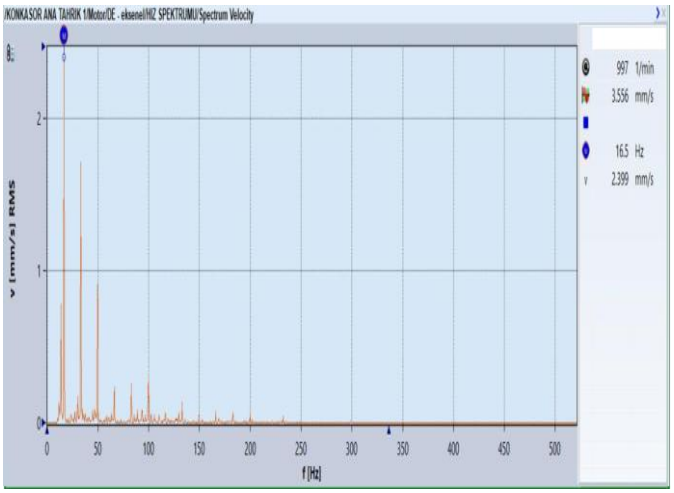

Figure 6. Crusher-1 Motor DE Axial Vibration Analysis

DE axial measurement shows a graph of the speed in multiples of 1X, 2X, and 3X. The signals in these layers occur when the motor shaft and the rotor shaft coincide at a certain distance. Angular misalignment causes high vibration in the axial direction and a 180-degree phase difference between the two shafts. It is necessary to check the gap between the bearing and the cover during maintenance. Since it is connected to the system with a belt pulley, it will be beneficial for process and motor efficiency to readjust its adjustment during maintenance.

3.1.1. Crusher-1 Main Drive Motor Analysis Results and Suggestions

During the vibration test performed on the Crusher-1 main drive motor, the vibration values of the motor are above the standards. It is observed that the dominant signals seen at the 1X layer are due to unbalance, with angular misalignment and slight rotor friction as side factors. When the vibration graphs are examined, it is seen that these signals are caused from the motor. The motor is connected to the load by a belt-pulley system. It is necessary to check the adjustment of the belt-pulley system to which it is connected with the load and to make a new adjustment. In addition, the graphs of the measured vibration values show harmonics in the bearing carrier covers, which means a gap.

3.2. Static Test Analysis Review of Asynchronous Motors

The main drive motor of the Cement Mill-3 is one of the most important main pieces of equipment of the unit where the grinding of cement is carried out. The shape of the motor is horizontal and connected to the steel frame with foot bolts. The front and rear bearings of the asynchronous motor consist of grease-lubricated ball bearings. The gearbox it drives is geared and connected by coupling. Shim plates are evenly distributed on the motor feet. The air filters are clean. The tag values of the motor are given in Table III.

TABLE III.
CEMENT MILL-3 MOTOR TAG INFORMATION

Tag Information	Tag Values
Brand	SIEMENS
Type	1RS-1802-5HA-90-Z
Power	1600 kW
Handover	493 rpm
Stator Voltage	6300 V

Figure 7. Cement Mill-3 Main Drive Motor General Field View

TABLE IV.
STATOR RESISTANCE, INDUCTANCE, AND CAPACITANCE MEASUREMENT VALUES

Stator Resistance	Lead 1-2	Lead 2-3	Lead 3-1	Unbalance [%]	Average
DC Resistance [mΩ]	264.3624	255.5788	264.3221	2.2	261.4211
Temp Corrected R [mΩ]	286.9501	277.3996	268.8416		283.7304
Inductance					
Frequency [Hz]	50.0	50.0	50.0		
Impedance [mΩ]	24.730	24.676	24.639	0.2	24.682
Impedance Ang [°]	45.3	45.3	45.3	0.0	45.3
Inductance [mH]	55.945	55.849	55.741	0.2	55.845
Dissipation Factor	0.990	0.989	0.990		
Capacitance					
Frequency [Hz]	4000.0				
Capacitance [nF]	4600.5				
Dissipation Factor	22.747				
Quality Factor	0.044				
Temperature	32.0 [°F]				

Table IV shows that the DC resistance levels and temperature resistances between the phases of the stator are at a good level with an average of 261.4211 mΩ. The impedances between the phases are measured as balanced and the average is 24.6828 mΩ.

TABLE V.
CEMENT MILL-3 MAIN DRIVE MOTOR ROTOR HIPOT MEASUREMENT VALUES

Rotor Insulation Resistance (IR) Result	
Voltage [V]	1090
I [µA]	0.899
IR [MΩ]	1212
HiPot Result	
Voltage [V]	1550
I [µA]	0.976
IR [MΩ]	1588

In Table V, the rotor HiPot measurement values are given. As seen in Table V, the insulation resistance (IR) is measured at 1212 MΩ and 1588 MΩ at 1090 V and 1550 V measurements on the rotor. Insulation levels are measured as well. Fig. 8 shows the DC test results of the rotor. Where; IR is insulation resistance.

TABLE VI.
CEMENT MILL-3 MAIN DRIVE MOTOR STATOR HIPOT MEASUREMENT VALUES

Stator Insulation Resistance (IR) Result	
Voltage [V]	5120
I [µA]	0.506
IR [MΩ]	10119
HiPot Result	
Voltage [V]	6310
I [µA]	0.473
IR [MΩ]	13340

In Table VI, the stator HiPot measurement values are given. In Table VI, the insulation resistance (IR) on the stator was measured as 10119 MΩ and 13340 MΩ at 5120 V and 6310 V. Insulation is measured at a good level. Fig. 9 shows the DC test results of the stator. Where; IR is insulation resistance.

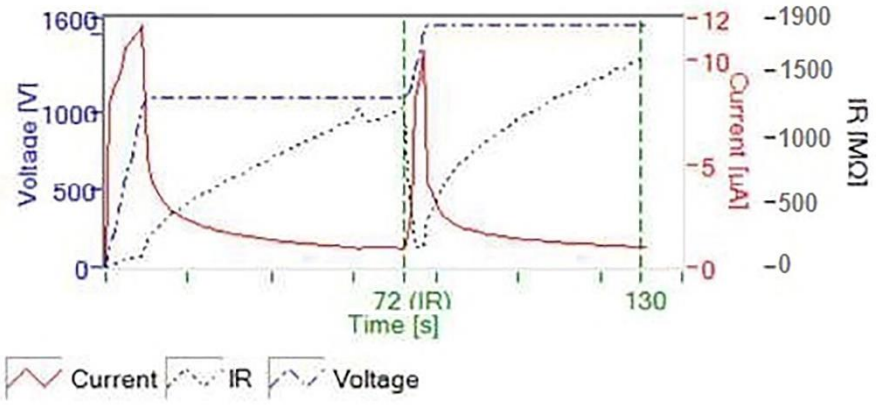

Figure 8. Rotor DC Test Results

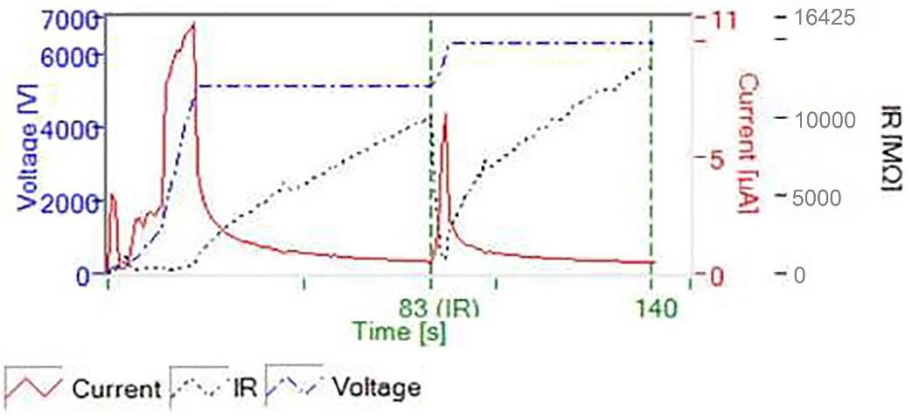

Figure 9. Stator DC Test Results

TABLE VII.
CEMENT MILL-3 MAIN DRIVE MOTOR ROTOR SURGE TEST MEASUREMENT VALUES

Lead	Peak Voltage [V]	Number of Pulses	PP EAR Status	Max. PP EAR[%]
1	1540	9	PASS	3
2	1540	3	PASS	2
3	1540	5	PASS	3

In Table VII, the rotor surge test measurement values are given. Fig. 10 shows the surge test graphs of the rotor. In Fig. 10, the number of pulses at the peak voltage of 1540 V applied to the rotor can be seen intact in the surge waveform.

In Table VIII, the stator surge test measurement values are given. Fig. 11 shows the surge test graphs of the stator. In Fig. 11, at a peak voltage of 6260 V between phases applied to the stator, the ripple waveform between phases is observed normally.

TABLE VIII.
CEMENT MILL-3 MAIN DRIVE MOTOR STATOR SURGE TEST MEASUREMENT VALUES

Lead	Peak Voltage [V]	Number of Pulses	PP EAR Status	Max. PP EAR[%]
1-2	6260	10	PASS	0
2-3	6260	5	PASS	2
3-1	6260	7	PASS	2

3.2.1 Cement Mill-3 Main Drive Motor Analysis Results and Suggestions

After static tests and visual inspections of the main drive motor of Cement Mill-3, negative conditions were not found. There are no abrasion, ovality, and arc marks on the ring surface. The engine coals were pressed against the bracelet in a normal condition and there was no tooth loss. The distances between the pressures of the portables are measured at the correct level. The insulation resistance (IR value) and vibration values of the motor are in accordance with ISO standards.

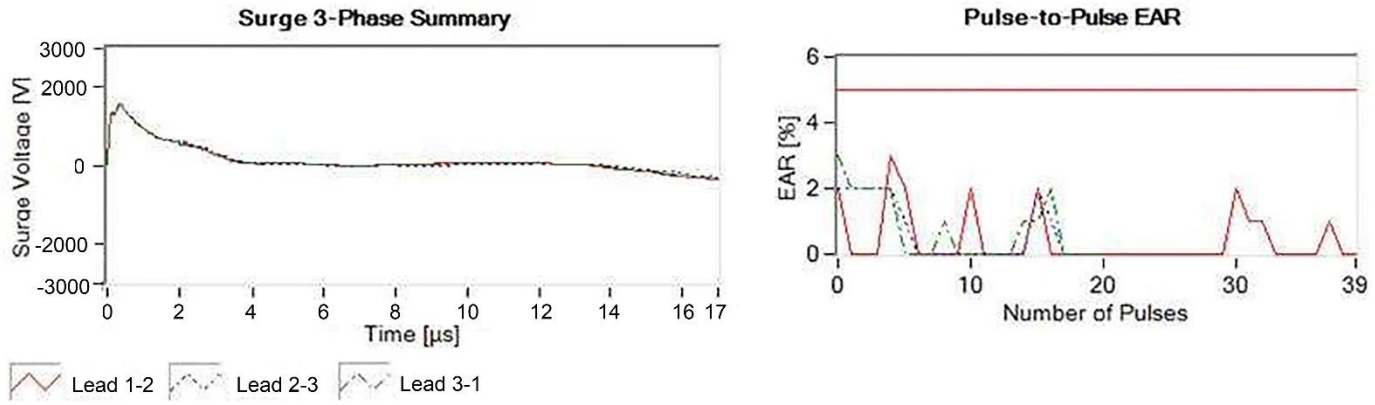

Figure 10. Rotor Surge Test Graphics

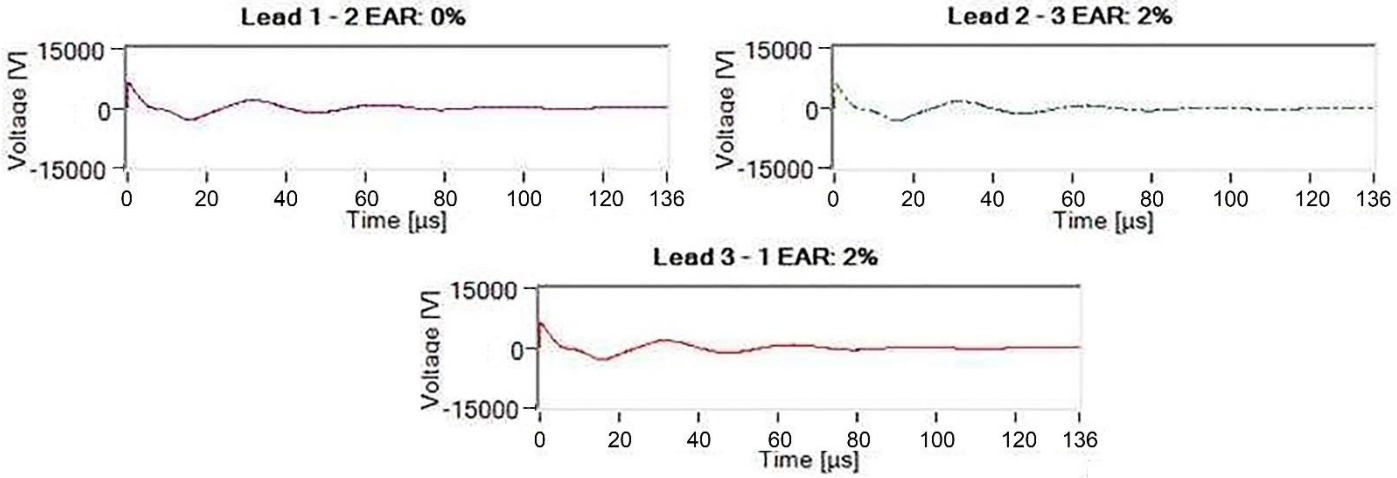

Figure 11. Stator Surge Test Graphics

4. CONCLUSION

As asynchronous motors are widely used in the cement industry, when undesirable situations are encountered, problems such as decreased product quality, increased energy use, labor losses, energy imbalance, increased maintenance costs, and decreased equipment efficiency are encountered in the process. Modern maintenance methods are applied in order to prevent and detect these problems in advance.

Predictive maintenance works, which is one of the modern maintenance methods, have been carried out and the areas that need to be maintained in the missing parts have been determined. Two high power induction motors are analyzed practically and theoretically by considering each parameter separately.

In this works; bearing cover clearance failures, unbalance, misalignment, misalignment, mechanical looseness, and light rotor friction were analyzed by vibration analysis. In electrical measurements, static and dynamic tests were performed; stator and rotor insulation resistance measurements, Hi-Pot, Surge tests, PI and DAR tests were performed and the types of faults were determined and improvement areas were identified.

In the dynamic analysis of the crusher-1 main drive motor, a dominant signal was observed in one direction depending on the direction in which the mass balance was disturbed, and this appears with vibration signals due to unbalance. Since the motor is connected to the load by belt and pulley system, the adjustment should be checked. As a side effect, the gaps in the bearing carrier covers also affect the signals, and the motor and load sides should be maintained and adjusted during the planned stop.

In the static test analysis of the main drive motor of the Cement Mill-3, it is observed that the insulation resistance (IR) is high and good. The pressing surfaces and distances of the coal holders to the ring are balanced. No arc marks and abrasion were observed on the ring surface. In the surge test, the resistance is above the standards. Wave frequencies between phases were observed equally.

In order to interpret the graphs in vibration analysis and electrical measurement tests, it will be useful for the working plant to determine the history and failure types of the equipment to be measured in advance.

Analyzing the graphs alone will not be sufficient for the investigations. In addition, knowledge of the process operation logic and the effects of structural and environmental sources on the equipment are among the important parameters for fault diagnosis.

One of the aspects that need to be improved for the business to continue to operate safely and smoothly is to ensure that failure does not recur. Recently, with the development of technology and competition, the philosophy of reliability-based maintenance has become widespread. In this philosophy, it is necessary to find the root cause of malfunctions and intervene in the equipment at the right time and to instill this philosophy by providing the necessary training to the personnel working on the equipment.

ACKNOWLEDGEMENT

This study has been produced from the master's degree dissertation of H. Çağtay ALKAYA.

REFERENCES

[1] Yıldız, A., Endüstri 4.0 ve Akıllı Fabrikalar, *Sakarya University Journal of Science*, 22 (2), 546–556, 2018. https://doi.org/10.16984/saufenbilder.321957

[2] Aydın, G., Meran, C., Çimento Sektöründe Kestirimci Bakımla Arıza Teşhisi ve Önlenmesi, *Mühendis ve Makina*, 59 (692), 48–67, 2018.

[3] Şahin, A., Büyük Güçlü Asenkron Motorlarda Titreşim Analizi ile Arıza Teşhisi, M. Sc. Thesis, Kocaeli University, Kocaeli, Turkey, 2018.

[4] Çavdarcı, M.A., Çimento sektöründe titreşim analizi ve kestirimci bakım yöntemleri, M. Sc. Thesis, Erciyes University, Kayseri, Turkey, 2021.

[5] Esen, G.K., Türkiye ve Dünyada Elektrik Motorları Enerji Tüketimi ve İlgili Teknik Mevzuat, Türk Standardları Enstitüsü. https://www.emo.org.tr/ekler/364734147179187_ek.pdf [Accessed: 21-Dec-2022].

[6] Uzun, H., Akar, O., Demirci, A., Aküner, M.C., Terzi, U.K., Analyzing High Efficiency Asynchronous Motors Using Scalar Control Technique, *Balkan Journal of Electrical and Computer Engineering*, 6, 23–26, 2018. https://doi.org/10.17694/bajece.410219.

[7] Kabul, A., Asenkron Motor Arızalarının Stator Akımı ve Titreşim Sinyalleriyle Analizi ve Tespiti, Ph.D. Thesis, Dumlupınar University, Kütahya, Turkey, 2022.

[8] Akbayır, K., Asenkron Motor Stator Arizalarinin Kaçak Akı Yöntemi İle Tespiti ve Prototip Geliştirilmesi, M.Sc. Thesis, Inonü University, Malatya, Turkey, 2022.

[9] Özelgin, İ., Asenkron Motor Arızalarının Dinamik Parametrelere Etkisi ve Frekans Analizi ile Tanısı, M.Sc. Thesis, Istanbul Technical University, Istanbul, Turkey, 2006.

[10] Çeven, S., Bayır, R., Bir Asenkron Motorun Mekanik Titreşim Sinyallerinin Ölçülerek Arıza Analizinin Yapılması, *European Journal of Science and Technology Special Issue*, 312–322, 2020. https://doi.org/10.31590/ejosat.780063.

[11] Güven, K., Periyodik Bakım Yapan Bir Tekstil İşletmesinde Bilgisayar Destekli Toplam Verimli Bakıma Geçiş ve Kaliteye Etkisi, M.Sc. Thesis, Erciyes University, Kayseri,Turkey, 2006.

[12] Sındır, E., Özkaner, V., Asenkron Motorlu Sistemde Bulanık Mantık Çıkarımı İle Kestirimci Bakım, *International Journal of Multidisciplinary Studies and Innovative Technologies*, 6 (2), 181–188, 2022.

[13] Göçülü, G., İşletmelerde Kestirimci Bakım Uygulamaları, M.Sc. Thesis, Mustafa Kemal University, Hatay, Turkey, 2015.

[14] Tazegün, A., Toplam Verimli Bakım ve Çimento Sektöründe Uygulamaları, M.Sc. Thesis, Trakya University, Edirne, Turkey, 2009.

[15] Ayan, O.A., Döner Makina Elemanların Titreşim Analizi ile Kestirimci Bakımı, M.Sc. Thesis, Trakya University, Edirne, Turkey, 2019.

[16] Vibscanner 2, https://www.pruftechnik.com/com/Products-and-Services/Condition-Monitoring-Systems/Vibration-Analysis-and-Balancing/Vibration-Analyzer/VIBSCANNER-2/ [Accessed: 01-Dec-2022].

[17] SKF Static Motor Analyzer Baker, http://skf.indpart.ru/images/upload/file/PUB-CM-71-030-EN-Baker DX-user-manual.pdf [Accessed: 03-Dec-2022].

BIOGRAPHIES

H.Çağtay ALKAYA completed his undergraduate education in Electrical and Electronics Engineering at Amasya University. He is also doing his master's degree in Electrical and Electronics Engineering, which is the same branch at Mehmet Akif Ersoy University. After completing his undergraduate education, he started his career in the energy and communication sector. In order to contribute to his professional development, he has been working in the field of electrical maintenance in cement factories, which are the pioneers of industrial facilities in various regions of Turkey. He is actively working in the fields of energy management, high voltage operation responsibility, and project management. In the field of maintenance, he has gained competence, especially in the maintenance of high-voltage asynchronous motors, and is doing his master's thesis in this field.

Sertaç GÖRGÜLÜ obtained his B.Sc. degree from Marmara University in 2001. In 2002, he started to work as a research assistant at Marmara University. He received his M.Sc. and Ph.D. degrees from Marmara

University in 2004 and 2011 respectively. Between 2009 and 2013, he worked at Kırklareli University in various titles. He has been working at Burdur Mehmet Akif Ersoy University since 2013. He works in the fields of natural and artificial lighting and design, renewable energy.

European Journal of Technique

journal homepage: https://dergipark.org.tr/en/pub/ejt

Vol.13, No.1, 2023

Measurement Resolution in Uncertainty Calculation with the GUM Method Approach: A LabVIEW Application

Hakan Çıtak[1*], Sabri Bıçakçı[2]

[1*]Balikesir University, Balikesir Vocational School, Electrical and Energy Department, 10145, Balikesir, Turkey. (hcitak@balikesir.edu.tr).
[2] Balikesir University, Electrical and Electronics Engineering Department, 10145, Balikesir, Turkey. (sbicakci@balikesir.edu.tr).

ARTICLE INFO

Received: May, 15. 2023
Revised: June., 08. 2023
Accepted: June, 11. 2023

Keywords:
Measurement uncertainty
Resolution
AD7714
myRIO
LabVIEW

Corresponding author: *Hakan Çıtak*

ISSN: *2536-5010* | e-ISSN: *2536-5134*

DOI: https://doi.org/10.36222/ejt.1302461

ABSTRACT

GUM (Guide to the Expression of Uncertainty in Measurement) is a method used for calculating uncertainty in measurements. The method involves an uncertainty calculation approach which also constitutes a reference for the international ISO/IEC 17025 standard. In the GUM method, all uncertainties are expressed as standard uncertainty. An uncertainty may incorporate various components where impacts from multiple sources are taken into consideration. Resolution errors resulting from the sensitivity of the measurement equipment has a significant impact in the calculation of uncertainty. Sensitivity of an analog measurement device such as a multimeter depends on the resolution of the ADC it contains. Multimeters with 8-bit resolution ADCs are often used as measurement devices for sensor voltage values to be read once or several times. Factors such as high measurement resolution and reading errors by operators lead to an increase in uncertainty. Multiple data from a sensor or many sensors cause a significant increase in uncertainty, which results in a serious loss of time and labor. In order to mitigate said two factors which increase uncertainty in such cases, analog data needs to be converted to digital data at high resolution and transferred into computer medium. In this study, an D7714 analog/digital converter IC with 24-bit resolution has been used to transfer digital data into computer medium via myRIO 1950. A LabVIEW-based software has been developed to perform register settings for the AD7714 IC and to retrieve data at 24-bit resolution.

1. INTRODUCTION (Helvetica 10p Bold)

According to the GUM method, a measurement result is expressed between a measurement value and its uncertainty range. Uncertainty represents the degree of deviation of the measurement result from the estimated actual value and determines the accuracy and reliability of the measurement[1]. According to the GUM method, uncertainty has two components namely Type-A uncertainty and Type-B uncertainty. Type-A uncertainty reflects the repeatability or reproducibility of a measurement and estimated using statistical methods. Type-A uncertainty is based on data obtained through repetition of the same measurement under different conditions [2]. High Type-A uncertainty indicates that the measurement result is less accurate or less reliable [3]. On the other hand, Type-B uncertainty incorporates the effects of factors such as the measurement process itself or the measurement equipment, methods or environment, which usually cannot be directly calculated through the use of statistical methods. Instead, estimations based on information such as expert opinions, past experience, manufacturers' statements, literature data or calibration reports can be used [4].

Differences in results obtained by repeating an experiment multiple times under identical conditions constitute Type-A uncertainty. Such uncertainty is directly related to the repeatability of the measurement, and therefore measurement resolution [5]. For instance, in a voltage measurement device with 8-bit resolution, a one-digit change would result in an under-reading or over-reading of 19.5 mV. On the other hand, a one-digit change at 24-bit resolution corresponds to 298 µV. In summary, the higher the digital resolution is, the lower the Type-A resolution, which plays a major role in total uncertainty, would be. Within such context, if sensor data of wide range is to be collected, it would be appropriate to use delta-sigma ADCs in order to prevent adverse effects of undesired high-frequency components on digitalization and to minimize conversion errors and thereby uncertainty [6]. Further, delta-sigma ADCs are widely used in IoT applications, thanks to their low power consumption, high resolution and favorable performance characteristics [7, 8]. Such ADCs provide high sensitivity and accuracy in the

conversion of analog signals into digital signals, thereby enabling more accurate processing of data received from sensors.

Connection of a delta-sigma ADC to a USB interface is generally achieved by the use of a USB data collection board or module. Software such as LabVIEW [9], MATLAB [10], Python [11], Visual Basic and LabWindows/CVI [12] can be utilized to perform register settings for delta-sigma ADCs through aforesaid modules and retrieval, recording and processing of digital data at 50kS/s speed.

In addition, low-pass and high-pass filtering are performed on delta-sigma ADCs in order to minimize noise errors [13]. The register of the low pass filter plays a crucial role in the determination of the sampling frequency of the ADC and the reduction of high-frequency noises. Setting of said register may reduce noise by keeping sampling frequency low, but also impacts the resolution of the ADC. High pass filter register is used for reducing the low-frequency noises in ADCs. Said filter allows measurement of high-frequency components while filtering out low-frequency noise. Setting of said register may affect accuracy of measurement results by determining the frequency response of the ADC. Moreover, the sensitivity of such ADCs may decrease or change in time. Therefore, calibration techniques are utilized in order to ensure that an ADC maintains its accuracy over its lifetime. Self-scale calibration is a widely-used method to measure and improve the accuracy of delta-sigma ADCs. Self-scale calibration is a method where the ADC measures and adjusts itself for the purpose of calibration. In such method, a pre-determined reference voltage is applied to the ADC and the voltage value read by the ADC is checked. Subsequently, the ADC utilizes an internal feedback loop set its parameters in order to equalize the measured value to the correct reference voltage [15].

The benefit of self-scale calibration is that it allows the ADC to automatically calibrate itself. Therefore, allowing the ADC to calibrate itself rather than manually setting the parameters which affect the accuracy of the ADC would lead to more accurate and reliable results.

As such, minimizing Type-A uncertainty and ensuring measurement repeatability by increasing digital resolution in analog measurements have been the primary goal of the study. The study further aims to reduce uncertainty by directly transferring measurements into the computer medium at 50 kS/s speed and thereby eliminating reading errors by operators. An AD7714 Delta-Sigma ADC which performs 24-bit conversion has been used in this study. A LabVIEW-based software has been developed to perform ADC register settings and to retrieve 24-bit data from the ADC output. A myRIO module has been utilized to connect the ADC to a USB interface. The procedures for creating 24-bit digital data for the delta-sigma ADC used in the study and the transfer of the generated digital data to the computer environment via the myRIO module with a developed LabVIEW-based software are discussed in detail, which is also the innovative side of this study. Further, the uncertainty performance of the developed measurement system in repetitive measurements is also analyzed.

2. MATERIAL AND METHOD

The first step of the study has been the establishment of the electronic connection between the AD7714 delta-sigma ADC, myRIO 1950 and the PC. This step involved the determination of myRIO connection points to allow performance of ADC register settings and reading of analog sensor voltage at 24-bit resolution. Pins selected at Connector A for the ADC-to-myRIO connection is exhibited in Figure 1.

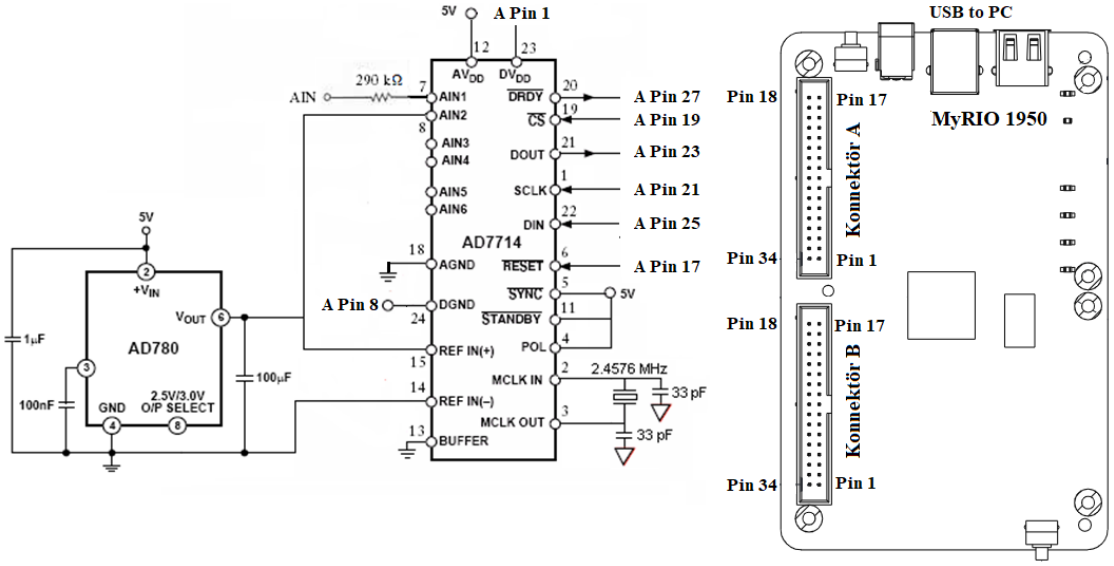

Figure 1. Electronic connection between the ADC, MyRIO 1950 and the PC.

Serial interface of the AD7714 is controlled via pins DIN, $DOUT$, $SCLK$, $\overline{DRDY}$, $\overline{CS}$ of the IC. Pin DIN is used for data transfer to the IC's registers. Pin $DOUT$ provides output for the 24-bit data generated in the data register. Pin $\overline{DRDY}$ is the communication point which indicates whether a 24-bitlik data is generated in the data register of the IC. The pin output is logic 1 if no data exists in the data register, and logic 0 if there is data. Pin $\overline{CS}$ controls IC selection and analog data input. The writing loop of said IC for the registers is provided in figure2.

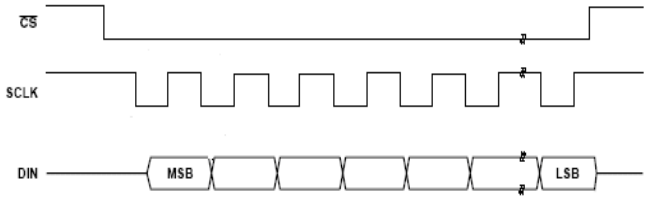

Figure 2. Writing Loop (POL=1)

The reading loop for the IF from the data registers is provided in figure 3.

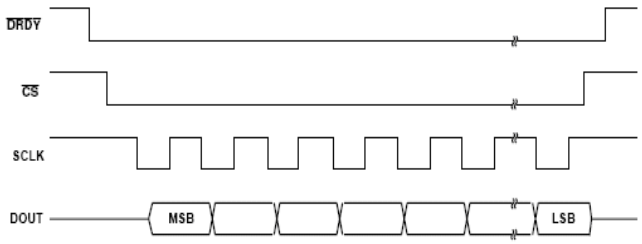

Figure 3. Reading Loop (POL=1)

In this study, programming of the registers of the AD7714 IC to convert analog data into digital data and controlling of the data register have been performed as per the flow chart provided in figure 4.

The AD7714 registers need to be reset before initiating the ADC process. This should be achieved by respectively sending the digital data specified in Table I to the relevant pins of AD7714.

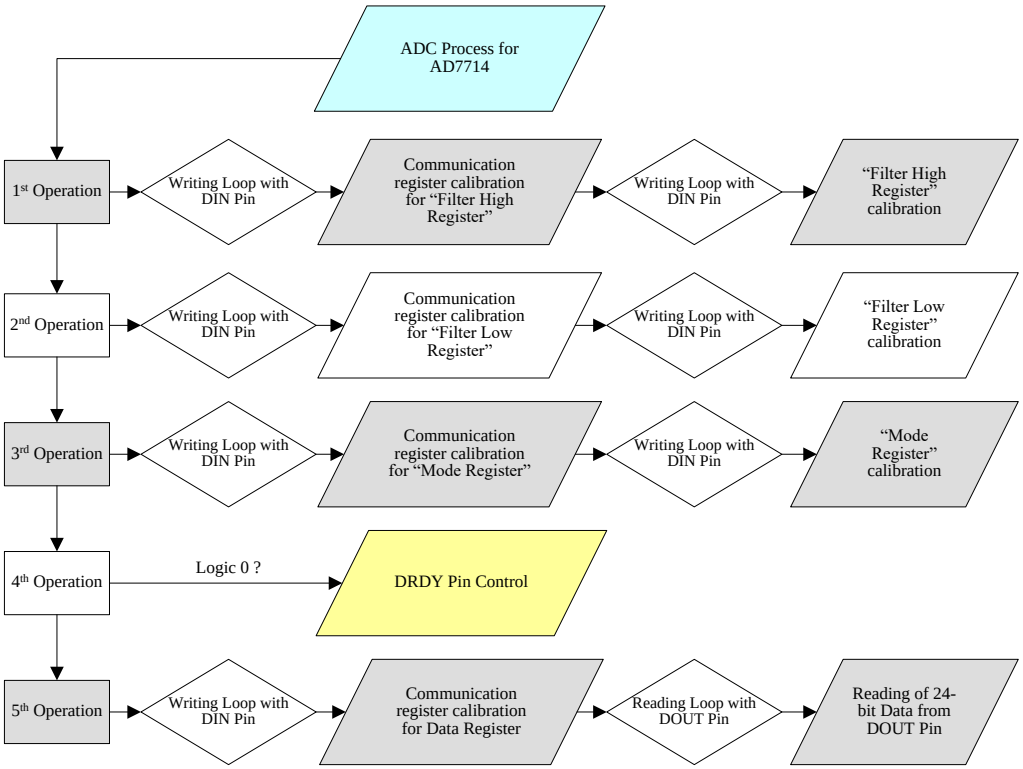

Figure 4. ADC Process for AD7714

TABLE I
RESET PROCESS OF AD7714

Pin	RESET Operations	
$\overline{CS}$	1	1
SCLK	1	1
DIN	0	0
$\overline{RESET}$	0	1

In the 1st operation step, digital data specified for the IC in Table II for communication register calibration for "Filter High Register" and digital data specified in Table III for calibration for "Filter High Register" were sent from the relevant pins of the IC, respectively, using the writing loop.

Logic 0 has been selected for the 8-bit "Filter High Register" communication register calibration of the IC, in order to ensure fastest writing operation. The subsequent 3 bits were used for register selection. The third bit was selected as logic 0 for writing operation, and the remaining 3 bits were set as AIN1/AN2, DC voltage input channels.

TABLE II
COMMUNICATION REGISTER CALIBRATION OF AD7714 FOR "FILTER HIGH REGISTER"

Pin	Communication register calibration for "Filter High Register"																	
$\overline{CS}$	0	0	0	0	0	0	0	0	0	0	0	0	0	0	0	0	0	1
SCLK	1	0	1	0	1	0	1	0	1	0	1	0	1	0	1	0	1	1
DIN	0	0	0	0	0	1	1	0	0	0	0	1	1	0	0	0	0	0
$\overline{RESET}$	1	1	1	1	1	1	1	1	1	1	1	1	1	1	1	1	1	1
		DRDY		RS2		RS1		RS0		R/$\overline{W}$		CH2		CH1		CH0		

TABLE III
"FILTER HIGH REGISTER" CALIBRATION OF AD7714

Pin	"Filter High Register" calibration																	
$\overline{CS}$	0	0	0	0	0	0	0	0	0	0	0	0	0	0	0	0	0	1
SCLK	1	0	1	0	1	0	1	0	1	0	1	0	1	0	1	0	1	1
DIN	0	0	0	1	1	0	0	0	0	1	1	1	1	1	1	1	1	0
$\overline{RESET}$	1	1	1	1	1	1	1	1	1	1	1	1	1	1	1	1	1	1
		B/U		WL		BST		ZERO		FS11		FS10		FS9		FS8		

During "Filter high register" calibration, the value of the highest bit (bipolar) for DC measurements has been set as logic 0. The value of said bit should be logic 1 for AC voltage or resistance measurements. The 7th bit of the calibration has been set as logic 1 for 24-bit resolution. The bits BST (6th bit) and Zero (5th bit) should always be set as logic 0. Filter selection in said type of ADCs are determined by a total of 12 bits of digital data. The upper 4 bits thereof constitute the lower 4 bits of the 8-bit "Filter high register" calibration. Such calibration aims to reduce low-frequency noise in the AD7714 IC. Said filter allows measurement of high-frequency components while filtering out low-frequency noise. Calibration of said register may affect accuracy of measurement results by determining the frequency response of the ADC.

The 2nd operation step following "Filter High Register" calibration involved communication register calibration for "Filter Low Register" (Table IV) and "Filter Low Register" calibration (Table V), where the relevant digital data were sent from the relevant pins of the IC, respectively, using the writing loop.

TABLE IV
COMMUNICATION REGISTER CALIBRATION FOR "FILTER LOW REGISTER" OF AD7714

Pin	Communication register calibration for "Filter Low Register"																	
$\overline{CS}$	0	0	0	0	0	0	0	0	0	0	0	0	0	0	0	0	0	1
SCLK	1	0	1	0	1	0	1	0	1	0	1	0	1	0	1	0	1	1
DIN	0	0	0	0	0	1	1	1	1	0	0	1	1	0	0	0	0	0
$\overline{RESET}$	1	1	1	1	1	1	1	1	1	1	1	1	1	1	1	1	1	1
		DRDY		RS2		RS1		RS0		R/$\overline{W}$		CH2		CH1		CH0		

TABLE V
"FILTER LOW REGISTER" CALIBRATION OF AD7714

Pin	"Filter Low Register" calibration																	
$\overline{CS}$	0	0	0	0	0	0	0	0	0	0	0	0	0	0	0	0	0	1
SCLK	1	0	1	0	1	0	1	0	1	0	1	0	1	0	1	0	1	1
DIN	0	1	1	0	0	1	1	0	0	0	0	0	0	0	0	0	0	0
$\overline{RESET}$	1	1	1	1	1	1	1	1	1	1	1	1	1	1	1	1	1	1
		FS7		FS6		FS5		FS4		FS3		FS2		FS1		FS0		

The remaining 8-bit part of the 12-bit filter selection is determined through the "Filter low register" calibration. Filter selection determines the time between the two data consecutively generated at pin *DOUT* of the AD7714, in other words, the sampling frequency. Said time is also dependent on the frequency and gain selection of the crystal oscillator connected to pin *CLKIN* of the IC. However, calibration of said register may reduce noise by keeping sampling frequency low, but this would also impact the resolution of the ADC.

The 3rd operation step following "Filter Low Register" calibration involved communication register calibration for "Mode Register" (Table VI) and "Mode Register" calibration (Table VII), where the relevant digital data were sent from the relevant pins of the IC, respectively, using the writing loop. Channel selection in communication register calibration for "Mode Register" and gain selection in "Mode Register" calibration are determined based on the type of analog data to be measured (AC, DC current or voltage). As the study aims to read DC voltage using pin AIN1 of the IC, digital data 100 was used for channel selection and digital data 000 was used for gain selection during calibration.

TABLE VI.
TABLE VI COMMUNICATION REGISTER CALIBRATION FOR "MODE REGISTER" OF AD7714

Pin	Communication register calibration for "Mode Register"																	
$\overline{CS}$	0	0	0	0	0	0	0	0	0	0	0	0	0	0	0	0	0	1
SCLK	1	0	1	0	1	0	1	0	1	0	1	0	1	0	1	0	1	1
DIN	0	0	0	0	0	0	0	1	1	0	0	1	1	0	0	0	0	0
$\overline{RESET}$	1	1	1	1	1	1	1	1	1	1	1	1	1	1	1	1	1	1
		DRDY		RS2		RS1		RS0		R/$\overline{W}$		CH2		CH1		CH0		

On the other hand, bits *BO* and *FSYNC* are always set as logic 0 during "Mode register" calibration for calibration mode definition and gain selection. 8 different calibration settings exist for "Mode Register" calibration. However, self-scale calibration is a widely - used method to measure and improve the accuracy of delta-sigma ADCs. In addition, self-

scale calibration is a method where the ADC calibrates by measuring and adjusting itself. In such method, a pre-determined reference voltage is applied to the ADC and the voltage value read by the ADC is checked. Subsequently, the ADC utilizes an internal feedback loop set its parameters in order to equalize the measured value to the correct reference voltage.

TABLE VII
"MODE REGISTER" CALIBRATION OF AD7714

Pin	"Mode Register" calibration																	
$\overline{CS}$	0	0	0	0	0	0	0	0	0	0	0	0	0	0	0	0	0	1
SCLK	1	0	1	0	1	0	1	0	1	0	1	0	1	0	1	0	1	1
DIN	0	0	0	0	0	1	1	0	0	0	0	0	0	0	0	0	0	0
$\overline{RESET}$	1	1	1	1	1	1	1	1	1	1	1	1	1	1	1	1	1	1
		MD2		MD1		MD0		G2		G1		G0		BO		FSYNC		

The benefit of self-scale calibration is that it allows the ADC to automatically calibrate itself. Therefore, system designers are able to obtain more accurate and reliable results by allowing the ADC to calibrate itself rather than manually setting the parameters which affect the accuracy of the ADC.

The 4th operation step following "Mode register" calibration involved controlling of pin *DRDY* of the IC, which indicates whether "Data Register" 24-bit digital data is generated. The value at this pin should be logic 0 is data is generated, and logic one if data is not generated. When the value at this pin is Logic 0, the process progressed to the 5th operation step, where communication register calibration for "Data Register" is performed. Digital data determined for said calibration has been respectively sent from the relevant pins of the IC using the writing loop (Table VIII). Subsequently, the 24-bit data generated in the "Data Register" was determined at pin *DOUT* by the 24 Clock signal sent to pin *SCLK*, starting from the most significant bit (MSB). The decimal equivalent of obtained 24-bit data was determined, its DC voltage equivalent was calculated and recorded into the computer.

TABLE VIII
COMMUNICATION REGISTER CALIBRATION FOR "DATA REGISTER" OF AD7714

Pin	Communication Register Calibration for "Data Register"																	
$\overline{CS}$	0	0	0	0	0	0	0	0	0	0	0	0	0	0	0	0	0	1
SCLK	1	0	1	0	1	0	1	0	1	0	1	0	1	0	1	0	1	1
DIN	0	0	0	1	1	0	0	1	1	1	1	1	1	0	0	0	0	0
$\overline{RESET}$	1	1	1	1	1	1	1	1	1	1	1	1	1	1	1	1	1	1
		DRDY		RS2		RS1		RS0		R/$\overline{W}$		CH2		CH1		CH0		

TABLE IX
READING OF 24 BIT DATA FROM DOUT PIN

Pin	Reading Process			
$\overline{CS}$	0	0	DOUT check it	DOUT 1 ise x= x+$\underbrace{8388608}_{2^{23}}$
SCLK	1	0		
DIN	0	0		DOUT 0 ise x= x+0
$\overline{RESET}$	1	1		
$\overline{CS}$	0	0	DOUT check it	DOUT 1 ise x= x+$\underbrace{4194304}_{2^{22}}$
SCLK	1	0		
DIN	0	0		DOUT 0 ise x= x+0
$\overline{RESET}$	1	1		
.	.	.	.	.
.	.	.	.	.
$\overline{CS}$	0	0	DOUT check it	DOUT 1 ise x= x+2^0
SCLK	1	0		
DIN	0	0		DOUT 0 ise x= x+0
$\overline{RESET}$	1	1		
RESULT	Y= x.5/16777215=……Volt			

The user interface and block diagram of the LabVIEW software developed for programming the registers and retrieval and recording of 24-bit data are exhibited in Figure 5 and Figure 6, respectively.

The Reset and Setup buttons are clicked respectively in the user interface of the developed LabVIEW software. Clicking the Reset button resets the IC, while clicking the Setup button performs calibration for the registers of the IC. Subsequently, when pin *DRDY* is Logic 0 (when the light on the interface turns off), the 24-bit data is read from pin *DOUT* of the IC and recorded in the selected file. This operation is repeated until the software is stopped.

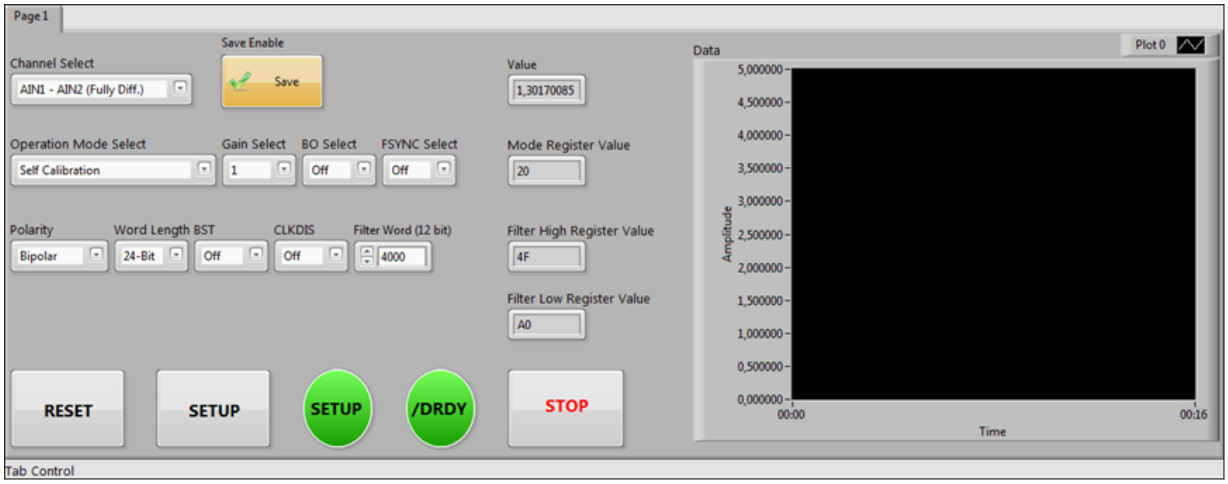

Figure 5. User interface of the developed LabVIEW software

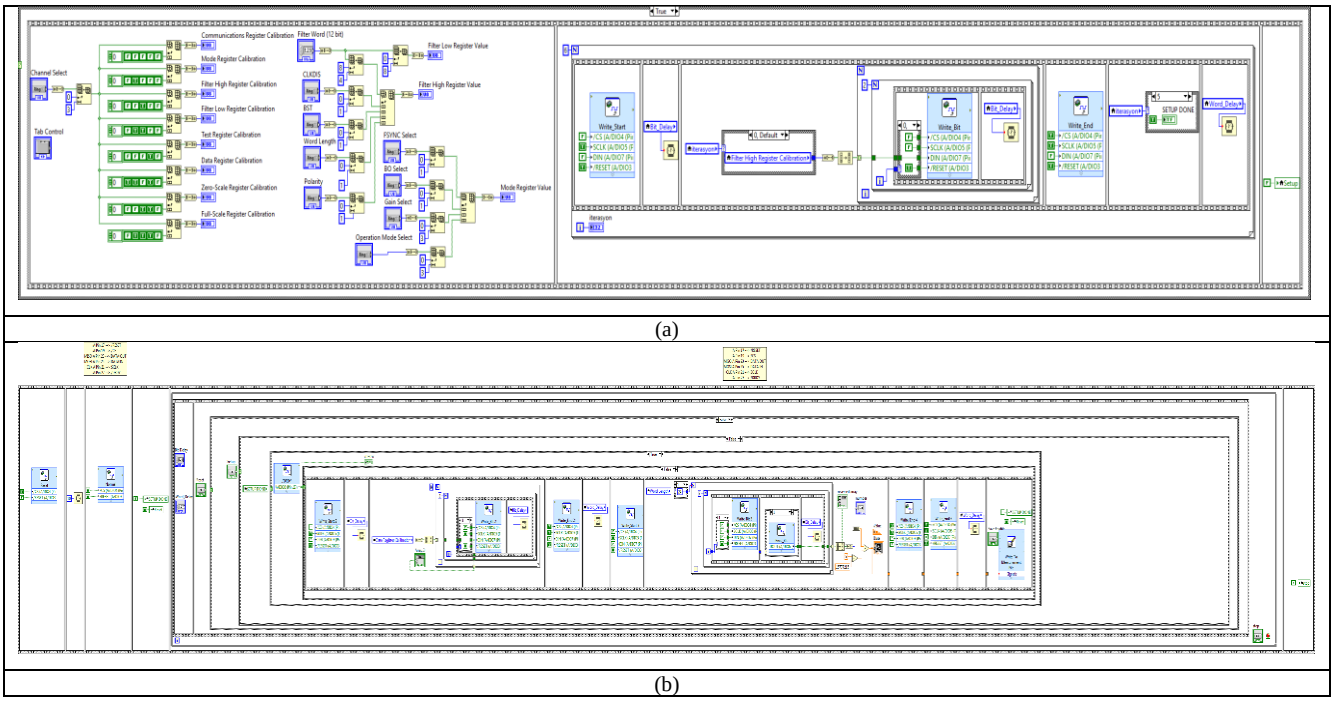

Figure 6. Block diagram of the developed LabVIEW software a) Programming of the Registers, b) Reading of the data in the Data Register

3. TYPE-A UNCERTAINTY OF THE MEASUREMENT SYSTEM: A SAMPLE CASE

A photo of the system developed under the study for DC voltage measurement is exhibited in Figure 7.

The performance of the measurement system developed within the scope of this study to reduce Type-A uncertainty in analog measurements by increasing digital resolution has been analyzed through a sample case. In the sample case, it was attempted to determine the magnetic flux density at a point 10 cm from a magnet by using a TE100 Fluxgate sensor. The analog voltage induced by the magnetic flux density at the sensor was transferred into computer medium and recorded with the use of said system. 8 measurements taken without changing sensor and magnet positions are exhibited in Table X. The same measurements were also conducted using a multimeter. The 8-bit resolution values measured and recorded with a multimeter in the study are given in Table 11.

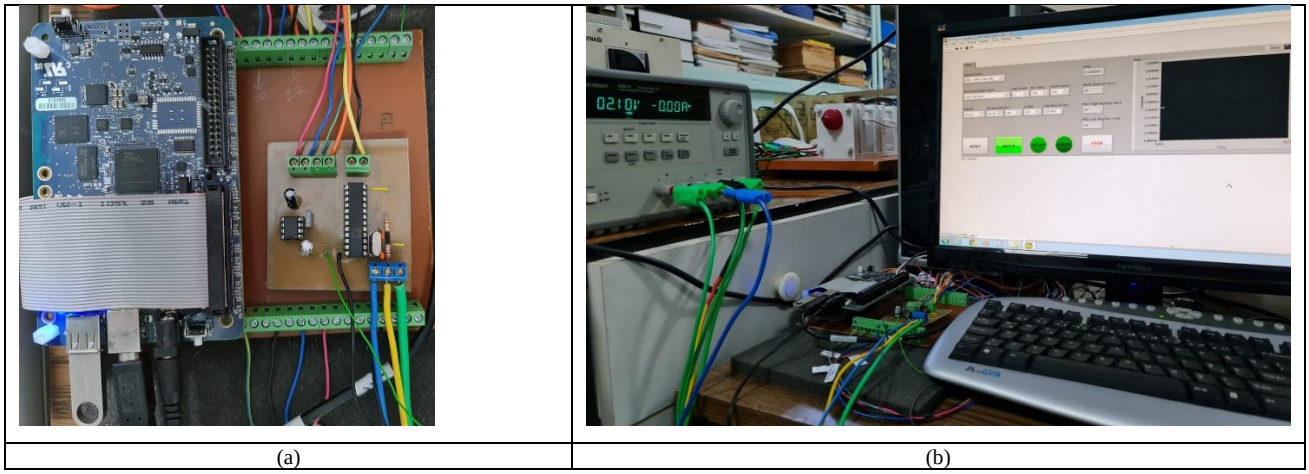

(a) (b)

Figure 7. a) Electronic connection of myRIO and AD7714, b) A photo of the measurement system.

TABLE X
TE100 FLUXGATE SENSOR VOLTAGE READINGS TAKEN USING THE MEASUREMENT SYSTEM AT 24-BIT RESOLUTION

Test No:	Measured Voltage Value (V)	Average Voltage Value (V)	Deviation from the Mean (V)	Standard deviation σ	Type A Uncertainty $U_A = \frac{\sigma}{\sqrt{n}}$
1	2,0999999105930275	2,099996632337369	0,000003278255658	0,000002447214930	0,000000865221136
2	2,0999987185000609		0,000002086162692		
3	2,0999972283838527		0,000000596046484		
4	2,0999963343141278		0,000000298023241		
5	2,0999945461746779		0,000002086162691		
6	2,0999984204768193		0,000001788139450		
7	2,0999954402444029		0,000001192092966		
8	2,0999924600119865		0,000004172325383		

TABLE XI
TE100 FLUXGATE SENSOR VOLTAGE READINGS TAKEN USING A MULTIMETER AT 8-BIT RESOLUTION

Deney No:	Ölçülen Gerilim Değeri (V)	Ortalama Gerilim Değeri (V)	Ortalamadan Sapma (V)	Standart Sapma σ	A Tipi Belirsizlik $U_A = \frac{\sigma}{\sqrt{n}}$
1	2,0980392	2,08088235	0,01715685	0,01636319	0,00578526
2	2,0784314		0,00245095		
3	2,0588235		0,02205885		
4	2,0784314		0,00245095		
5	2,0980392		0,01715685		
6	2,0784314		0,00245095		
7	2,0588235		0,02205885		
8	2,0980392		0,01715685		

Comparison of Table X and Table XI indicated that Type-A uncertainty calculated according to the GUM model increases by 6687 in repetitive measurements when resolution is decreased. This clearly demonstrates the impact of resolution on Type-A uncertainty. It is also an indication that Type-A uncertainty in a measurement would change by changing the measurement system, even though the sensor and the sensed are the same. Furthermore, in comparison to the use of a multimeter, direct transfer of the measurements into computer medium at 50 kS/s speed during the study helped reduction of total uncertainty, thanks to the elimination of reading errors by operators.

4. CONCLUSION AND DISCUSSION

This study provides a detailed examination of the delta-sigma ADC's procedures for the creation of digital data at 24-bit resolution, as well as the transfer of said generated digital data into computer medium via the myRIO module. A LabVIEW-based software has been developed to perform ADC

register settings and to retrieve 24-bit data from the ADC output. In addition, performance of the system developed under this study was tested for repetitive measurements using a sample case, and its effectiveness in reduction of Type-A uncertainty has been proved. Considering the fact that the measurement system eliminates uncertainty reasons such as operator errors at high-speed measurements, total uncertainty to be determined according to the GUM model would also be reduced. Moreover, the developed measurement system is compatible with all sensors which generate analog voltage output based on changing physical characteristics. The system is capable of detecting and recording changes as little as 298μV at the analog output. Today, anomalies in the horizontal component of the earth's magnetic field particularly cause deviations in magnetic sensors at μV levels, which escalates the need for such measurement systems with low uncertainty.

REFERENCES

[1] J. C. Damasceno, P. R. Couto, "Methods for evaluation of measurement uncertainty," In Metrology, London, IntechOpen, pp. 9-28, 2018.

[2] M. S. B. Fernández, "Evaluation of uncertainty in the measurement of the stress-optic coefficient," Journal of Non-Crystalline Solids, 607, 122249. 2023.

[3] T. Dorst, T. Schneider, S. Eichstädt, A. Schütze, "Influence of measurement uncertainty on machine learning results demonstrated for a smart gas sensor," Journal of Sensors and Sensor Systems, 12(1), pp. 45-60, 2023.

[4] J. Huang, Y. Li, B. Jiang, L. Cao, "Analysis of measurement uncertainty of a surface acoustic wave micro-pressure sensor," Measurement and Control, 52(1-2), pp. 116-121, 2019.

[5] H. Zangl, K. Hoermaier, "Educational aspects of uncertainty calculation with software tools," Measurement, 101, pp. 257-264, 2017.

[6] Z. Tan, C. H. Chen, Y. Chae, G. C. Temes, "Incremental delta-sigma ADCs: A tutorial review," IEEE Transactions on Circuits and Systems I: Regular Papers, 67(12), pp. 4161-4173, 2020.

[7] E. Kabalcı, Y. Kabalcı, P. Siano, "Design and implementation of a smart metering infrastructure for low voltage microgrids," International Journal of Electrical Power & Energy Systems, pp. 134, 107375, 2022.

[8] K. Nam, H. Kim, G. Choi, M. Yoo, H. Ko, "Low-noise delta-sigma analog front end with capacitor swapping technique for capacitive microsensors," Measurement and Control, 55(5-6), pp. 239-246, 2022.

[9] J. Jovanović, D. Denić, "Mixed-mode method used for Pt100 static transfer function linearization." Measurement Science Review, 21(5), pp. 142-149, 2021.

[10] N. Jeelani. A. Hamid Bhat, "Constant switching frequency-based delta-sigma modulation of single-phase AC–AC zeta converter." International Journal of Circuit Theory and Applications, 51(1), pp. 97-114. 2023.

[11] J. M. Binder, A. Stark, N. Tomek, J. Scheuer, F. Frank, K.D. Jahnke, ... & F. Jelezko, "Qudi: A modular python suite for experiment control and data processing," SoftwareX, 6, pp. 85-90, 2017.

[12] T. Drevinskas, M. Kaljurand, A. Maruška, "Capacitance-to-digital: A single chip detector for capillary electrophoresis," Electrophoresis," 35(16), pp. 2401-2407, 2014.

[13] S. Billa, A. Sukumaran, S. Pavan, "Analysis and design of continuous-time delta–sigma converters incorporating chopping," IEEE Journal of Solid-State Circuits, 52(9), pp. 2350-2361, 2017.

[14] S. Pavan, R. Schreier, G. C. Temes, "Understanding delta-sigma data converters," Wiley-IEEE Press, 2017, pp.584.

[15] R. Theertham, P. Koottala, S. Billa, S. Pavan, "Design techniques for high-resolution continuous-time delta–sigma converters with low in-band noise spectral density," IEEE Journal of Solid-State Circuits, 55(9), pp. 2429-2442, 2020.

BIOGRAPHIES

Hakan Citak was born in Romanshorn, Switzerland in 1969. He received the B.S. and Ph.D. degrees from the Department of Electric Education, Institute of Science, Marmara University, Istanbul, Turkey, in 1995 and 2014, respectively. He is currently working for the Balikesir Vocational High School, Electric Program, Balikesir University, Balikesir. His research interests are magnetic sensors and magnetic anomaly. He is holds two patents.

Sabri Bicakci was born in Balikesir, Turkey in 1982. He received the B.S. degree in electronics engineering from the Erciyes University, Kayseri, in 2005, M.S. degree in electrical and electronics engineering from the Balikesir University, Balikesir, in 2009 and the Ph. D. degree in mechanical engineering from Balikesir University, Balikesir, in 2012.

From 2005 to 2015, he was a Research Assistant with Electrical and Electronics Engineering Department, Balikesir University.

Since 2015, he has been an Assistant Professor with the Mechatronics Engineering Department, Balikesir University. His research interest includes robotics and control systems.

European Journal of Technique

journal homepage: https://dergipark.org.tr/en/pub/ejt

Vol.13, No.1, 2023

Electroanalytical Investigation of Cancer Chemotherapy Drug Vinorelbine on Disposable Pencil Graphite Electrode in Surfactant Media by Voltammetric Method*

Günay Önal[1*], Abdulkadir Levent[2], and Zühre Şentürk[3]

[1*] Batman University, Health Services Vocational College, 72100 Batman, Turkey (gunayturmus@hotmail.com).
[2] Batman University, Faculty of Arts and Sciences, Department of Chemistry, 72100 Batman, Turkey (leventkadir@hotmail.com).
[3] Van Yüzüncü Yıl University, Faculty of Science, Department of Analytical Chemistry, 65080 Van, Turkey (zuhresenturk@hotmail.com).

ARTICLE INFO

Received: March., 02. 2023
Revised: March., 30. 2023
Accepted: March., 30. 2023

Keywords:
Vinorelbine
Pencil graphite electrode
Square-wave adsorptive stripping voltammetry
Cationic surfactant
Real samples

Corresponding author: *Günay ÖNAL*
*It is produced from PhD thesis of Günay Önal

ISSN: *2536-5010* | e-ISSN: *2536-5134*

DOI: https://doi.org/10.36222/ejt.1259355

ABSTRACT

Vinca alkaloids have been used in the treatment of human cancers for over 50 years. In this study, a new application of disposable pencil graphite electrode is presented for the determination of Vinorelbine, which is one of the semisynthetic derivatives of *Vinca* alkaloids.

The electrochemical properties of Vinorelbine were investigated using cyclic voltammetry and adsorptive stripping voltammetry in aqueous solutions over the pH range of 2.0-12.0 in the absence and presence of anionic and cationic surfactants. Employing square-wave stripping mode (after 120 s accumulation at +0.0 V) in Britton-Robinson buffer pH 10.0 containing 3×10^{-3} M cationic surfactant, TBAB (tetra-*n*-butylammonium bromide), there was an excellent correlation between oxidation peak current at +0.75 V (vs. Ag/AgCl) and Vinorelbine concentration in range of 2.3×10^{-8} – 5.8×10^{-6} M. The limit of detection was found to be 7.5×10^{-9} M (as base form, 5.8 ng mL^{-1}). The applicability of the developed technique was tested in pharmaceutical formulations and spiked human urine samples.

1. INTRODUCTION

One of the biggest global public health issues, cancer has a negative impact on people's health and quality of life. Therefore, it is undeniable that the interest in drugs for cancer treatment has increased. On the other hand, in addition to patient safety during, the administration of drugs used in cancer treatment due to their possible toxic properties, it is crucial to maintain a safe working environment and to safeguard the health professionals who provide the treatment from the possibility of coming into touch with this class of medications. At the same time, it is extremely important to develop new methods for the determination of antineoplastic drugs in different environments.

Although some of the *Vinca* alkaloids in the herbal antineoplastic drugs class have been marketed for more than 50 years for use in cancer treatment, little is known about their mechanism of action and metabolism. Vinorelbine is a semi-synthetic derivative of Vinblastine, one of the *Vinca* alkaloids, also known as Anhydrovinblastine (see Figure 1 for its chemical structure).

The molecule was discovered by Pierre Potier and his research group (France) in 1980, and was developed in 1989 under the trade name Navelbin® IV (Vinorelbine ditartrate) for the treatment of bronchial cancer. In 1991, it was approved for the treatment of non-small-cell lung cancer. Vinorelbine is currently used in the treatment of different cancer diseases in combination with other chemotherapeutic drugs. It has been shown to be especially effective in the treatment of advanced breast cancer and non-small-cell lung cancer **[1-3].**

According to the literature review, it has been seen that liquid chromatography (LC) has been the most widely used method in the last two decades for the determination of *Vinca* alkaloids in general, Vinorelbine in particular, from different media (pharmaceutical forms, environmental samples and biological samples such as urine, blood, tissue). Mass spectrometry (MS) is preferred as a detection system especially for pharmacokinetic studies **[4-8]**. Although LC has high

sensitivity, selectivity and accuracy, it requires experienced personnel, long and laborious pre-separation processes, organic solvents, high cost devices (especially in the detection unit).

On the other hand, despite the redox active groups in the molecular structure of *Vinca* alkaloids, very few studies have been reported on their electrochemical properties due to their very complex structure [9-15]. Considering that voltammetry, which is one of the electroanalytical methods, is simple, fast, low cost, low sensitive to matrix effect and suitable for on-site analysis; it is clear that this method will be an alternative candidate for the determination of these antineoplastic drugs in the near future [16-18].

According to our best knowledge, there is only one study on the voltammetric characteristics of Vinorelbine [19]. In that study performed in 1993, the electrochemical oxidation of this molecule was investigated using cyclic and differential pulse voltammetric techniques at the surface of glassy carbon (GC) electrode in a wide pH range (1.2-12.8). Its results were revealed that the anodic oxidation mechanism of Vinorelbine is very complex and pH-dependent.

In the study presented here, the redox properties of Vinorelbine will be evaluated using commercially available graphite pencil leads as electrode material. Beginning from the end of the 1990s, pencil graphite (PG) electrodes has become an alternative to other solid electrodes due to their several outstanding properties, such as disposability, good mechanical stability, high electrochemical reactivity, low technology, low cost, and ease of preparation. Because PG electrodes are single-use, cleaning procedures are not required. Commercial mechanical pencil leads of different hardness and diameter (as a mixture of natural graphite and clay) are used in the design of PG electrodes [20-25].

Apart from the electrode material, one of the simple and inexpensive ways to increase the sensitivity and selectivity of the voltammetric method is to use surfactants at their submicelle concentrations in the electrochemical cell. [26]. Our research group performed the determination of many hydrophilic or hydrophobic compounds in surfactant-containing solutions using different carbon-based electrodes by voltammetric method. [27-31].

In view of the only one data on the electrochemical investigation of Vinorelbine, the aim of this study is to investigate the electrochemical oxidation of this compound using PG electrode in the presence of both anionic and cationic surfactants. Next, the applicability of the voltammetric approach will be tested by the analysis of pharmaceutical formulations and spiked human urine samples.

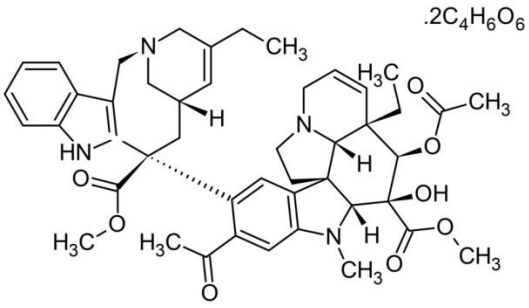

Figure 1. Molecular structure of Vinorelbine ditartrate

2. EXPERİMENTAL

2.1. Apparatus

The voltammetric measurements were performed using a Autolab PGSTAT 128N potentiostat/galvanostat (EcoChemie, the Netherlands) driven by Nova 1.1 software, and BAS C3 solid electrode cell stand unit (Bioanalytical System, BAS, USA). All experiments were conducted in a 10-mL one-compartment electrochemical cell consisting of a PG working electrode, an Ag/AgCl (3M NaCl) reference electrode (BAS, MF-2052, USA), and platinum wire auxiliary electrode (BAS, MF-1032, USA). The pH values of solutions were measured using the pH meter (WTW inoLab720) equipped with the glass-reference electrode.

For the preparation of PG electrode, mechanical pencil (Model Rotring T 0.5, Germany) as a holder and soft pencil leads (20% of clay + 74% of graphite + 6% of polymeric wax as a binder) with 6.0 cm of length and 0.5 mm diameter (Model Tombow 0.5/2B, Japan) were purchased from a bookstore. A similar way to that used in previous work [21] was applied for the electrode design. For electrical contact, the metallic head of the pencil body and the outer metallic handle were attached with copper wire. Before each measurement, 12 mm of pencil lead (total) was dipped into the solution, and then PG electrode was subjected to an electrochemical pretreatment. For this purpose, a potential of +1.4 V was applied for 60 s in selected supporting electrolyte without stirring (in the case of CV studies, at +1.8 V for 60 s). Each voltammetric recording was carried out using a new pencil lead. Following the way in our previous work [31], the effective surface area of the designed PG electrode was calculated to be 0.159 cm^2.

2.2. Chemicals and solutions

The analytical standard of Vinorelbine (as ditartrate salt, purity ≥90%) was purchased from Sigma-Aldrich. As the solubility of this compound is limited in water, dimethylsulfoxide (DMSO) was used in the preparation of its stock solution (1×10^{-3} M). The prepared solutions were stored in a refrigerator at +4 ºC, away from light when not in use. The less concentrated solutions of this compound used in calibration studies and sample analysis were prepared from the stock solutions by dilution of appropriate volume with supporting electrolyte. Analytical-grade reagents and ultrapure water (resistivity ≥ 18.2 MΩ cm) supplied from a Millipore Milli-Q purification system (USA) were used for the preparation of supporting electrolytes namely Britton-Robinson (BR) buffer (each constituent having a final concentration of 0.04 M, pH 2.0-12.0), phosphate buffer (0.1 M, pH 3.0 and 7.4) and acetate buffer (0.1 M, pH 4.8). The surfactants tested were cationic type, tetra-*n*-butylammonium bromide, TBAB (99%, Merck) and anionic type, sodium dodecylsulfate, SDS (90%, Merck). Their stock solutions (0.1 M) were prepared in water.

2.3. Measurement procedures

In preliminary studies on the electrochemical behavior of Vinorelbine, the cyclic voltammetry (CV) was applied on the surface of PG electrode. Then, the performance characteristics of the square-wave adsorptive stripping voltammetry (SW-AdSV) were determined at different pH values in the absence and presence of surfactants. Later, this technique was applied to the real samples.

The general procedure for the stripping voltammetric determination of Vinorelbine can be summarized as follows: The three-electrode system was immersed in a selected supporting electrolyte (at a desired pH) containing a selected concentration of Vinorelbine. A chosen accumulation potential (optimal, 0.0 V) was then applied to the surface of PG electrode for a suitable accumulation period of time (optimal, 120 s) while the solution was stirred at 750 rpm. Then stirrer was stopped and the solution was allowed to settle for 10 s. Afterwards, the voltammograms were recorded in a certain potential scanning range (from 0.0 V to +1.4 V) in the positive direction using the SW waveform.

2.4. Sample Preparation

For the application of the method to the pharmaceutical dosage forms, Navelbine® injectable solutions (50 mg 5 mL^{-1} Vinorelbine) were purchased from the local pharmacies. Each vial contains 69.25 mg of Vinorelbine ditartrate equivalent to 50 mg of Vinorelbine. The content of two ampoules of this formulation was mixed thoroughly. The required volume was directly transferred to the electrochemical cell containing 10 mL of Britton-Robinson buffer (pH 10.0) containing 3×10^{-3} M TBAB. Quantifications were performed using the calibration curve developed for the pure electrolyte, from the related regression equation.

Urine sample was collected in plastic container from a healthy non-smoker and drug-free volunteer on an empty stomach and just before the experiments. The sample was centrifuged at 5000 rpm for 10 minutes to remove unknown endogenous chemicals. 50 µL of urine from the clear upper part was pipetted into a 10 mL-glass tube and then spiked with 10 µL of 2×10^{-4} M Vinorelbine (model human urine sample). This sample was then completed to the volume with BR buffer (pH 10.0) unless otherwise stated. This final mixture was transferred into the electrochemical cell and subjected to SW-AdSV measurements. The determination of Vinorelbine in spiked urine sample was carried out using standard addition method with respective volumes of 45, 60, 70, 80 and 90 µL of Vinorelbine solution used above, and stripping voltammograms were recorded after each addition. The Vinorelbine-free part of the urine sample was used as a blank.

Each experiment of pharmaceuticals and urine samples was repeated three times.

3. RESULTS AND DISCUSSION

In order to understand the electrochemical response of Vinorelbine on the surface of PG electrode, the experiments were carried out using CV and SW-AdSV techniques in aqueous or surfactant-containing aqueous solutions (Note: Since the DMSO concentration is kept at ~1% (v/v) and below in the recording of CV and AdSV curves, the solutions used are expressed as "aqueous solution").

3.1. Cyclic voltammetry in aqueous solutions

At the beginning of the study, two consecutive CV curves (CVs) of 2.3×10^{-5} M Vinorelbine in BR buffer at pH 10 (the most suitable medium for analytical purposes, as will be shown later) were recorded within the potential window from 0.0 V to +1.4 V at scan rate of 100 mVs^{-1} (Figure 2). As can be seen from the first positive-going scan, the molecule was oxidized in two distinctly separated steps at about +0.73 V (Ia) and +1.00 V (IIa) with their peak currents of 11.18 µA (Ia) and 10.68 µA (IIa). When the potential scanning was continued in the cathodic region after the oxidation of the molecule, no reduction steps were observed in the studied potential range. It suggests the totally irreversible electrode reaction of Vinorelbine. On the second forward scan, the signal of the Ia was greatly reduced and the IIa step was disappeared. This formation is an important indication that the oxidation products of Vinorelbine are strongly adsorbed on the electrode surface. A similar observation was also reported previously for the electrochemical properties of Vinorelbine using GC electrode [19].

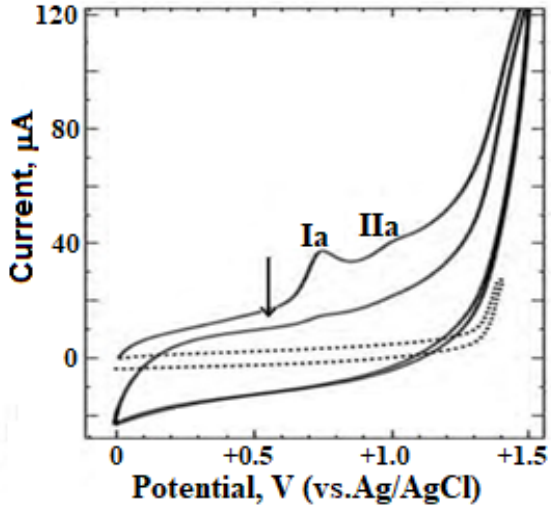

Figure 2. The repetitive CVs of 2.3×10^{-5} M Vinorelbine in BR buffer (pH 10.0). Electrode, PG; potential scan rate, 100 mVs^{-1}. Dashed lines, supporting electrolyte. Arrow indicates order of the recorded scans

In order to examine the effect of potential scan rate on the electrochemical oxidation of Vinorelbine molecule, CVs of 4.6×10^{-5} M Vinorelbine solution were recorded by increasing this parameter from 50 to 700 mVs^{-1} using the above conditions (Figure 3). As the scan rate gradually increased, an increase in the peak currents of both Ia and IIa, as well as a shift in peak potentials to slightly more positive values were observed. This supports the above-mentioned irreversibility of the electrode reaction [32].

As seen clearly from the figure, the first oxidation step (Ia) became sharper and measurable, so this step was chosen as the analytical signal in the continuation of the study.

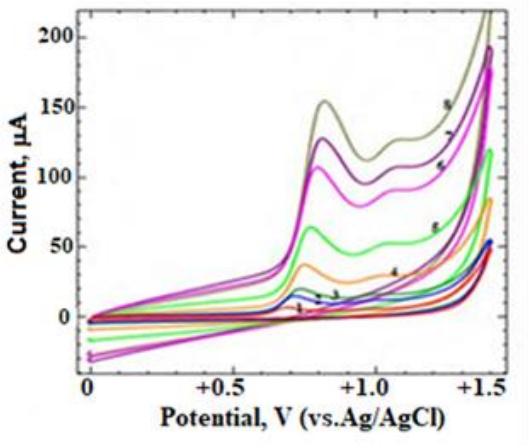

Figure 3. The CVs of 4.6×10^{-5} M Vinorelbine recorded at various scan rates: (1) 50, (2) 100, (3) 200, (4) 300, (5) 400, (6) 500, (7) 600, (8) 700 mVs^{-1}. Electrode, PG; supporting electrolyte, BR buffer (pH 10.0).

Plotting the oxidation peak current (i_p) vs. scan rate (v) gave up a straight line, which demonstrates an adsorption behavior of Ia in this medium. The equation is expressed below:

i_p (μA) = 0.12 v (mV s^{-1}) – 5.28 (r = 0.998)

On the other hand, it was also observed a linear relationship between i_p and $v^{1/2}$ according the following equation, which suggests a diffusional behavior:

i_p (μA) = 4.11 $\sqrt{v}$ (mV s^{-1}) – 34.22 (r = 0.977)

However, as can be seen from the r value of equation, the linearity in this relationship is not very good between 50 and 700 mV s^{-1}, and deviations are observed at low (50 and 100 mV s^{-1}) and high (600 and 700 mV s^{-1}) scan rate values. This case shows that the diffusion mechanism is also involved in the electrochemical reaction of Vinorelbine, but it is effective at moderate scan rates.

In order to understand the oxidation of Vinorelbine on the PG electrode, the data through a plot of log i_p vs. log v were also analyzed, according to the following equations:

log i_p (μA) = 1.30 log v (mV s^{-1}) – 1.74 (r = 0.996)

The slope value in the related equation is greater than 1.0, which proves that the oxidation process is controlled by adsorption [33]. In the light of these findings, the electrochemical behavior of Vinorelbine on the PG electrode is mainly controlled by adsorption. On the other hand, it can be said that diffusion also contributes using the scan rates between 200-500 mVs^{-1}.

Meanwhile, the relationship between E_p and log v can be expressed as follows in the range of potential scan rate studied:

E_p (V) = 0.072 log ν (mV s^{-1}) + 0.80 (r = 0.982)

For an irreversible electrode process [32], the relationship between E_p and v is defined as:

$E_p = E^0 + (2.303RT / \alpha nF) \log (RTk^0 / \alpha nF) + (2.303RT / \alpha nF) \log v$

In the equation, α is the charge transfer coefficient and n is the number of electrons transferred in the redox reaction. R (8.314 J K^{-1} mol^{-1}), T (298 K) and F (96480 C mol^{-1}) are known constants. The slope value in the E_p / log v relationship given above is 0.072. Using the related equation, the αn value is calculated as 0.81. For most completely irreversible electrode systems, the α value can be accepted as 0.5. Thus, the value n = 1.64 (≈ 2) is obtained. This value shows that two electrons per molecule are transferred for the irreversible oxidation process of the Vinorelbine molecule at the surface of PG electrode. The result obtained is consistent with the SW-AdSV finding performed in BR buffer using a modified carbon paste electrode on Vincamin, one of the indole alkaloids of the *Vinca minor* plant [13].

3.2. Stripping voltammetry in aqueous and aqueous-surfactant solutions

In the light of the above findings, in this part of the study, the electrochemical oxidation of Vinorelbine molecule was investigated in surfactant-free or surfactant-containing aqueous solutions.

3.2.1. Effect of solution pH and surfactant

At first, this part of the study was focused to examine the effect pH of the supporting electrolyte in order to understand the optimum electrochemical responses of Vinorelbine molecule. For this, using the SW-AdSV technique (accumulation potential, 0.0 V and accumulation period of time, 60s) the voltammograms of 2.3×10^{-5} M Vinorelbin were recorded in BR buffer at the range of pH 2.0-12.0 in the absence and presence of surfactants (Figure 4).

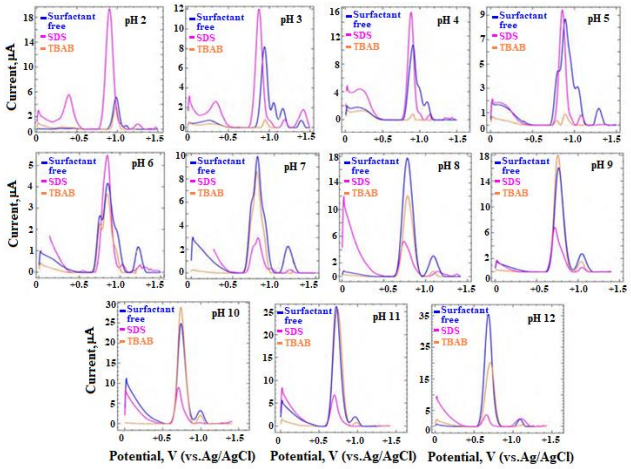

Figure 4. SW-AdSV curves of 2.3×10^{-5} M Vinorelbine in BR buffer (pH 2.0-12.0) in the absence and presence of anionic (SDS) and cationic (TBAB) surfactants. Electrode, PG; accumulation potential 0.0 V; accumulation period of time, 60 s; surfactant concentration, 5.0×10^{-3} M; SW variables: step potential, 5 mV; frequency, 25 Hz; pulse amplitude, 20 mV.

As can be seen from the voltammograms obtained in surfactant-free BR buffer solutions (shown as blue line), the anodic oxidation mechanism of the Vinorelbine molecule is pH dependent and probably involves many complex electron transfer processes. Especially in the pH range of 3.0-7.0, a large number of shoulder-shaped oxidation steps appeared and it was very difficult to evaluate these steps. Findings obtained in repeated experiments in acetate (pH 4.8) and phosphate (pH 3.0 and 7.4) buffers were in agreement with the findings of BR buffer corresponding to the same pH values (data not shown). In strongly acidic solutions (pH 2.0) and solutions above pH 7.0, these steps were separated from each other and their significance increased. Brett et al. [19] also obtained similar findings for Vinorelbine in the study performed on GC electrode.

The peak potentials shifted to the lower positive values as the pH values increased. This observation is proof that proton transfer is also involved in the oxidation process of Vinorelbine. When the relationship between the peak potential (E_p) and pH was examined, two linear regions with different slope values were obtained in the wide pH range studied:

E_p (mV) = -31.2 pH + 1037 (r = 0.992) (pH 2.0 to 6.0)

E_p (mV) = -19.0 pH + 930 (r = 0.999) (pH 7.0 to 11.0)

These findings were also consistent with those of obtained for Vincamin [13]. The reason why the correlation coefficient (r) value of the relationship in the pH 2.0 – 6.0 range is not very good is due to the possible reading error of the fundamental oxidation peak intensity due to the peak splits in the relevant range.

Due to the complexity of molecular structures of *Vinca* alkaloids, their detailed oxidation pathways were not well documented so far. Considering the electrochemical behavior of indoline-alkaloids with structural similarity [9,12], it can be assumed that the oxidation of Vinorelbine molecule involves multi-step electron transfer with the loss of protons. Subsequently, chemical reaction products (dimers or polymers) are strongly adsorbed on the electrode surface forming an inactive film.

From the Fig. 4, i_p / pH findings show that the peak intensity reached the highest value in alkaline solutions. Hence, these media can be employed for analytical use.

In the following part of the work, the applicability of the PG electrode was examined in surfactant-containing solutions. For this purpose, keeping the Vinorelbine concentration at 2.3×10^{-5} M, two kinds of surfactants with opposite charges, namely SDS (anionic) (shown as pink line) and TBAB (cationic) (shown as orange line) were added to BR buffer (pH 2.0-12.0) having a concentration of 5.0×10^{-3} M (Fig 4). When voltammograms in surfactant-free and surfactant-containing solutions were examined, it was observed that the effectiveness of SDS on the peak morphology and intensity of Vinorelbine was very high in acidic solutions (pH 2.0-6.0). On the other hand, the peak potentials shifted to less positive values in this media. Against this, in acidic solutions (pH≤5.0) containing TBAB, the peak intensity was much lower than in solutions without surfactant. In the case of this surfactant, it was observed highest peak intensity at pH 9.0 and 10.0. There was no significant change in peak potentials when cationic surfactant is used.

Since there is one hydroxyl group and four nitrogen-containing regions on the Vinorelbine (Figure 1), this molecule probably should have five pK_a values. However, in aqueous solutions the protonated and nonprotonated structures of the *Vinca* alkaloids (including Vinorelbine) have not been fully elucidated until now. This may be due to the difficulty of determining their pK_a values specific to nitrogen regions. In the Drugbank database **[34]**, the predicted pK_a values of Vinorelbine have been reported as 10.87 (strongest acidic) and 8.66 (strongest basic). Based on the above information, it could be expected that Vinorelbine molecule will exist fully positively charged, mixture of neutral (lipophilic)/positively charged, and neutral species depending on the pH of the environment.

On the other hand, in aqueous solutions containing anionic (in our case SDS) or cationic (in our case TBAB) surfactants below their critical micelle concentrations ($CMC_{SDS} = 8.2\times10^{-3}$ M **[35]**, CMC_{TBAB} = 0.25 M **[36]**), the long hydrophobic tails of their surface micelles can be adsorbed on hydrophobic surface of substrate (in our case PG surface). Thus, they form negatively or positively charged hydrophilic films oriented towards the water bulk phase. Therefore, in strongly acidic solutions containing SDS, the peak intensity was very high due to the electrostatic interaction between the cationic Vinorelbine molecules and the negatively charged head groups of the SDS micelles on the electrode surface. As the acidity of the solutions decreased, the positive charge of the Vinorelbine molecule gradually decreased, thus the peak intensity decreased. If the positively charged surfactant, TBAB, was added to acidic solutions, a decrease in the peak intensity of the Vinorelbine molecule was observed compared to the solutions without surfactant, since the electrostatic forces would work in the opposite direction. The increase in peak intensity of neutral form of Vinorelbine (partially or completely) in TBAB-containing-solutions at pH, 9.0 and 10.0 can be explained by a different mechanism called coadsorption (surface solubilization) **[37-39]**. Reported studies have shown that this mechanism usually takes place in the presence of cationic surfactant with long hydrophobic tail.

When surfactant-free and surfactant-containing solutions were examined, the highest peak currents were reached at pH 2.0 in the presence of SDS, at pH 10.0 in the presence of TBAB, and at pH 12.0 without surfactant. It should be underlined at this point that one of these three media at different pH values could be selected for the determination of Vinorelbine in order to reduce or eliminate the effect of interference from real samples. Considering the effect of the surfactant concentration on the electrode response (will be given later), it was decided to work using BR buffer containing TBAB in the continuation of the work.

3.2.2. Effect of accumulation conditions and other operating parameters

Taking into account the adsorptive properties of Vinorelbine on the PG surface, it was examined the influence of accumulation parameters (accumulation period of time, t_{acc} and accumulation potential, E_{acc}) for 5.5×10^{-6} M Vinorelbine in BR buffer solution containing 5.0×10^{-3} M TBAB (data not shown). The effect of t_{acc} on the analytical signal was investigated in the range of 0-210 s by keeping the E_{acc} value constant at 0.0 V. It was observed a linear increase in the peak current of Vinorelbine in the range of 0-120 s. This value almost remained stable beyond this range. After fixing the t_{acc} at 120 s, the effect of E_{acc} was also investigated over the potential range from 0.0 to +0.6 V. In this case, the oxidation peak current decreased as this parameter increased. After these findings, further experiments were carried out in the continuation of the study by applying E_{acc} of 0.0V for 120 s.

The attention was finally turned to optimize SWV operating parameters such as frequency (f = 5-45 Hz), step potential (ΔE_s = 1-13 mV) and pulse amplitude (ΔE_{sw} = 10-70 mV) under the above conditions (data not presented). To obtain highest sensitivity and better peak shape, the optimized values were: f, 30 Hz; ΔE_s, 11 mV; and ΔE_{sw}, 40 mV.

3.2.3. Effect of surfactant concentration

After optimizing the adsorption and instrumental variables in previous sections, finally the effect of TBAB concentration was investigated in order to provide the best experimental condition for the analytical study of Vinorelbine. By keeping the Vinorelbine concentration constant at 5.5×10^{-6} M, TBAB in the concentration range of 1×10^{-4} M - 1×10^{-2} M was added to the BR buffer (pH 10) solution and the SW-AdSV curves were recorded. As can be seen in Fig. 5, the oxidation peak current of Vinorelbine increased with TBAB concentration up to 3×10^{-3} M. At higher concentration above 3×10^{-3} M, it started to decrease. As a result, the experiments in the analytical examination were carried out by keeping the TBAB concentration constant at 3×10^{-3} M. When this surfactant concentration was present in solution, Vinorelbine signals were increased by approximately 50% compared to solutions without surfactant.

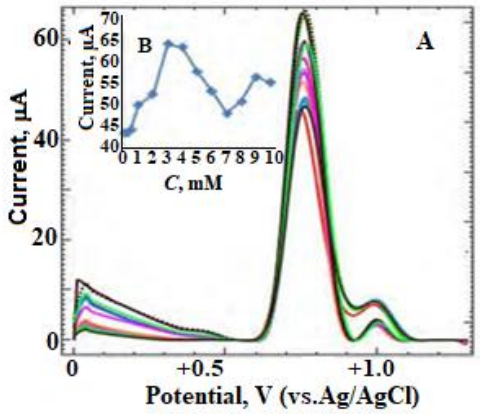

Figure 5. SW-AdSV curves of 5.5×10^{-6} M Vinorelbine recorded in BR buffer (pH 10) containing various concentrations of TBAB (1×10^{-4} M - 1×10^{-2} M). Electrode, PG; accumulation potential 0.0 V; accumulation period of time, 120 s; SW variables: step potential, 11 mV; frequency, 30 Hz; pulse amplitude, 40 mV. Black line, 0 mM TBAB; dashed line, 3 mM TBAB. Inset: plots of i_p vs. the concentration of TBAB.

3.3. Analytical application in aqueous-surfactant solutions

We should first point out that, there is no study on the quantification of Vinorelbine by voltammetric method in the literature so far.

Using the chosen experimental and instrumental conditions presented above, analytical applicability of PG electrode in combination with SW-AdSV was tested in 3×10^{-3} M TBAB-containing BR buffer at pH 10 by plotting the peak currents as a function of Vinorelbine concentration. The relevant stripping voltammograms and corresponding calibration graph are given in Figure 6.

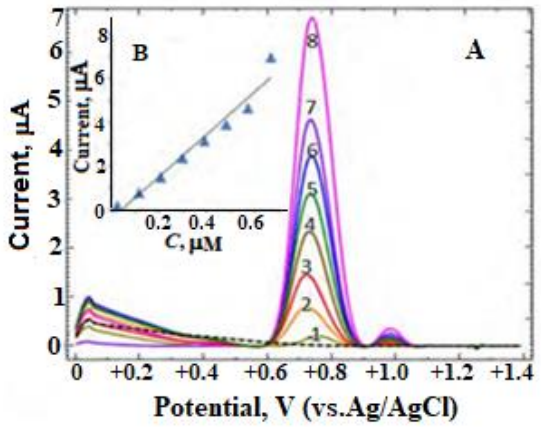

Figure 6. SW-AdSV curves of for Vinorelbine concentration levels of (1) 0.023, (2) 1.15, (3) 2.07, (4) 2.99, (5) 3.91, (6) 4.83, (7) 5.75, (8) 6.67 µM recorded in BR buffer (pH 10) containing 3×10^{-3} M TBAB. Dashed line, supporting electrolyte. Inset: plots of i_p vs. the concentration of Vinorelbine. The other operating conditions are as shown in Fig. 5.

It was obtained a linearity between the oxidation peak currents on the Vinorelbine concentration from 2.3×10^{-8} to 5.8×10^{-6} M (as base form, 17.9 – 4518 ng mL^{-1}). The SWV response at a potential of +0.75 V increased proportionally with the concentration of Vinorelbine (Fig. 6, inset) to present a highly linear calibration plot according to the following equation:

i_p (µA) = 0.0097 C (nM) – 0.4013 (r = 0.997, n = 7)

In the equation, i_p represents the oxidation peak current, C the Vinorelbine concentration, r the correlation coefficient and n the number of experiments, respectively.

Limit of detection (LOD) and quantification (LOQ) values obtained with the aid of analytical curves were calculated according to the 3 s/m and 10 s/m, respectively. In this equation, s is the standard deviation of the peak currents (three runs) of the lowest concentration of the relevant linearity range (2.3×10^{-8} M) and m *is* the slope of the used calibration curves. The values were calculated as 7.5×10^{-9} M (as base form, 5.8 ng mL^{-1}) and 2.5×10^{-8} M (as base form, 9.47 ng mL^{-1}) for LOD and LOQ, respectively.

As can be seen from the values found, PG allowed the detection of very low concentrations of Vinorelbine without applying any chemical modification to the electrode (except for a simple electrochemical pretreatment). Electrochemical pretreatment used in this work is very fast, simple and cost-effective compared to other surface modification strategies and is environmentally friendly as it does not require any toxic chemicals. According to the opinion of some researchers, the increased electrochemical response obtained on the PG electrode compared to other electrode materials is due to the clay material in its structure **[23]**. Since this material provides a porous structure and a special surface area for the PG electrode, it increases the electrocatalytic efficiency of the electrode in the redox reactions of many analytes.

The analytical performance of the voltammetric method (in terms of sensitivity) developed by our working group for the first time is comparable to some of the separation methods using MS or MS/MS detection system **[6,7]**.

In order to evaluate the precision of the here-reported voltammetric method developed for Vinorelbine, solutions at a concentration of 3.5×10^{-7} M were prepared under the selected experimental conditions and stripping voltammograms of these solutions were recorded nine times in the same day. Oxidation peak current and potential values were measured from these voltammograms and the values found were evaluated as intra-day repeatability. According to the results, the RSD values were calculated as 1.23% (for peak current) and 0.32% (for peak potential).

3.3.1. Analysis of real samples

To verify the performance characteristics of the developed method in real samples, its applicability was first tested in commercially pharmaceutical formulation (injectable solution). The vial solutions were easily prepared after a simple dilution described in Section 2.4. By comparing the voltammograms of the vial content with the voltammograms of the standard Vinorelbine, it was observed that the both curves were compatible. Considering the required dilutions of the vial sample, Vinorelbine content was calculated as 51.50 mg (71.33 mg as ditartrate salt) per vial (RSD of 2.97%). This value is in good agreement with the label value of 50 mg per vial declared by the producer (recovery, 103.0%). In order to evaluate the validity of the proposed method, recovery experiments were applied by adding known volumes of standard Vinorelbine solutions to the previously analyzed sample solution between the linearity range. It was obtained the satisfactory recovery from 93.0 to 107.0%. It presents that there is no remarkable interference in the commercial pharmaceutical injectable forms.

Due to the high sensitivity and reproducibility of the voltammetric method developed on a disposable PG electrode were also investigated for the determination of Vinorelbine in spiked human urine sample without any complex separation. The only treatment was a simple dilution (1:200 v/v) with the selected supporting electrolyte. At the beginning of the experiments,

voltammograms of blank urine samples were prepared in supporting electrolyte (BR buffer, pH 10.0) in the absence and presence of TBAB. No oxidation steps were observed for biomolecules (uric acid, ascorbic acid, dopamine) in the potential range where the Vinorelbine signal is observed in surfactant-free solutions. In a previous study reported by our working group using SW-AdSV technique on PG electrode [40], the uric acid peak in the urine sample diluted with BR buffer (pH 10.0) appeared at approximately +0.30 V. The oxidation steps of ascorbic acid and dopamine on the PG electrode generally occur at lower positive potential values compared to uric acid [41,42]. On the other hand, when the same experiments were repeated in TBAB-containing solutions, a peak with a low intensity was observed +0.6 and +0.8 V. It can be assumed that this peak may be related to a different urine component, which is in anionic form at the pH studied and thus interacts with the cationic surfactant. Since standard addition method will be used for this purpose, it is clear that this peak will not affect the results. Considering the high peak intensity and smooth peak morphology of Vinorelbine in surfactant-free solutions at this pH, in order to avoid any risk, the studies in urine samples were performed in BR buffer pH 10.0 without surfactant. Analysis of model human urine sample (containing spiked concentration of 2.0×10^{-7} M for Vinorelbine in the electrochemical cell) is illustrated in Fig. 7A with the graphical evaluation of multiple standard addition method. The oxidation signal at about +0.70 V increased proportionally after five consecutive additions of the standard Vinorelbine solutions (Fig. 7B), yielding a linear calibration plot; i_p (μA) = 8.8263 C (μM) + 1.9281 (r = 0.987).

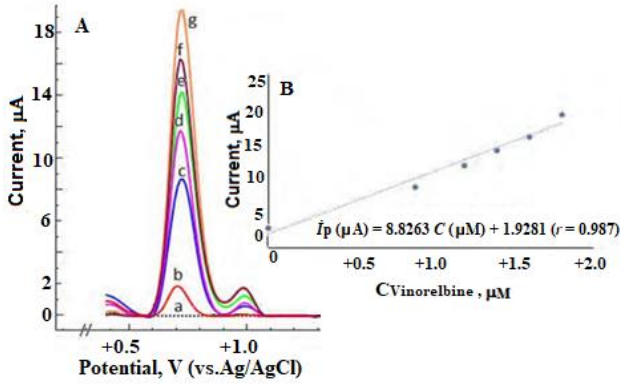

Figure 7. **(A)** SW stripping voltammograms recorded in the model urine sample from volunteer (diluted with BR buffer, pH 10 in the ratio of 1:200, v/v). Dashed lines (a) present the voltammogram of unspiked sample of urine; (b) in the presence of 2×10^{-7} M Vinorelbine; (c–g) after standard additions of 45, 60, 70, 80 and 90 μL from 2×10^{-4} M Vinorelbine). **(B)** The result of analysis by the standard addition method. The other operating conditions are as shown in Fig. 5.

As shown in Table 1, the quantification of Vinorelbine presented satisfactory RSD value and recovery indicating that the proposed method could also accurately determine Vinorelbine from urine samples.

Table 1. Analysis of model urine sample for Vinorelbine by SW-AdSV developed in this study using PG electrode.

Added (μM)	Found[a] (μM)	Recovery[b](%)± % RSD (%)
0	Not detected	
0.2	0.218	109.0± 4.58

[a]Calculated by using standard addition method. Values reported are mean of three different independent analyzes of the same sample. [b]Calculated as: (found concentration/added concentration) × 100.

4. CONCLUSION

As stated in the Introduction Section, there is very limited number of studies for the voltammetric determination of *Vinca* alkaloids. To our knowledge, only one electrochemically based research, which is quite old, has been reported for Vinorelbine. In the related study, no study was conducted for the determination of this compound, only the electrode mechanism was tried to be clarified on GC surface. In our present work, it was first shown how the Vinorelbine molecule is oxidized on PG electrode in aqueous or aqueous-surfactant (anionic/cationic) solutions. Then, voltammetric method was developed for the determination of real samples.

The observation obtained from the findings can be important in two respects: (*i*) Considering that the redox mechanism of Vinorelbine and similar compounds is very complex (especially in terms of forming free radicals and intermediate), the information obtained from this work may shed a great deal of light on the oxidation studies of *Vinca* alkaloids in the surfactant environment. (*ii*) The voltammetric method developed in this study will provide an alternative to chromatographic methods, which are often used for their determination.

It can be assumed that the proposed voltammetric method using a disposable, economical and environment-friendly PG electrode may also constitute the first step for on-site measurements of not only Vinorelbine but also other *Vinca* alkaloids, especially in wastewater around the hospital. The LOD value reached in the presence of surfactant looks very promising for future research.

REFERENCES

[1] G. M. Cragg, and D. J. Newman, "Plants as a source of anti-cancer agents," Journal of Ethnopharmacology, vol. 100, no. 1-2, pp. 72-79, Aug. 22, 2005. Doi: 10.1016/j.jep.2005.05.011.

[2] T. R. Asmis et al., "Age and comorbidity as independent prognostic factors in the treatment of non-small-cell lung cancer: A review of National Cancer Institute of Canada Clinical Trials Group Trials," Journal of Clinical Oncology, vol. 26, no. 1, pp. 54-59, Jan. 2008. Doi: 10.1200/JCO.2007.12.8322.

[3] Y. C. Xu, et al., "A systematic review of vinorelbine for the treatment of breast cancer," Breast Journal, vol. 19, no. 2. pp. 180-188, March 2013. Doi: 10.1111/tbj.12071.

[4] S. Ragot, et al., "Sensitive determination of vinorelbine and its metabolites in human serum using liquid chromatography-electrospray mass spectrometry," Journal of Chromatography B: Biomedical Sciences and Applications, vol. 753, no. 2, pp. 167-178, Apr. 2001. Doi: 10.1016/S0378-4347(00)00408-4.

[5] J. de Graeve, et al., "Metabolism pathway of vinorelbine (Navelbine®) in human: Characterisation of the metabolites by HPLC-MS/MS," Journal of Pharmaceutical and Biomedical Analysis, vol. 47, no. 1, pp. 47-58, May 2008. Doi: 10.1016/j.jpba.2007.12.006.

[6] S. Gao, et al., "Rapid and sensitive liquid chromatography coupled with electrospray ionization tandem mass spectrometry method for the analysis of paclitaxel, docetaxel, vinblastine, and vinorelbine in human plasma," Therapeutic Drug Monitoring, vol. 36, no.3, pp. 394-400., June 2014. Doi: 10.1097/FTD.0000000000000010.

[7] X. Gong et al., "Validated UHPLC–MS/MS assay for quantitative determination of etoposide, gemcitabine, vinorelbine and their metabolites in patients with lung cancer," Biomedical Chromatography, vol. 31, no. 11, e3989, Apr. 2017. Doi: 10.1002/bmc.3989.

[8] G. Corona, et al., "Rapid LC–MS/MS method for quantification of vinorelbine and 4-O-deacetylvinorelbine in human whole blood suitable to monitoring oral metronomic anticancer therapy," Biomedical Chromatography, vol. 32, no. 9, e4282, Sep. 2018. Doi: 10.1002/bmc.4282.

[9] J. F. Rusling, B. J. Scheer, and I. U. Haque, "Voltammetric oxidation of vinblastine and related compounds," Analytica Chimica Acta, vol. 158, pp. 23-32, 1984. Doi: 10.1016/S0003-2670(00)84810-2.

[10] A. Temizer, "Electroanalytical determination of vinca alkaloids used in cancer chemotherapy," Talanta, vol. 33, no. 10, pp. 791-794, Oct. 1986. Doi: 10.1016/0039-9140(86)80195-3.

[11] A. M. O. Brett, M. M. M. Grazina, T. R. A. Macedo, and D. Raimundo, "Anodic behavior of some Vinca alkaloids with cytostatic activity: Effect of pH," Electroanalysis, vol. 6, no. 1, pp. 57-61, Jan. 1994. Doi: 10.1002/elan.1140060111.

[12] I. Tabakovic, E. Gunic, and I. Juranic, "Anodic fragmentation of catharanthine and coupling with vindoline. Formation of anhydrovinblastine," vol. 62, no. 4, 947-953, Feb. 1997. Doi: 10.1021/jo9621128.

[13] A. M. Beltagi, "Development and validation of an adsorptive stripping voltammetric method for the quantification of vincamine in its formulations and human serum using a nujol-based carbon paste electrode," Chemical and Pharmaceutical Bulletin, vol. 56, no. 12, pp. 1651-1657, 2008. Doi: 10.1248/cpb.56.1651.

[14] Y. Zhang, J. Zheng, and M. Guo, "Preparation of molecularly imprinted electrochemical sensor for detection of vincristine based on reduced graphene oxide/gold nanoparticle composite film," Chinese Journal of Chemistry, vol. 34, no. 12, pp. 1268-1276, Dec. 2016. Doi: 10.1002/cjoc.201600582.

[15] E. Haghshenas, T. Madrakian, A. Afkhami, and H. Saify Nabiabad, "A label-free electrochemical biosensor based on tubulin immobilized on gold nanoparticle/glassy carbon electrode for the determination of vinblastine," Analytical and Bioanalytical Chemistry, vol. 409, no. 22, pp. 5269-5278, Sep. 2017. Doi: 10.1007/s00216-017-0471-y.

[16] P. Kovacic, "Unifying mechanism for anticancer agents involving electron transfer and oxidative stress: Clinical implications," Medical Hypotheses, vol. 69, no. 3, pp. 510-516, 2007. Doi: 10.1016/j.mehy.2006.08.046.

[17] I. U. Haque, and H. Saba, "Voltammetry of an anti-cancer drug," ECS Transactions, vol. 16, no. 18, pp. 3-23, Mar. 2009. Doi: 10.1149/1.3099679.

[18] H. R. S. Lima, et al., "Electrochemical sensors and biosensors for the analysis of antineoplastic drugs," Biosensors and Bioelectronics, vol. 108, pp. 27-37, June 2018. Doi: 10.1016/j.bios.2018.02.034.

[19] A. M. Oliveira Brett, et al., "A study of the electrochemical oxidation of Navelbine," Journal of the Pharmaceutical and Biomedical Analysis, vol. 11, no. 3, 203-206, March 1993. Doi: 10.1016/0731-7085(93)80197-9.

[20] A. M. Bond, P. J. Mahon, J. Schiewe, and V. Vicente-Beckett, "An inexpensive and renewable pencil: Electrode for use in field-based stripping voltammetry," Analytica Chimica Acta, vol. 345, no. 1-3, pp. 67-74, June 1997. Doi: 10.1016/S0003-2670(97)00102-5.

[21] J. Wang, A.-N. Kawde, and E. Sahlin, "Renewable pencil electrodes for highly sensitive stripping potentiometric measurements of DNA and RNA," vol. 125, pp.5-7, Jan. 2000. Doi: 10.1039/A907364G

[22] J. Wang, and A. N. Kawde, "Pencil-based renewable biosensor for label-free electrochemical detection of DNA hybridization," Analytica Chimica Acta, vol. 431, no. 2, pp. 219-224, March 2001. Doi: 10.1016/S0003-2670(00)01318-0.

[23] J. K. Kariuki, "An electrochemical and spectroscopic characterization of pencil graphite electrodes," Journal of The Electrochemical Society, vol. 159, no. 9, pp. H747–H751, Aug. 2012. Doi: 10.1149/2.007209jes.

[24] I. G. David, D. E. Popa, and M. Buleandra, "Pencil graphite electrodes: A versatile tool in electroanalysis," Journal of Analytical Methods in Chemistry, vol. 2017. 22 pages, Jan. 2017. Doi: 10.1155/2017/1905968.

[25] D. Demetriades, A. Economou, and A. Voulgaropoulos, "A study of pencil-lead bismuth-film electrodes for the determination of trace metals by anodic stripping voltammetry," Analytica Chimica Acta, vol. 519, no. 2, pp. 167-172, Aug. 2004. Doi: 10.1016/j.aca.2004.05.008.

[26] R. Vittal, H. Gomathi, and K. J. Kim, "Beneficial role of surfactants in electrochemistry and in the modification of electrodes," Advances in Colloid and Interface Science, vol. 119, no. 1, pp. 55-68, Jan. 2006. Doi: 10.1016/j.cis.2005.09.004.

[27] A. Levent, Y. Yardım, and Z. Şentürk, "Voltammetric behavior of nicotine at pencil graphite electrode and its enhancement determination in the presence of anionic surfactant," Electrochimica Acta, vol. 55, no. 1, pp. 190-195, Dec. 2009. Doi: 10.1016/j.electacta.2009.08.035.

[28] Y. Yardim, A. Levent, E. Keskin, and Z. Şentürk, "Voltammetric behavior of benzo[*a*]pyrene at boron-doped diamond electrode: A study of its determination by adsorptive transfer stripping voltammetry based on the enhancement effect of anionic surfactant, sodium dodecylsulfate," Talanta, vol. 85, no. 1, pp. 441-448, July 2011. Doi: 10.1016/j.talanta.2011.04.005.

[29] A. Levent, A. Altun, Y. Yardım, and Z. Şentürk, ''Sensitive voltammetric determination of testosterone in pharmaceuticals and human urine using a glassy carbon electrode in the presence of cationic surfactant,'' Electrochimica Acta, vol. 128, pp. 54-60. May, 2014. Doi: 10.1016/j.electacta.2013.10.024.

[30] A. Levent, Y. Yardım, and Z. Şentürk, ''Electrochemical performance of boron-doped diamond electrode in surfactant-containing media for ambroxol determination,'' Sensors and Actuators B: Chemical, vol. 203, pp. 517-526, Nov. 2014. Doi: 10.1016/j.snb.2014.07.035.

[31] P. Talay, Yardım and Z. Şentürk, ''Simple and sensitive electrochemical determination of higenamine in dietary supplements using a disposable pencil graphite electrode'' Monatshefte für Chemie - Chemical Monthly, vol. 151, pp. 301-307, 2020. Doi: 10.1007/s00706-020-02556-y.

[32] E. Laviron, ''General expression of the linear potential sweep voltammogram in the case of diffusionless electrochemical systems,'' Journal of Electroanalytical Chemistry, vol: 101, no. 1, pp. 19-28, July 1979. Doi:10.1016/S0022-0728(79)80075-3.

[33] E. Laviron, L. Roullier, and C. Degrand, "A multilayer model for the study of space distributed redox modified electrodes: Part II. Theory and application of linear potential sweep voltammetry for a simple reaction," Journal of Electroanalytical Chemistry and Interfacial Electrochemistry, vol. 112, no. 1, pp. 11-23, Feb. 1980. Doi: 10.1016/S0022-0728(80)80003-9.

[34] Vinorelbine https://go.drugbank.com/drugs/DB00361. Accessed 25 February 2023.

[35] H. Nakamura, A. Sano, and K. Matsuura, "Determination of critical micelle concentration of anionic surfactants by capillary electrophoresis using 2-naphthalenemethanol as a marker for micelle formation," Analytical Sciences, vol. 14, no. 2, pp. 379-382, Apr. 1998. Doi: 10.2116/analsci.14.379.

[36] P. Saxena, Y. Singh, and P. Jain, "Thermodynamic parameters of quaternary ammonium salts tmac,teab,tbab and tbai in aqueous and methanolic solutions at 298.16K,303.16K,308.16K and 313.16K by conductivity measurements," 2018. [Online]. Available: http://ijesc.org/

[37] I. Cherkaoui, V. Monticone, C. Vaution, and C. Treiner, "Surface modification of silica particles by a cationic surfactant: adsolubilization of steroids from aqueous solutions," International Journal of Pharmaceutics, vol. 176, no. 1, pp. 111-120, Dec. 1998. Doi: 10.1016/S0378-5173(98)00299-3.

[38] L. Kovacs and G.G. Warr, ''Changes in the adsorbed layer structure of cationic surfactants on mica induced by adsolubilized aromatic molecules,'' Langmuir, vol. 18, no. 12, pp. 4790-4794, 2002. Doi: 10.1021/la0118558.

[39] A. Adak, M. Bandyopadhyay, and A. Pal, "Adsolubilization of organic compounds in surfactant-modified alumina," Journal of Surface Science and Technology, vol. 21, no. 1-2, pp. 97-112, 2005.

[40] A. Levent, "Voltammetric behavior of acebutolol on pencil graphite electrode: highly sensitive determination in real samples by square-wave anodic stripping voltammetry," Journal of the Iranian Chemical Society, vol. 14, no. 12, pp. 2495-2502, Aug. 2017. Doi: 10.1007/s13738-017-1184-z.

[41] A. Özcan and Y. Şahin, "Preparation of selective and sensitive electrochemically treated pencil graphite electrodes for the determination of uric acid in urine and blood serum," Biosensors and Bioelectronics, vol. 25, no. 11, pp. 2497-2502, Jul. 2010. Doi: 10.1016/j.bios.2010.04.020.

[42] A. Levent and G. Önal, ''Application of a pencil graphite electrode for voltammetric simultaneous determination of ascorbic acid, norepinephrine, and uric acid in real samples,'' Turkish Journal of Chemistry, vol.42, no. 2, pp. 460-471, 2018. Doi: 10.3906/kim-1708-14.

BIOGRAPHIES

Günay Önal received her BSc (Dicle Univesty, Diyarbakır, Turkey), MSc(Dicle Universty, Diyarbakır, Turkey) and PhD (Yüzüncü Yıl University, Van, Turkey).) degrees in 1989, 1998 and 2018, respectively. Then, she joined Batman University (Batman, Turkey) in 2005. She became Asst Professor in 2012. Her research interest comprises the development new electrochemical sensors for the determination of compounds pharmaceutical, environmental, biological and clinical interest.

Abdulkadir Levent received his BSc, MSc and PhD degrees in 1998, 2001 and 2007, respectively, from Department of Chemistry, Faculty of Science, Yüzüncü Yıl University (Van, Turkey). Then, he joined Batman University (Batman, Turkey) in 2010. He became Associate Professor in 2012 and full professor in 2016 at the same university. His research interest comprises the development new electrochemical sensors for the determination of a wide range of organic compounds of pharmaceutical, environmental, biological and clinical interest, and spectrometric and chromatographic methods.

Zühre Şentürk received her PhD degree in 1985 from Department of Analytical Chemistry, Faculty of Pharmacy, Ankara University (Ankara, Turkey). She worked as visiting scientist in the laboratories of Prof. G.J. Patriarche and Prof. J.M. Kauffmann (ULB, Brussels, Belgium) in 1990 and

1996, respectively. She became full professor in 1997 in Faculty of Pharmacy, Gazi University (Ankara, Turkey). She attended Faculty of Science, Yüzüncü Yıl University (Van, Turkey) as a professor of Analytical Chemistry in 1999. Her research interest focuses on pharmaceutical, environmental and biomedical applications of electrochemical sensors (potentiometric ion-selective electrodes, modified electrodes, nanomaterials).

European Journal of Technique

journal homepage: https://dergipark.org.tr/en/pub/ejt

Vol.13, No.1, 2023

Determination of Antioxidant Activity of Dietary Selenium, Oleuropein, Glutathione Mixture

Feryal Zeliha Akay[1*], **Göksel Kızıl**[2]

[1*] University of Dicle, Faculty of Science, Chemistry Department, Diyarbakır, Turkey. (e-mail: feryalakay@hotmail.com.tr).
[2] University of Dicle, Faculty of Science, Chemistry Department, Diyarbakır, Turkey. (e-mail: gokselk@dicle.edu.tr).

ARTICLE INFO

Received: May., 26. 2023
Revised: Jun., 04. 2023
Accepted: Jun, 30. 2023

Keywords:
Free radicals
Selenium
Oleuropein
Gluthatione
ROS(reactive oxygen species)

Corresponding author: *Feryal Zeliha Akay*

ISSN: *2536-5010* | e-ISSN: *2536-5134*

DOI: https://doi.org/10.36222/ejt.1303042

ABSTRACT

Free radicals are a unit involved with cellular disorders through their damaging actions on proteins, lipids and DNA and area unit causative factors for an outsized variety of chronic diseases and therefore the aging method. Antioxidants of plant origin hold nice significance and have so gained utmost importance within the recent past. The current research spills the inhibition effect of selenium, glutathione and oleuropein mixtures against free radicals and supermolecule chemical action. It was determined that the mixture of oleuropein, glutathione and selenium used in the study inhibited free radicals. It was determined that it competed with the positive control at increasing concentrations. The mixture is intended to be used as a daily support supplement.
The aim of the study is to use the prepared mixture as an alternative to drugs known to have artificial antioxidant properties in the market. One of the aims of this study is to have both drug therapy in the literature and inhibition of ROS-induced damage in the biological system at an early stage.

1. INTRODUCTION

Phenolic compounds, which are the most effective phytochemical bioactive, and flavonoids and stilbenes, which are a group of phenolics, are important minor components of many fruits, vegetables and herbal products. The flavonoids, which form a large group of phenolic compounds, are divided into nine parts: flavones, isoflavones, flavonols, flavanols, flavanones, anthocyanidins, anthocyanins, flavonols and chalcones. Flavonoid antioxidant compounds are bioactive compounds with phenol chemical structure and contain polar hydroxyl (OH^-) substituents in their structures[1]. Phenolic substances are radical scavenging natural antioxidants. It is known that flavonoids inhibit lipid peroxidation and are radical scavenging [2].

The antioxidant effects of phenols have been explained by three mechanisms [3].
In the first mechanism (HAT), polyphenols (ArOH) free radical ($R^{\cdot}$); neutralizes it by giving hydrogen.

In the second mechanism (SET) (ArOH) free radical ($R^{\cdot}$); It forms the more harmless $ArOH^+$ radical by donating electrons.
Transition metals involved in free radical formation in the third mechanism (TMC); It forms stable compounds by being chelated with polyphenols. The formation of the $^{\cdot}OH$ radical, which is formed as a result of the Fenton reaction between H_2O_2 and the metal ion, is prevented(Figure 1.)

1.1. ROS (Reactive Oxygen Species)

They are forms of oxygen with high chemical reactivity compared to the normal oxygen molecule due to their chemical structure. Reactive oxygen species are thought to be an important factor in aging and most of the diseases are related to aging[4](Figure 2.).

1.2. Selenium

(Se) is an essential micronutrient in our diet and can reduce diabetic symptoms [5]. Se; It acts like insulin in streptozotocin (STZ)-induced diabetic mice, where it can regulate the activity of several enzymes involved in gluconeogenesis and glycolysis and facilitate the transport of glucose into cells[6]. However, high Se blood levels can cause toxicity.

Selenium affects oxidative stress, inflammation, apoptosis, uncontrolled cell proliferation, hormone production, angiogenesis and immune function, and DNA methylation. Selenium has insulin-like effects both in vitro and in vivo. Selenium ameliorates the treatment of models involving heart, kidney and platelet defects and alleviates disease symptoms in the diabetes animal [7].

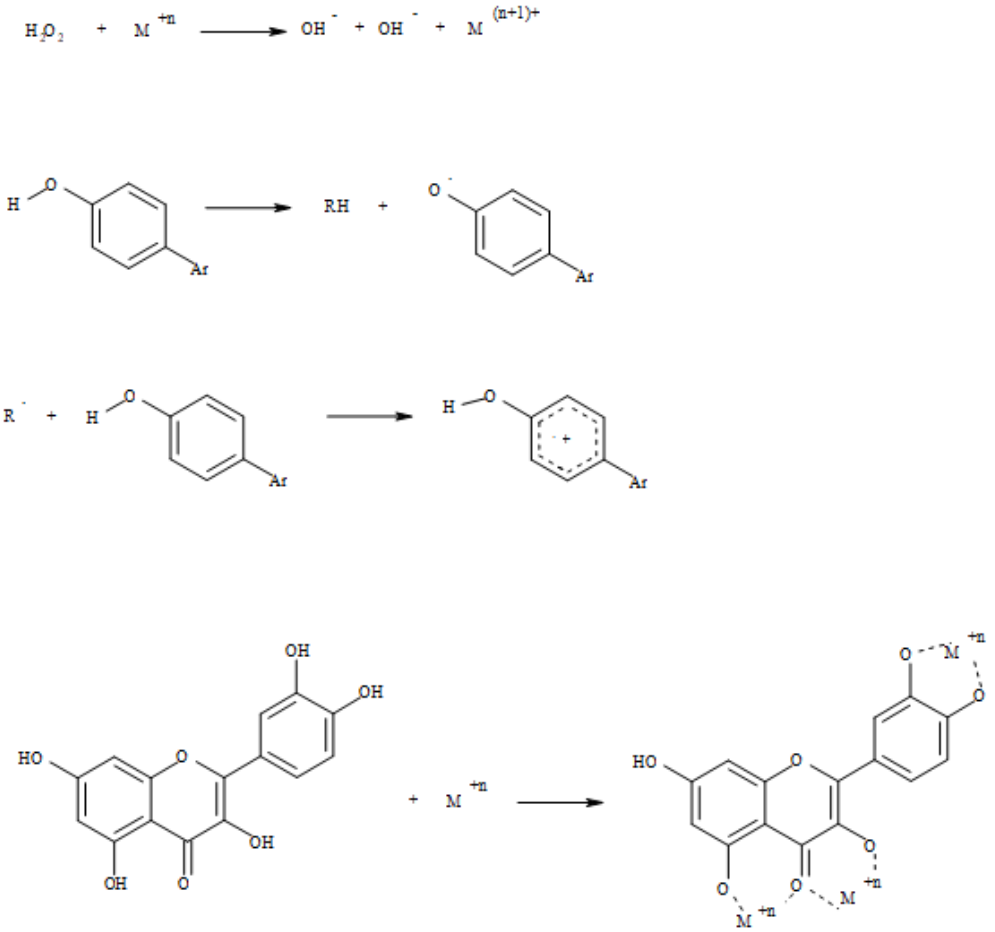

Figure 1. Antioxidant mechanism of polyphenols

1.3. Glutathione

Free radicals formed during glycation; They damage the decline of antioxidant defense mechanisms, cell organelles and enzymes. Thus, oxidative-chronic stress causes the formation and development of diseases that reduce the quality/duration of life such as diabetes, atherosclerosis, Alzheimer's and cancer.

Glutathione extinguishes oxidation agents[8]. Oxidation agents play a role in the formation, development and acceleration of aging in many diseases. It preserves hemoglobin. S-H groups have reducing properties against oxidizing agents and prevent oxidation of hemoglobin. Glutathione; It is depleted as a result of excessive consumption of drugs, chemicals, and pesticides. It is irreversibly damaged. (Figure 3).

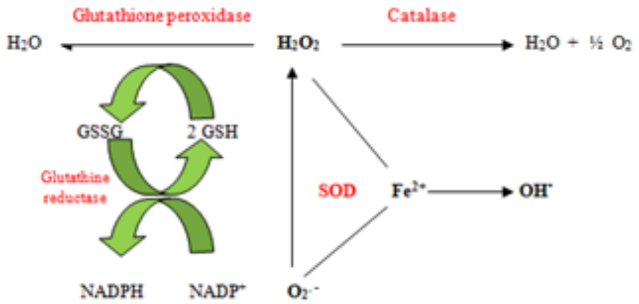

Figure 2. Free Oxygen Detoxification System

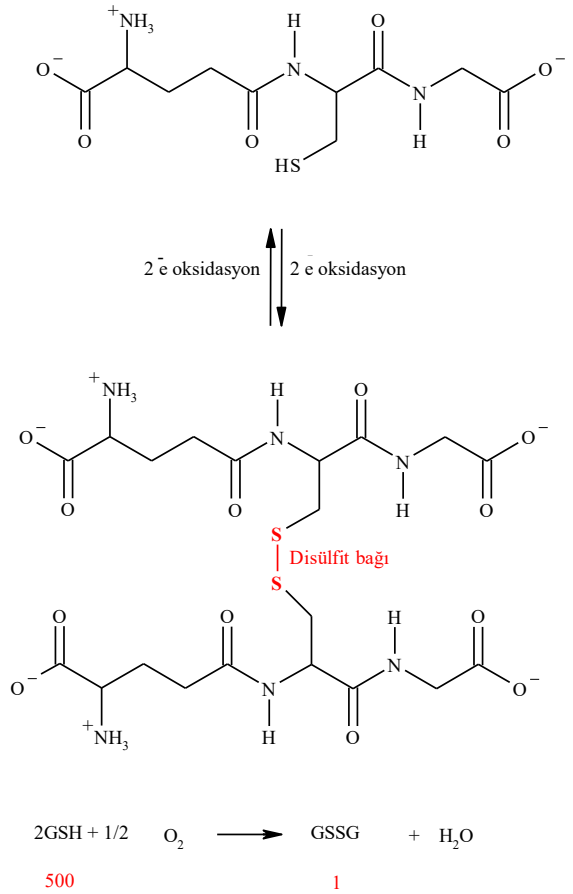

Figure 3. Oxidation and Reduction of Glutathione

1.4. Oleuropein

It is obtained from olive leaves and olive oil. (Figure 4.). Various studies have shown that oleuropein contains a high antioxidant activity[9].

Oleuropein inhibits low-density lipoproteins[10]. It scavenges free radicals formed in in vitro oxidation and in vivo lipid peroxidation. Oleuropein has a protective neuroprotective effect on spinal cord injury and oxidative spinal cord [11].

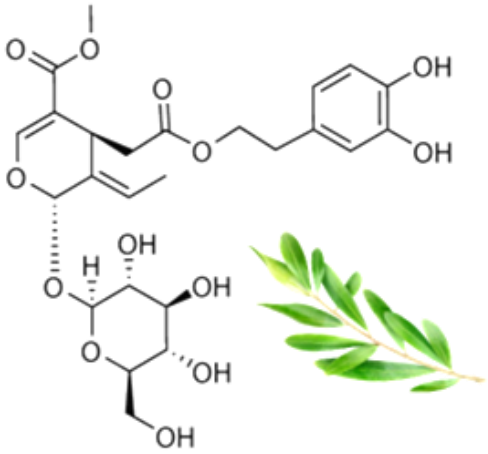

Figure 4. Oleuropein Chemical Structure

In the study, a mixture of oleuropein, selenium and glutathione substances with antioxidant properties known to inhibit reactive oxygen species (ROS) was prepared. The mixture was calculated according to the daily requirement of the body. The effect of the mix on scavenging DPPH and OH-radical was investigated.

2. MATERIALS AND METHODS

2.1. Chemicals Used

Selenium, L-glutathione, oleuropein were bought from Sigma-Aldrich. Gallic acid, ethanol, 1,1-diphenyl-2-picryl-hydrazil(DPPH), butylated hydroxytolue(BHT), butylated hydroxyanisole(BHA), α-tocopherol, quercetin, folin&ciocalteu's phenol reagent, ascorbic acid sodium carbonate, iron-2-chloride, iron-3-chloride, ethylenediaminetetraacetic acid (EDTA), hydrogen peroxide, ferrozine, ferricyanide, trichloroacetic acid(TCA), KH_2PO_4, K_2HPO_4 deoxyribose, 2-thiobarbituric acid(TBA), sodium hydroxide.

2.2. Selenium, oleuropein and glutathione mixture used

Selenium, oleuropein and glutathione were calculated according to the daily need of the body (Selenium 10 µg/kg, L- glutathione 15 µg/kg, Oleuropein 7mg/kg). A mixture of these substances was prepared. This mixture was used in all experimental studies.

2.3. Biochemical analysis

2.3.1. DPPH Radical Scavenging Activity

Antioxidants donate their hydrogen to the radical in order to scavenge the DPPH radical. The DPPH radical is free and stable. They become stable by gaining electrons or hydrogen. DPPH radical scavenging activity is more widely used as it provides the opportunity to compare the antioxidant activity in a short time compared to other methods[12]. The basic principle of this method is based on the reduction of absorbance.

Unpaired electrons on DPPH give maximum absorbance at 517 nm in the visible region. The reaction between the antioxidant molecule and DPPH causes a decrease in the concentration of DPPH in the environment, thus reducing the absorbance. The resulting structure is non-radical DPPH-H.

During the reaction, the color of the mixture changes from purple to yellow.

1 mg/ml stock solutions of oleuropein, gluthatione and selenium mix used in the study were prepared. Dilutions were made from stock solutions at concentrations of 10-100 µg/ml. A solution of 0.1 mM DPPH in 96% ethanol was prepared. 3 ml of mix extract was taken and 1 ml of 0.1 mM DPPH solution was added to them. After mixing the tubes thoroughly by vortexing, they were incubated for 30 minutes at room temperature in the dark. Then, absorbance values were measured in a UV device at 517 nm. BHA and were used as positive control. The negative control is the mix or the test sample without the positive control. The % inhibition values were calculated using the formula below.

$$\% I = [(A_{Control} - Sample) / A_{Control}] \times 100 \qquad (1)$$

2.3.2. OH Radical Scavenging Activity(Deoxyribose Assay)

The hydroxy radical scavenging activity of the mix used in the study was investigated in the Fe^{2+}/ascorbate/EDTA/H_2O_2 system by the deoxyribose method. Malondialdehyde (MDA) is formed after the hydroxy radical attacks deoxyribose. The resulting MDA reacts with TBA (2-thiobarbituric acid) to form a pink colored MDA-TBA complex[13].

Respectively; 100µl 1mM EDTA, 10 µl 0.1 mM $FeCl_3$, 100µl 50 mM H_2O_2, 360 µl 2.8 mM deoxyribose, 1 mg/ml stock solutions of oleuropein, glutathione and selenium mix(10-100µg/ml), 330 µl 50 mM pH 7.4 phosphate buffer and 100 µl of 0.3 mM ascorbic acid was used. The mixture was incubated for 1 hour in the dark and in a water bath at 37 ^oC. After incubation, 1 ml was taken from the mixtures, respectively; 1 ml of 10% TCA and 1 ml of 0.5% TBA (containing 0.025% BHA in 0.025M NaOH) were added. It was boiled in a 100 ^oC water bath until the pinkish color turned yellow (approximately 5 minutes). As soon as the color transformation was observed, it was cooled on ice. The absorbance value was measured in UV spectroscopy at 532 nm[14-15].

There is no mix in the negative control and no positive control. The % inhibition values were calculated using the formula below.

$$\% I = [(A_{Control} - Sample) / A_{Control}] \times 100 \qquad (2)$$

2.4. Statistical analysis

Data are presented as mean±SD. Statistical significance of the data was determined by Student's test, and a value of $p < 0.05$ was considered as statistically significant.

3. EXPERIMENTAL RESULTS AND DISCUSSION

3.1. Biochemical analysis

3.1.1. DPPH Radical Scavenging Activity

Antioxidant substances scavenge the DPPH radical by giving their own hydrogen to the radical. DPPH is a free and stable radical. The effect of scavenging DPPH radical is determined in a short time compared to other antioxidant methods.

Therefore it is used more widely. While determining the DPPH radical scavenging activity 5 concentrations of mix was studied in the range of 10-100 µg/ml.

% Inhibitions [($A_{Control}$ – Sample) / $A_{Control}$] x 100 was calculated with this formula

Mix showed scavenging activity between 28.08% and 91.41%.

BHA showed scavenging activity between 93.50% and 96.30% (Figure 5.).

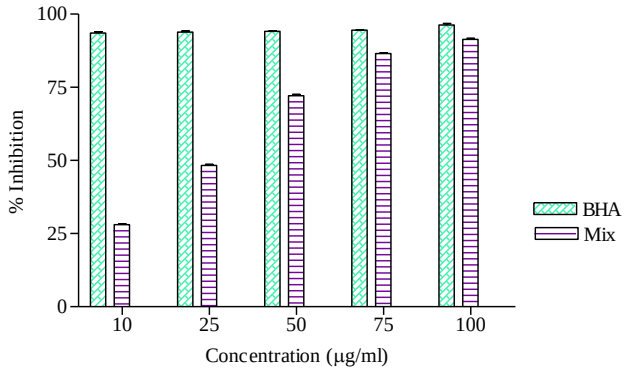

Figure 5. Scavenging effect of different concentrations(10, 25, 50, 75, 100 µg/ml) of *mix* on the DPPH radical. Each value is given as the average of 3 test results and ± standard deviations (SD) (n=3)

3.1.2. OH Radical Scavenging Activity(Deoxyribose Assay)

The OH radical scavenging activity of the mix was studied at 5 concentrations in the range of 10-100µg/ml.

% Inhibitions [($A_{Control}$ – Sample) / $A_{Control}$] x 100 was calculated with this formula

BHA was used as positive control. Mix showed hydroxy radical scavenging activity in the range of 39.68% and 99.67%. BHA showed hydroxy radical scavenging activity in the range of 38.21% and 97.39%(Figure 6.).

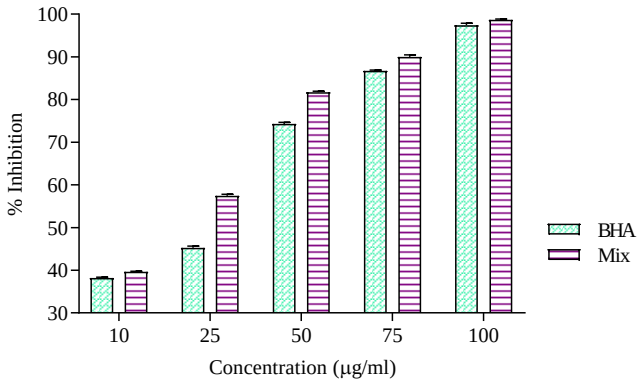

Figure 6. The hydroxy radical scavenging activity (%) of mix of different concentrations (10, 25, 50, 75, 100 µg/ml) Each value is averaged over 3 test results and given ± standard deviations (SD) (n=3)

4. CONCLUSION.

Antioxidant defense elements produced by the body can be damaged due to unnecessary drug use, chemical exposure and bad eating habits. In order for our body's defense elements to work, we need an antioxidant system. As a support element for our damaged antioxidant system, we need to take antioxidant supplements from the diet. It was determined that the mixture of oleuropein, glutathione and selenium used in the study inhibited free radicals. It was determined that it competed with the positive control at increasing concentrations. The mixture is intended to be used as a daily support supplement.

The prepared mixture was used as a protective agent in immunoglobulin G protein and lymphocyte damage in the follow-up study. Quite efficient results have been obtained.

ACKNOWLEDGEMENT

This study was carried out as a thesis in the YOK 100/2000 Priority Thematic Area Biomaterials and Tissue Engineering doctoral program. Dicle University Scientific Research Project Coordinatorship was supported by the Ph.D. project numbered Science-22.004.

AUTHOR CONTRIBUTIONS

Author A: Conceived and designed the analysis. Collected data and performed the analysis. Performed statistical analysis and wrote the paper.

Author B: She was the PhD thesis advisor and provided the execution of the project.

CONFLICTS OF INTEREST

The authors declare no conflict of interest.

REFERENCES

[1] Pietta PG. Flavonoids as antioxidants. Journal of natural products, 63(2000) 1035–1042. https://doi.org/10.1021/np9904509

[2] Tokusoglu, O. (2016). Effect of high hydrostatic pressure processing strategies on retention of antioxidant phenolic bioactives in foods and beverages–a review. Polish Journal of Food and Nutrition Sciences, 66(4).

[3] Leopoldini, M., Marino, T., Russo, N., & Toscano, M. (2004). Antioxidant properties of phenolic compounds: H-atom versus electron transfer mechanism. The Journal of Physical Chemistry A, 108(22), 4916-4922. 2

[4] Bonnefont-Rousselot D, Thérond P, Beaudeux JL, Peynet J, Legrand A, Delattre J. High density lipoproteins (HDL) and the oxidative hypothesis of atherosclerosis. Clin Chem Lab Med. 37(1999) 939-948 doi:10.1515/CCLM.1999.139

[5] Pillai, S. S., Sugathan, J. K., & Indira, M. (2012). Selenium downregulates RAGE and NFκB expression in diabetic rats. Biological trace element research, 149, 71-77.

[6] Hwang, J. Y., Zhang, J., Kang, M. J., Lee, S. K., Kim, H. A., Kim, J. J., & Kim, J. I. (2007). Hypoglycemic and hypolipidemic effects of Saururus chinensis Baill in streptozotocin-induced diabetic rats. Nutrition Research and Practice, 1(2), 100-104.

[7] Ayaz, M., Ozdemir, S., Ugur, M., Vassort, G., & Turan, B. (2004). Effects of selenium on altered mechanical and electrical cardiac activities of diabetic rat. Archives of Biochemistry and Biophysics, 426(1), 83-90.

[8] Liu, H., Wang, H., Shenvi, S., Hagen, T. M., & LIU, R. M. (2004). Glutathione metabolism during aging and in Alzheimer disease. Annals of the New York Academy of Sciences, 1019(1), 346-349

[9] Hassen, I., Casabianca, H., & Hosni, K. (2015). Biological activities of the natural antioxidant oleuropein: Exceeding the expectation–A mini-review. Journal of Functional Foods, 18, 926-940.

[10] Ahamad, J., Toufeeq, I., Khan, M. A., Ameen, M. S. M., Anwer, E. T., Uthirapathy, S., ... & Ahmad, J. (2019). Oleuropein: A natural antioxidant molecule in the treatment of metabolic syndrome. Phytotherapy Research, 33(12), 3112-3128.

[11] Khalatbary, A. R., & Ahmadvand, H. (2012). Neuroprotective effect of oleuropein following spinal cord injury in rats. Neurological research, 34(1), 44-51.

[12] Gülçin I, Küfrevioglu OI, Oktay M, Büyükokuroglu ME, Antioxidant, antimicrobial, antiulcer and analgesic activities of nettle (Urtica dioica L.). Journal of ethnopharmacology, 90(2004) 205–215. https://doi.org/10.1016/j.jep.2003.09.028

[13] Wang L, Yen JH, Liang HL and Wu MJ. "Antioxidant effect of methanol extracts from lotus plumule and blossom (Nelumbo nucifera

Gertn.)," Journal of Food and Drug Analysis 11 (2003) https://doi.org/10.38212/2224-6614.2726.

[14] Shimada K, Fujikawa K, Yahara K, Nakamura T, Antioxidative properties of xanthan on the autoxidation of soybean oil in cyclodextrin emulsion. Journal of agricultural and food chemistry, 40(1992) 945-948.

[15] Mazumder A, Gerlt JA, Absalon MJ., Stubbe J, Cunningham RP, Withka J, Bolton PH, Stereochemical studies of the. Beta.-elimination reactions at aldehydic abasic sites in DNA: endonuclease III from Escherichia Coli, sodium hydroxide, and Lys-Trp-Lys. Biochemistry, 30(1991) 1119-1126.

BIOGRAPHIES

Feryal Zeliha Akay obtained her BSc degree in Chemistry from Dicle University in 2015. She received the MSc. diploma in Biochemistry from the Dicle University in 2018 and make PhD in two programs; Biochemistry, Biomaterials and Tissue Engineering of the same university. She is active in teaching and research in the AGEs(Advanced glycation and product, biological macromolekules damage and cell culture system.

Göksel Kızıl, Prof. Dr. obtained her BSc degree in Chemistry from Dicle University in 1990. She received the PhD diploma in Biochemistry from the University of Nottingham in 1998 She is active in teaching and research in the immune system cells, vaccine and biological macromolekules damage and cell culture system

European Journal of Technique

journal homepage: https://dergipark.org.tr/en/pub/ejt

Vol.13, No.1, 2023

Q-Learning Based Obstacle Avoidance Data Harvesting Model Using UAV and UGV

Erdal AKIN[1,3*], **Yakup SAHIN**[2]

[1*]Bitlis Eren University, Computer Engineering Department, 13100, Merkez, Bitlis, Türkiye. (e-mail: e.akin@beu.edu.tr).
[2] Bitlis Eren University, Electrical and Electronics Engineering Department, 13100, Merkez, Bitlis, Türkiye. (e-mail:ysahin@beu.edu.tr).
[3] Malmö University, Department of Computer Science and Media Technology, Malmö, Sweden. (e-mail:erdal.akin@mau.se).

ARTICLE INFO

Received: Jan., 17. 2023
Revised: May., 22. 2023
Accepted: June., 26. 2023

Keywords:
Q-Learning, UAV, UGV, Data Harvesting, IoT

Corresponding author: *Erdal AKIN*

ISSN: *2536-5010* | e-ISSN: *2536-5134*

DOI: https://doi.org/10.36222/ejt.1237590

ABSTRACT

The Internet of Things (IoT) has revolutionized our lives by providing convenience in various aspects. However, for the IoT environment to function optimally, it is crucial to collect data from IoT devices regularly. This is because timely data collection enables more accurate evaluations and insights. Additionally, energy conservation is another crucial aspect to consider when collecting data, as it can significantly impact the sustainability of the IoT ecosystem. To achieve this, Unmanned Aerial Vehicles (UAVs) and Unmanned Ground Vehicles (UGVs) are increasingly being used to collect data. In this study, we delve into the problem of how UAVs and UGVs can effectively and efficiently collect data from IoT devices in an environment with obstacles. To address this challenge, we propose a Q-learning-based Obstacle Avoidance Data Harvesting (QOA-DH) method, which utilizes reinforcement learning principles to make data collection decisions. Additionally, we conduct a comparison of the performance of UAVs and UGVs, considering the different restrictions and assumptions that are unique to each type of vehicle. This research aims to improve the overall efficiency and effectiveness of data collection in IoT environments and pave the way for sustainable IoT solutions.

1. INTRODUCTION

Internet of Things (IoT) devices benefit us from many applications in diverse areas, such as health management, military monitoring, and environmental measurements. The IoT devices collect or generate some data based on the usage purpose. In order to evaluate the data, it should be harvested periodically. For this purpose, an autonomous vehicle can visit all IoT devices and collect the data. Unmanned aerial vehicles (UAV) and unmanned ground vehicles (UGV) are well-known autonomous vehicles for data harvesting. These vehicles generally use electric and similar components. However, they also differ in many aspects, such as maneuverability, speed, battery capacity, and cost. The energy in the vehicle's battery should be sufficient to perform the abovementioned operation. Accordingly, the vehicle should be chosen according to the environment, time, and cost of data harvesting. However, energy efficiency is a significant issue for data harvester autonomous vehicles. Therefore, the best trajectory planning is needed to ensure optimum energy efficiency. Accordingly, we propose a novel framework where an autonomous vehicle must cover a maximum number of IoT devices to maximize the harvested data. Then, we propose a Q-Learning Based Obstacle Avoidance Data Harvesting method, called QOA-DH, which provides trajectories for the autonomous device to maximize the number of visited IoT devices during their first attempt (no battery replenishment).

This paper compares two unmanned vehicles, UAV and UGV, with various features detailed in Section 3. Finally, we perform a comprehensive experiment to assess the performance of the trajectories provided by the QOA-DH concerning the different features of UAV and UGV.

The remainder of this paper is structured as follows. In Section 2, we provide the literature review for Q-learning-based trajectory designs. Section 3 describes Q-learning, while the proposed QOA-DH model and assumptions are presented in Section 4. In Section 5, simulation details and performance analyses are provided. Lastly, we conclude the paper in Section 6.

2. RELATED WORKS

Data harvesting from IoT devices by an autonomous vehicle is a fast, reliable, and economical approach. The UAV is a commonly used data harvester vehicle, and it is independent of the roads and can visit IoT devices more quickly from UGV. But, the battery capacity of the UAV is limited

compared to the UGV. To evaluate an effective data collection process, optimum trajectory planning is desired. Therefore, Artificial Intelligence (AI) based trajectory planning studies have been presented in the literature [1]. Swarm UAVs can harvest data simultaneously, but trajectory planning for swarms needs more effort, time, and processing power for trajectory planning [2, 3, 4].

On the other hand, 2D path planning needs less effort with the probabilistic roadmaps (PRM) algorithms [5, 6] from 3D path planning [7]. In some research, after the swarm UAVs collect the data, the data is immediately loaded into the cloud [8, 9, 10]. These swarm data harvesters use the global system for mobile communications (GSM) to load the data to the cloud. This process leads to a time difference between sensor data.

A UGV can visit more IoT devices than a UAV because of its large battery capacity. Although the UGV has a larger battery capacity, time and efficiency should be considered during data harvesting. Consequently, trajectory planning is quite essential for the UGV. The meta-heuristic search algorithms can help to determine the optimum trajectory. Particle swarm optimizer (PSO) is another approach to planning the right trajectory [11]. Ant colony optimization method presents remarkable results in optimal path planning [12]. Near-optimal algorithm [13] gives better results than A* in a static environment. Finally, local-search-based and edge-learning systems are used to determine the efficient trajectory [14, 15].

3. REINFORCEMENT LEARNING

Machine Learning (ML) can be categorized into three techniques; supervised learning, unsupervised learning, and reinforcement learning. Reinforcement Learning (RL) differs from other techniques in attempting a specific task in a previously unknown environment [16]. In RL, an agent takes actions based on a policy to achieve a goal in an unknown environment. To do that, the agent tries to learn a policy to maximize the value and reach the specific task. As seenin Figure 1, the agent moves from the state $s_t \in S$ by taking an action $a_t \in A$ concerning the reward $r_{t+1} \in R$ obtained from the previous experiences [17, 18, 19].

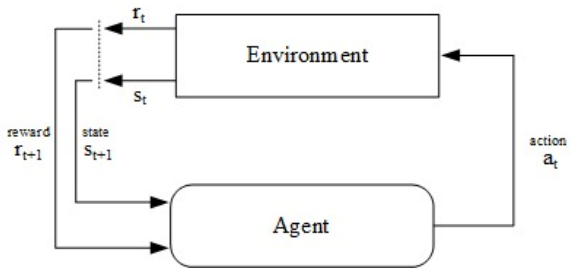

Figure 1. Reinforcement Learning Framework

There are several RL algorithms in the literature; one is the Q-learning algorithm. Q-Learning is used to find the optimal action-value function for an agent in an environment. The Q-Learning algorithm is based on the principle of learning from experience and updating the agent's knowledge based on the rewards it receives from the environment. One of the earliest works on Q-Learning was done in 1992 when they introduced the Q-Learning algorithm for learning the optimal action-value function for an agent in a finite Markov Decision Process (MDP) environment [20]. They showed that the Q-Learning algorithm converges to the optimal action-value function under certain conditions, such as the existence of a unique fixed point and the use of a sufficiently small learning rate. The actor-critic approach has been proposed to improve the Q-Learning algorithm in the following years [21]. State-Action-Reward-State-Action (SARSA) is similar to Q-Learning. Still, it uses the action selected by the agent in the next state, rather than the action with the maximum value, to update the action-value function. This makes SARSA more suitable for online learning and dealing with problems where the optimal action may not be known in advance [22]. The Q-Learning algorithms are used to solve many problems in the literature. For example, robotics are trained to avoid obstacles in unknown environments [23]. Another approach that the algorithm is used to train agents and play complex games such as Chess and Go [24]. Besides, Q-Learning is used in other applications, including finance, healthcare, IoT, and control systems [25, 26, 27, 28, 29].

Q-learning algorithm that uses a Q-table $Q(s,a)$, Where S is the set of states, and A represents the set of actions that the agent can take. In state $s \in S, Q(s,a)$ is updated with the equation (1) when the agent takes an action $a \in A$ [18, 19].

$$Q_{t+1}(s_t,a_t) = Q_t(s_t,a_t) + \alpha(r_t + \gamma max_a Q_t(s_{t+1},a_t) - Q_t(s_t,a_t)) \quad (1)$$

where the agent obtains the instant reward $r_t \in R$ while moving from state s_t to state s_{t+1}. The discount factor $\gamma \in (0,1]$ stabilizes the immediate and future reward. The Learning Rate $\alpha \in (0,1]$ is a hyperparameter correlating the new value with the previous value.

4. SYSTEM MODEL and PROBLEM STATEMENT

In this section, we first introduce the system model of the proposed Q-learning Based Obstacle Avoidance Data Harvesting (QOA-DH) Model for UAV and UGV.

4.1. System Model

We consider a network composed of a Base Station (BS), which is also a Terminal Station, and a grid world ($M(X,Y)$) where the UAV or UGV can start-finish its duty from BS. We consider UAV and UGV responsible for data harvesting from IoT devices, which are yellow circles in Fig. 2a. Our goal is to maximize the total number of visited IoT devices with minimum battery consumption and time interval. For this purpose, we use a grid-based map, as seen in Figure 2a, where the red cell represents BS, yellow circles are IoT devices, and black cells are obstacles (a.k.a. walls). Therefore, we formulate our QOA-DH Model as a tuple $< V,S,A,R,\gamma,\alpha >$ represents the type of the vehicle (agent) V, the set of states S, the set of actions spaces A, reward function $R(s,a)$, the future discount factor γ, and learning rate α, respectively. An agent (UAV or UGV) selects an action $a_t \in A$ in time t based on its state $s_t \in S$, which is the location of the agent in time t. The action set A includes up, down, left, and right in the current state of the agent. In each step, the agent consumes the battery as follows:

$$\text{for } a_t \in A, B_t(V) = B_t(V) - \eta(V) \quad (2)$$

where $B_t(V)$ is the remaining battery of the agent at time t and $\eta(V)$ represents battery consumption in each step a_t. The battery of the agent is 100 at the beginning. The battery consumption differentiates concerning the technology used for the vehicles. Since high-capacity batteries cause excessive load on UAVs, batteries with low capacity are used. Therefore, UAVs consume more battery than UGVs for the same number of actions.

When an agent takes action, it earns a reward (or punishment) based on the Reward function, an essential parameter for optimizing the algorithm. Since we have two different agents, we carefully present the reward function as follows:

$$R_{s,a}(V) = \begin{cases} I(V) * C, if\ s' \epsilon\ G\ \{obstacle\} \\ O(V) * C, \quad Otherwise \end{cases} \quad (3)$$

Where $s' \in S$ represents the next state of the agent, C denotes a constant factor, $I(V) \in [1,3]$ and $I(V) \in [-15,0]$ are functions that return a factor concerning the type V of the vehicle for instant reward.

Another two important parameters are the discount factor and learning rate. Discount factor $\gamma \in (0,1]$ balances immediate and future rewards to adjust the greedy of the policy. The learning rate $\alpha \in (0,1]$ is the fitness between the previous and new values [19, 30]. In section 5, we evaluated the algorithms with $\gamma = 0.5$ and $\alpha = 0.15$.

Algorithm 1: Environment setup of Q-learning Based Obstacle Avoidance Data Harvesting (*QOA-DH*) Model.

Initialization: Grid world $M(X,Y)$, Base Station (is also starting position) $BS(X,Y) \in M$, battery $B_t = 100$, Vehicle Type (V), Action set $A = \{up, down, left, right\}$, Reward Table R, Discount Factor γ, Learning Rate α, Initial Q-table $Q_t[s,a] = 0$, Episode Number $E = 1000000$, $\epsilon = 1.0$, and decay value $d = 0.000001$.

```
foreach E do
    Reset R.
    Reset Environment.
    while True do
        t++.
        Reduce battery of the V as in equation (2).
        Obtain reward as in equation (3).
        if random ≤ ε then
            select action a_t ∈ A, randomly .
        else
            Select action a_t = argmax_a(Q(s,a))
        end
        if B_t = 0 ∨ s = BS(X,Y) then
            break.
        end
        Update Q-table as in Equation 1.
        Update Reward Table R as in Equation 3.
    end
    ε = ε − d.
end
```

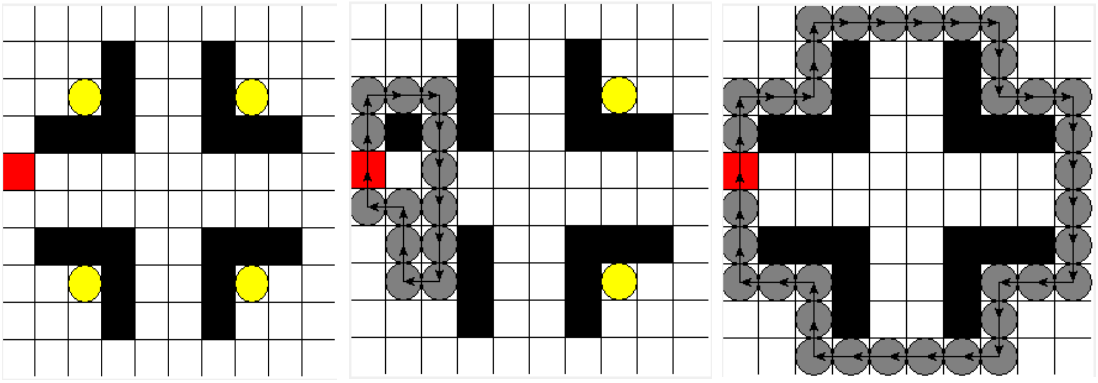

(a) Initial Small Map (b) UAV (c) UGV

Figure 2. Portraying the initial small map and final trajectories of the vehicles; (a) Initial small map, (b) UAV trajectory, and (c) UGV trajectory. Arrows show the direction of the vehicles, the red square is the base station, and the gray circles present observed areas.

4.2 Methodology

Our primary goal in this study is to visit a maximum number of IoT devices to maximize harvested data. However, there are restrictions and assumptions that Unmanned Vehicles (UAV and UGV) need to adhere to:

- UAV and UGV have limited battery capacity.
- Both UAV and UGV do not charge their battery and fulfill their task with only one battery.
- Battery consumption differs for UAV and UGV. It is calculated with Equation 2, and the parameters are given in Table 1.
- UAV flies at a certain altitude so that it can fly over obstacles. UGV should avoid the obstacles.

4.3 Problem Statement

This section presents our proposed QOA-DH Model setup in Algorithm 1.

The vehicle (agent) starts in the base station $BS(X,Y) \in M(X,Y)$. The algorithm initializes the Q-table $Q(S,A)$ with zero at the beginning and updates it in each step as in Equation 1. The reward table R is filled based on Equation 3. In each step, the vehicle's battery is reduced using Equation 2. A new episode starts over if the battery runs out or the agent reaches the terminal state (same as BS). In each episode, the obtained trajectory and the total reward are stored.

5. SYSTEM MODEL and PROBLEM STATEMENT

In this section, we compare the UAV and UGV on the QOA-DH method considering energy efficiency, number of observed IoT devices, and spent time to accomplish the task.

5.1 Simulation Setting

We developed the QOA-HA with Python 3.9 version using NumPy, Tkinter, gym, and collection libraries. As illustrated in Fig. 2a and Fig. 3a, we have a $10x10$ and a 20x20 grid environment. The red cell is BS, where the agent (UAV or UGV) starts and ends its duty. Black cells are obstacles in the environment.

Since the UAV can fly over the obstacles $O(V)$ parameter is given as 0, it is -15 for forcing the UGV to avoid the obstacles. The yellow circles are IoT devices the agent is responsible for collecting data. $I(V)$ is the parameter to provide a reward for directing the agent through these cells. We train each vehicle on the QOA-DH in 1000000 episodes (E). Battery consumption η(V) is chosen as 6 and 3 for UAV in small and big maps, respectively, while it is 2 and 1. The hyperparameter used in the simulation is summarized in Table I.

TABLE I

Primary hyperparameters for QOA-DH.

	SMALL MAP (10x10)		BIG MAP (20X20)	
Parameter	UAV	UGV	UAV	UGV
Grid G	10x10	10x10	20x20	20x20
Episode E	1000000	1000000	1000000	1000000
Epsilon ε	1.0	1.0	1.0	1.0
Decay Value d	0.000001	0.000001	0.000001	0.000001
Discount Rate γ	0.5	0.5	0.5	0.5
Learning Rate α	0.15	0.15	0.15	0.15
$B_t(V)$	100	100	100	100
$\eta(V)$	6	2	3	1
C	1000	1000	1000	1000
$I(V)$	3	1	3	1
$O(V)$	0	-15	0	-15

The snapshot of the computed trajectories of the UAV and UGV are represented in Fig. 2. Grey circles show the observed cells (trajectories), and arrows represent the direction of the UVs. As seen in Fig. 2b and 2c, the UAV flies over a small area of the environment, while the UGV visits all IoT devices. This is because the UAVs have different battery constraints and assumptions. Therefore, we compare UAV and UGV on

QOA-DH model by using the following performance metrics:

- The ratio of Observed IoT Devices (ROIoT) (%): This is the ratio of the number of observed IoT devices.
- Battery Consumption (BC) (%): This is the ratio of the battery consumption, which is calculated using Equation 2, of the agents.
- Spent Time (ST) (Time Unit): This is the time the agent spends completing its duty for only one battery capacity without replenishment.

5.2 Evaluation

We evaluate the performance of the vehicles with diverse battery consumption parameters in two different size maps. The small map has a 10x10 grid, and the big map has a 20x20 grid.

5.2.1 Small Map Evaluation

As seen in Fig. 2a, four IoT devices are located behind the walls in the 10x10 grid map. The UGV visits and collects data from all IoT devices (100%) in the environment, as seen in Fig. 3. Conversely, the UAV can only fly over half of the IoT devices, even if it can fly over obstacles. The reason behind this is that the UAV consumes more energy for its movement. Accordingly, when we evaluate the battery consumption of the vehicles in Fig. 4, the battery consumption is around 84% for the UAV and around 72% for the UGV.

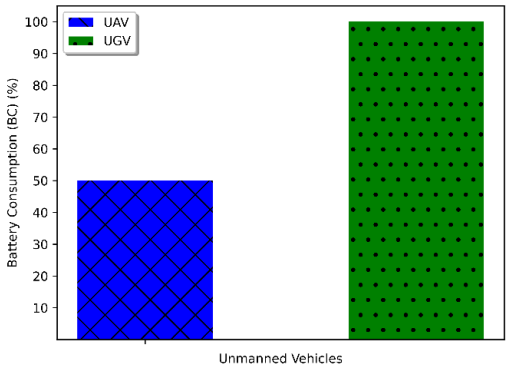

Figure 3. The ratio of Observed IoT Devices (ROIoT) (%) in Small Map.

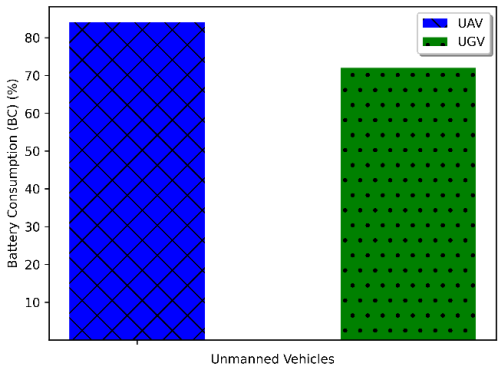

Figure 4. Battery Consumption (BC) (%) in Small Map.

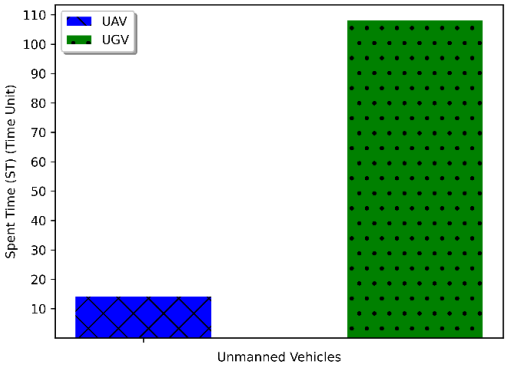

Figure 5. Spent Time (ST) (Time Unit) in Small Map.

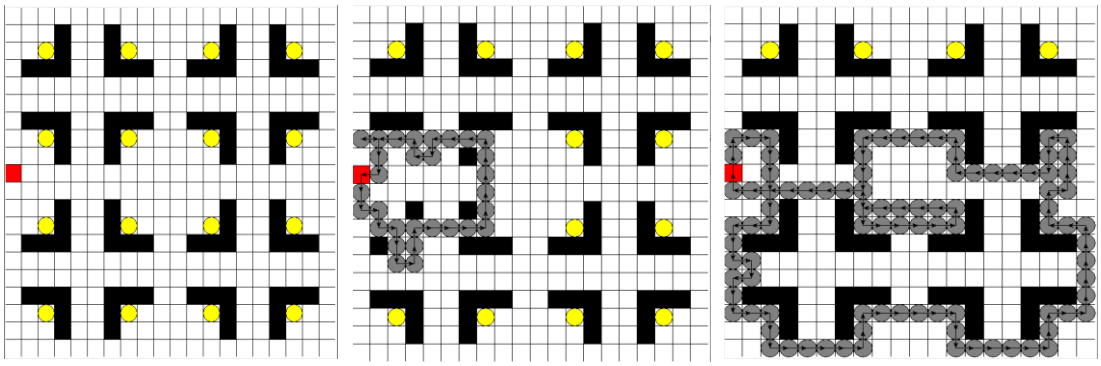

(a) Initial Big Map (b) UAV (c) UGV

Figure 6. Portraying the initial big map and final trajectories of the vehicles; (a) Initial big map, (b) UAV trajectory, and (c) UGV trajectory. Arrows show the direction of the vehicles, the red square is the base station, and the gray circles present observed areas.

Obviously, the UGV accomplishes its task with better battery efficiency than the UAV. The UAV should replenish its battery (more than one time) to complete the task.

On the other hand, time efficiency is another metric we should consider. In the scenario of needing fast data collection from IoT devices, the UGV would fail. This is because the UGV completes its duty in around 110 time units, while visiting two IoT devices takes around 15 time units for the UAV. This results in 10 times faster than the UGV. However, if we consider the battery recharging of the UAV, it would take more time than the UGV to achieve the task. Therefore, using multiple batteries or UAVs is not a cost-effective way.

5.2.2 Big Map Evaluation

In this section, we evaluated the performance of the devices in a 20x20 grid map. Assuming that battery usage is 1% of the remaining battery of the UGV and 3% for the UAV on the map. In this map (Fig. 6a), there are 16 IoT devices located behind the walls. The trajectories of UAV and UGV are given in Fig. 6b, Fig. 6c, respectively. Since the map is greater than the previous scenario, both vehicles could not visit all IoT devices. However, as seen in Fig. 7, UGV is able to visit 75% of the devices (12 IoT devices), while UAV can only visit 25% of them (4 IoT devices).

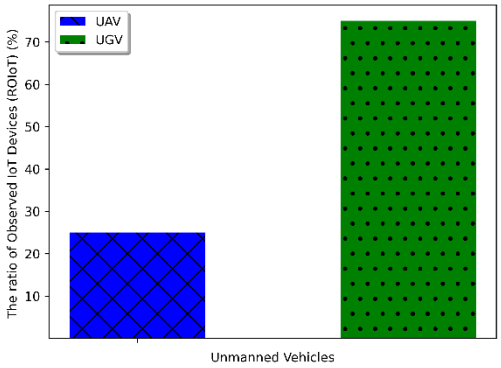

Figure 7. The ratio of Observed IoT Devices (ROIoT) (%) in Big Map.

Due to the large size of the map, both vehicles try to use almost all of their batteries to complete their task, Fig. 8. Since both need to return the base station (BS) before the battery is completely running out, the UAV completes its trajectory with 94% battery consumption. The remaining 6% battery would not be enough to detour to visit another IoT device. On the other hand, UGV uses all its battery to reach the BS.

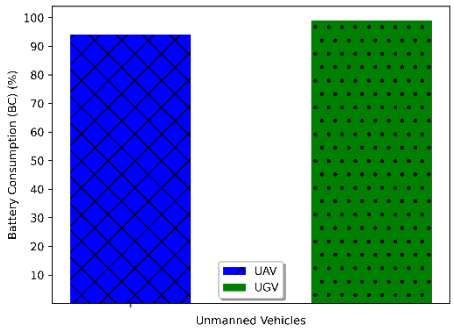

Figure 8. Battery Consumption (BC) (%) in Big Map.

Another important metric is the spent time (ST) to complete the task. As seen in Fig. 9, like the small map, the UAV completes its flight 10 times faster than the UGV with fewer visited IoT devices. Again, if fast data collection is crucial, this issue can be solved by using multiple UAVs. Otherwise, multiple batteries replenishing with one UAV would be time-consuming because the UAV needs to fly to the BS for battery replenishment and take off to visit remaining IoT devices.

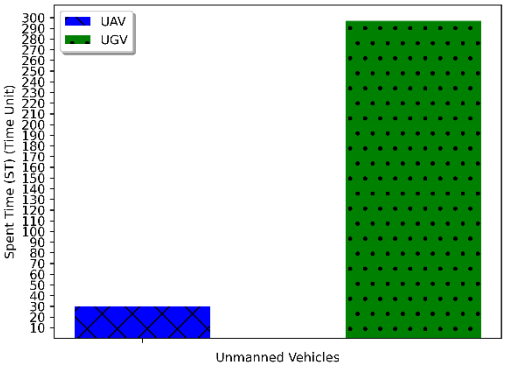

Figure 9. Spent Time (ST) (Time Unit) in Big Map.

6. CONCLUSION

In the event of data harvesting from IoT devices, Unmanned Vehicles (UVs) are widely used. Unmanned Aircraft Vehicles (UAVs) and Unmanned Ground Vehicles (UGVs) are well-known vehicles used for this purpose. Accordingly, in this study, we propose a Q-learning Obstacle Avoidance Data Harvesting (QOA-DH) framework, where we train the vehicles concerning their battery restriction and movement velocity. The results demonstrate that the UGV is more battery effective and can visit all IoT devices to harvest data in the environment. On the other hand, the UAV is faster than the UGV, giving it an advantage in achieving minor duties in a short time. However, since the UAV consumes battery faster, it should recharge its battery, which is not time efficient. To overcome this issue, we can use multiple batteries for replenishing or UAVs interchangeably, using each other to accomplish the task. For all that, both solutions are not cost-effective. Therefore, to overcome the issues and achieve the task for our future work, we plan to extend this work to propose a cost, energy, and time-efficient hybrid approach that uses UAV and UGV together.

REFERENCES

[1] Z. Qin, X. Zhang, X. Zhang, B. Lu, Z. Liu, and L. Guo, "The uav trajectory optimization for data collection from time-constrained iot devices: A hierarchical deep q-network approach," Applied Sciences, vol. 12, no. 5, pp. 2546, 2022.

[2] Bithas, P.S., Michailidis, E.T., Nomikos, N., Vouyioukas, D. and Kanatas, A.G., 2019. A survey on machine-learning techniques for UAV-based communications. Sensors, vol. 19, no. 23, pp.5170.

[3] H. Bayerlein, M. Theile, M. Caccamo, and D. Gesbert, "Multi-UAV path planning for wireless data harvesting with deep reinforcement learning," IEEE Open Journal of the Communications Society, vol. 2, pp. 1171–1187, 2021.

[4] Y. Yao, Z. Zhu, S. Huang, X. Yue, C. Pan, and X. Li, "Energy efficiency characterization in heterogeneous iot system with uav swarms based on wireless power transfer," IEEE Access, vol. 8, pp. 967–979, 2019.

[5] Z. Wang and J. Cai, "Probabilistic roadmap method for path-planning in radioactive environment of nuclear facilities," Progress in Nuclear Energy, vol. 109, pp.113–120, 2018.

[6] A. Upadhyay, K. R. Shrimali, and A. Shukla, "Uav-robot relationship for coordination of robots on a collision free path," Procedia Computer Science, vol. 133, pp. 424–431, 2018.

[7] F. Yan, Y.-S. Liu, and J.-Z. Xiao, "Path planning in complex 3d environments using a probabilistic roadmap method," International Journal of Automation and computing, vol. 10, no. 6, pp. 525–533, 2016.

[8] S. Jain, R. C. Shah, W. Brunette, G. Borriello, and S. Roy, "Exploiting mobility for energy efficient data collection in wireless sensor networks," Mobile networks and Applications, vol. 11, no. 3, pp. 327–339, 2006.

[9] C.S. Choi and F. Baccelli, "Spatial and temporal analysis of direct communications from static devices to mobile vehicles," IEEE Transactions on Wireless Communications, vol. 18, no. 11, pp. 5128–5140, 2019.

[10] R. Marini, L. Spampinato, S. Mignardi, R. Verdone, and C. Buratti, "Reinforcement learning-based trajectory planning for uav-aided vehicular communications," 2022 30th European Signal Processing Conference (EUSIPCO), IEEE, pp. 967–971, 2022.

[11] A. Kaplan, N. Kingry, P. Uhing, and R. Dai, "Time-optimal path planning with power schedules for a solar-powered ground robot," IEEE Transactions on Automation Science and Engineering, vol. 14, no. 2, pp. 1235–1244, 2006.

[12] M. R. Jabbarpour, H. Zarrabi, J. J. Jung, and P. Kim, "A green ant-based method for path planning of unmanned ground vehicles," IEEE access, vol. 5, pp. 1820–1832, 2017.

[13] E. Almoaili and H. Kurdi, "Path planning algorithm for unmanned ground vehicles (ugvs) in known static environments," Procedia Computer Science, vol. 177, pp. 57–63, 2020.

[14] Y.-C. Wang and K.-C. Chen, "Efficient path planning for a mobile sink to reliably gather data from sensors with diverse sensing rates and limited buffers," IEEE Transactions on Mobile Computing, vol. 18, no. 7, pp. 1527–1540, 2018.

[15] D. Liu, S. Wang, Z. Wen, L. Cheng, M. Wen, and Y.-C. Wu, "Edge learning with unmanned ground vehicle: Joint path, energy, and sample size planning," IEEE Internet of Things Journal, vol. 8, no. 4, pp. 2959–2975, 2020.

[16] A. T. Azar, A. Koubaa, N. Ali Mohamed, H. A. Ibrahim, Z. F. Ibrahim, M. Kazim, A. Ammar, B. Benjdira, A. M. Khamis, I. A. Hameed, et al., "Drone deep reinforcement learning: A review," Electronics, vol. 10, no. 9, pp. 999, 2021.

[17] K. Arulkumaran, M. P. Deisenroth, M. Brundage, and A. A. Bharath, "Deep reinforcement learning: A brief survey," IEEE Signal Processing Magazine, vol. 34, no. 6, pp. 26–38, 2017.

[18] C. J. C. H. Watkins, Learning from delayed rewards. King's College, May 1989.

[19] M. Kusy and R. Zajdel, "Stateless Q-Learning algorithm for training of radial basis function based neural networks in medical data classification," Advances in Intelligent Systems and Computing, vol. 230, pp. 267–278, 2014.

[20] C. J. C. H. Watkins and P. Dayan, "Q-learning," Machine learning, vol. 8, pp. 279-292, 1992.

[21] S. Bhatnagar, R. S: Sutton, M. Ghavamzadeh, and M. Lee, "Incremental Natural Actor-Critic Algorithms," NeurIPS, pp. 729-736, 1993.

[22] R. S. Sutton and A. G. Barto, "Reinforcement learning: An introduction," MIT press, 2018.

[23] Y. Hu, D. Li, Y. He, and J. Han, "Incremental Learning Framework for Autonomous Robots Based on Q-Learning and the Adaptive Kernel Linear Model," in IEEE Transactions on Cognitive and Developmental Systems, vol. 14, no. 1, pp. 64-74, March 2022.

[24] V. Mnih, et al, "Human-level control through deep reinforcement learning. Nature, vol. 518, no. 7540, pp. 529-533, 2015.

[25] J. Zhu, Y. Song, D. Jiang and H. Song, "A New Deep-Q-Learning-Based Transmission Scheduling Mechanism for the Cognitive Internet of Things," in IEEE Internet of Things Journal, vol. 5, no. 4, pp. 2375-2385, Aug. 2018.

[26] X. Zhou, W. Liang, K. I. -K. Wang, H. Wang, L. T. Yang and Q. Jin, "Deep-Learning-Enhanced Human Activity Recognition for Internet of Healthcare Things," in IEEE Internet of Things Journal, vol. 7, no. 7, pp. 6429-6438, July 2020.

[27] A. Weissensteiner, "A Q-Learning Approach to Derive Optimal Consumption and Investment Strategies," in IEEE Transactions on Neural Networks, vol. 20, no. 8, pp. 1234-1243, Aug. 2009

[28] M. Ye, C. Tianqing and F. Wenhui, "A single-task and multi-decision evolutionary game model based on multi-agent reinforcement learning," in Journal of Systems Engineering and Electronics, vol. 32, no. 3, pp. 642-657, June 2021

[29] Z. Xiaochuan, W. Wanwan, L. Qin, W. Tianao and S. Hao, "The Design and Realization of Dynamic Evaluation Strategy of Pieces in Military Chess Game System," 2019 Chinese Control And Decision Conference (CCDC) pp. 6287-6292, Nanchang, China, 2019.

[30] T. N. Larsen, H. Ø. Teigen, T. Laache, D. Varagnolo, and A. Rasheed, "Comparing deep reinforcement learning algorithms' ability to safely navigate challenging waters," Frontiers in Robotics and AI 8.

BIOGRAPHIES

Erdal AKIN was born in Ceyhan, Adana, Turkey. He graduated from the Department of Mathematics, Yildiz Technical University, Istanbul, in 2008. In 2009, he received the Republic of Turkey Ministry of National Education scholarship to study in the USA. He received master's and Ph.D. degrees from the Department of Computer Science, The University of Texas at San Antonio (UTSA), in the Spring of 2014 and December 2018, respectively. His research interests are Deep Reinforcement Learning, Software Defined Networks, Security, and Blockchain.

Yakup SAHIN was born in Adana, Turkey, in 1986. He received his B.S. degree in electrical and electronics engineering from İnönü University, Malatya, Turkey, in 2010, and his M.S. and Ph.D. degrees in electrical engineering from Yıldız Technical University, Istanbul, Turkey, in 2013 and 2016, respectively. He worked as a Research Assistant from 2011 to 2016 in the Department of Electrical Engineering at Yıldız Technical University. He served as an Assistant Professor from 2016 to 2021 and is currently an Associate Professor in the Department of Electrical and Electronics Engineering at Bitlis Eren University. He has authored or co-authored more than 50 technical papers published in journals and conference proceedings. Additionally, he has been involved in 9 research projects related to power electronics. His current research interests include DC-DC and DC-AC power converter topologies, high-frequency soft-switching converters, power factor correction, switching power supplies, and bidirectional converters.

European Journal of Technique

journal homepage: https://dergipark.org.tr/en/pub/ejt

Vol.13, No.1, 2023

Optimum Design and Control of a Quick-Return Mechanism Used in a Jewelry Welding Powder Production Machine

Osman YİĞİD[1*], Murat ŞEN[2]

[1*]Firat University, Mechanical Engineering Department, 23119, Elazig, Türkiye. (e-mail: yigidosman@gmail.com).

[2] Firat University, Mechanical Engineering Department, 23119, Elazig, Türkiye. (e-mail: msen@firat.edu.tr).

ARTICLE INFO

Received: Sep., 27. 2022
Revised: Feb., 20. 2023
Accepted: Feb., 21. 2023

Keywords:
Quick-return mechanism
Sliding mode control
Jewelry welding powder
Optimum design

Corresponding author: *Osman YİĞİD*

ISSN: *2536-5010* | e-ISSN: *2536-5134*

DOI: https://doi.org/10.36222/ejt.1181023

ABSTRACT

The movement of the machines used in the industry is generally driven by an electric motor. The rotational motion of the electric motor is transferred to the mechanism, and while the kinematic and dynamic analyzes of the mechanism are performed, it is considered that the input link (crank) of the mechanism to which the rotational motion of this motor is transferred rotates with a constant angular velocity. However, the inertia forces and moments created by all the other links of the mechanism prevent the crank from rotating with a constant angular velocity. To eliminate this problem, the angular velocity of the crank must be controlled using an appropriate control method. In this study, the optimum design of the quick return mechanism in a welding powder production machine to be used in the jewelry manufacturing industry has been made within the scope of some specified constraints. Then, the dynamic equations of the mechanism were obtained utilizing the Eksergian's Equations of Motion method and the sliding mode control method was used to ensure that the crank rotates with a constant angular velocity. In this way, it is aimed to obtain a more standard size jewelry welding powder.

1. INTRODUCTION

Quick-return mechanisms are widely used in mechanical engineering applications like cutting and shaping machines etc. These mechanisms are designed so that the forward movement with the intended work is slow (mostly cutting stroke) and the return movement without the work is faster (return stroke). In this way, efficiency can be achieved by shortening the idle time while the mechanism is running. The round trip ratio is known as TR (time ratio) in the mechanism and always has a value greater than 1 due to construction.

The movement of the mechanisms used in the industry is generally provided by using an electric motor and this motor is required to rotate the input link of the mechanism with a constant speed and all designs and analyzes of the mechanisms are made accordingly. However, due to the external forces and inertia forces that may occur during the operation of the mechanisms, it becomes difficult for the crank to rotate at a constant speed. In order to eliminate this problem, some machine elements that will create a flywheel effect can be used in mechanisms. However, as a result of advances in electronics and programming technology, by using different control methods, the motor can be provided to rotate the input link of the mechanism at a constant speed. Researchers are working to develop effective methods in this context. Fung and Chen [1], presented a study to control the crank constant velocity of a quick-return mechanism driven by a DC motor based on PID (Proportional Integral Derivative) controller. They used Hamilton's principle and Lagrange multiplier method to formulate the mechanism for dynamic analysis. They obtained good results for numerical simulations with or without applying cutting force to the system. El-Kribi et al. [2], made a multi-objective optimization study with continuous and discrete variables to minimize the motor torque and velocity fluctuation of a four-bar mechanism by using genetic algorithm. Tao and Sadler [3], made a control study on a four-bar mechanism for reducing the crank angular fluctuation by using PID control method. They used numerical optimization methods to obtain the control gains of the controller. Ha et al. [4], presented an identification method based on real-coded genetic algorithm for identifying the parameters of a slider-crank mechanism. Wai and Lin [5], controlled a slider-crank mechanism by using fuzzy neural network controller with adaptive learning rates utilizing analytical methods based on discrete type Lyapunov function. Lin and Wai [6], presented a fuzzy neural network sliding mode controller to obtain much less tracking error for the position control of motor-quick-return servomechanism. They showed the effectiveness of the presented method with the comparison of adaptive sliding mode controller with some

simulations and experimental studies. Ouyang et al. [7], presented a study on a five bar hybrid machine system consisted of a constant speed motor and a servomotor for a constant velocity trajectory profile. They used extra mechanical flywheel to reduce the speed fluctuations for better performance. Gündoğdu and Erentürk [8], made a control simulation study of a four bar mechanism by using fuzzy logic controller and compared the results with an optimal PID controller. Affi et al. [9], presented a multi-objective optimization of a motor-driven four-bar mechanism considering the geometry and the dynamics of the system together. Yan and Yan [10], proposed an approach for designing the variable input speed servo four bar mechanism based on an integrated mechanism and controller design with dimensions of the links, the counterweights, input speed trajectory and controller parameters as design variables. Tanyıldızı and Çakar [11], used sliding mode control and moving sliding mode control algorithms to control the angular velocity of the crank of a slider-crank mechanism. They investigated the robustness of the control algorithms by applying a nonlinear force to the system. In another study, Çakar and Tanyıldızı [12], studied the same control algorithms to control the crank angular velocity fluctuations of a four bar mechanism with the presentation of simulation and experimental applications.

In this study, the optimum design of a quick-return mechanism in a welding powder production machine used in the jewelry industry has been made and the dynamic equations of the mechanism have been obtained by the Eksergian's Equations of Motion method. In addition, the motor to which the crank is connected was controlled with the sliding mode control method in order for the crank, on which the mechanism is driven, to rotate with a constant speed to provide more standard size jewelry welding powder.

2. OPTIMUM DESIGN OF THE QUICK RETURN MECHANISM

While designing any machine, it is desired that the designed machine should have optimum features in terms of efficiency and cost while fulfilling the specified functions. The features such as the maximum work of the machine in minimum volume, high mechanical advantage and being economical in terms of cost must be taken into consideration. In this context, an optimization study has been carried out to ensure that the mechanism designed in this study is in optimum dimensions, taking into account some of the constraints determined. The representation of the designed machine and the schematic of the mechanism are given in Figure 1.

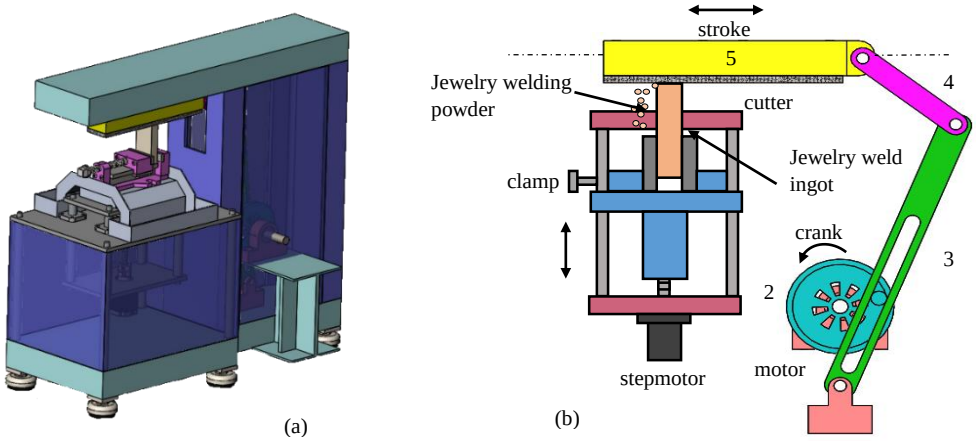

Figure 1. a) Jewelry welding powder production machine design, b) Quick-return mechanism of the machine

The mechanism, schematically illustrated in Figure 1.b, is designed to produce welding powder used in the jewelry manufacturing industry. The mechanism is driven by the crank (link 2) connected to the shaft of an electric motor. A cutter unit that forms welding powder is attached to the output link (link 5) of the mechanism, where linear motion is obtained. In this way, while welding powder is produced in the forward movement of the link 5 of the mechanism, no work is done on the return cycle and this period is completed quickly.

The produced welding powder and it's usage in a filigree application are depicted in Figure 2.a and Figure 2.b respectively.

Figure 2. a) Jewelry welding powder, b) jewelry welding powder operation

Jewelry welding powder is used especially in filigree type designed jewelries or crafted object applications. Some examples of crafted objects using this type of welding powder are shown in Figure 3.

Figure 3. Filigree silver objects in which jewelry welding powder is used

The design parameters of the mechanism are r_2 (x_1), r_3 (x_2), r_4 (x_3), a (x_4) and b (x_5) as seen in Figure 4.

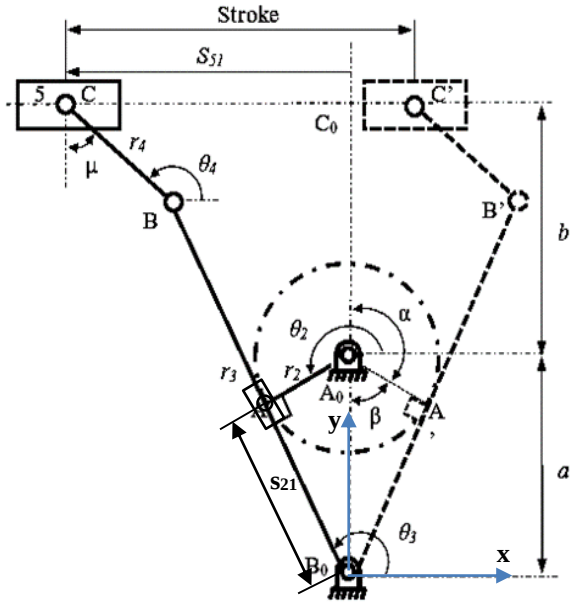

Figure 4. The kinematic diagram of quick-return mechanism

The objective function is:

$$f_{obj} = min(x_1 + x_2 + x_3 + x_4 + x_5) \tag{1}$$

The design constraints of the mechanism are given below, where all lengths are in (mm).

$$\begin{aligned}
&c_1 ; x_1 < x_4 \\
&c_2 ; 200 < x_4 + x_5 < 500 \\
&c_3 ; 250 < 2x_2 \sin\theta_3 < 350 \\
&c_4 ; 250 < 2x_2 \sin\theta_3 + x_3 \sin\theta_4 < 500 \\
&c_5 ; 45^\circ < \mu < 55^\circ \\
&c_6 ; 1.5 < TR < 2
\end{aligned} \tag{2}$$

Here, μ is the transmission angle and TR is time ratio of the mechanism. For the optimization of the mechanism Matlab *fmincon* algorithm was used. The determined optimum design parameters and related physical parameters i.e. lengths (r), masses (m) and moment of inertias (I) of the links are given in Table 1.

TABLE I
DETERMINED DESIGN PARAMETERS AND THE PHYSICAL PARAMETERS OF THE MECHANISM

	r (mm)	m (kg)	I (kgm^2)*10^{-4}
r_2	54	0.35	8.95
r_3	324	0.32	53
r_4	78	0.36	8.5
s_{51}	-	1	-
a	140	-	-
b	207	-	-

3. EQUATIONS OF MOTION OF THE MECHANISM

The kinematic equations can be obtained by using vector loops for the mechanism given in Figure 4 as below:

$$\begin{aligned}
&\mathbf{B_0A = B_0A_0 + A_0A} \\
&s_{21}e^{i\theta_3} = ia + r_2 e^{i\theta_2}
\end{aligned} \tag{3}$$

$$\begin{aligned}
&\mathbf{B_0B + BC = B_0C_0 + C_0C} \\
&r_3 e^{i\theta_3} + r_4 e^{i\theta_4} = i(a+b) - s_{51}
\end{aligned} \tag{4}$$

By using Equations (3-4) one can obtain the following equations in complex plane.

$$
\begin{aligned}
&s_{21}\left(\cos\theta_3 + i\sin\theta_3\right) = ia + r_2\left(\cos\theta_2 + i\sin\theta_2\right)\\
&\text{real}: s_{21}\cos\theta_3 - r_2\cos\theta_2 = 0\\
&\text{imag}: s_{21}\sin\theta_3 - a - r_2\sin\theta_2 = 0
\end{aligned}
\tag{5}
$$

$$
\begin{aligned}
&r_3\left(\cos\theta_3 + i\sin\theta_3\right) + r_4\left(\cos\theta_4 + i\sin\theta_4\right)\\
&= i\left(a+b\right) - s_{51}\\
&\text{real}: r_3\cos\theta_3 + r_4\cos\theta_4 + s_{51} = 0\\
&\text{imag}: r_3\sin\theta_3 + r_4\sin\theta_4 - a - b = 0
\end{aligned}
\tag{6}
$$

Here, s_{21} in Equation (5) can be cancelled as:

$$
\frac{s_{21}\sin\theta_3}{s_{21}\cos\theta_3} = \tan\theta_3 = \frac{a + r_2\sin\theta_2}{r_2\cos\theta_2} \tag{7}
$$

By rearranging Equations (6-7), the constraint equations of the mechanism can be written as follows:

$$
\begin{aligned}
f_1\left(\theta_2,\theta_3,\theta_4,s_{51}\right) &= r_2\sin\theta_3\cos\theta_2\\
&\quad - \cos\theta_3\left(a + r_2\sin\theta_2\right) = 0\\
f_2\left(\theta_2,\theta_3,\theta_4,s_{51}\right) &= r_3\cos\theta_3 + r_4\cos\theta_4 + s_{51} = 0\\
f_3\left(\theta_2,\theta_3,\theta_4,s_{51}\right) &= r_3\sin\theta_3 + r_4\sin\theta_4 - (a+b) = 0
\end{aligned}
\tag{8}
$$

The independent generalized coordinate (q) and the dependent coordinates (ϕ_1, ϕ_2, and ϕ_3) of the mechanism are presented as follows:

$$
\theta_2 = q;\quad \theta_3 = \phi_1;\quad \theta_4 = \phi_2;\quad s_{51} = \phi_3 \tag{9}
$$

The first order influence coefficients can be calculated by using Equation (8), where J is the Jacobian matrix and f is constraint equations vector which are calculated as shown below.

$$
g = -J^{-1}f' \tag{10}
$$

$$
f' = \left\{\frac{\partial f_1}{\partial q}\quad \frac{\partial f_2}{\partial q}\quad \frac{\partial f_3}{\partial q}\right\}^T = \left\{r_2\cos(q-\phi_1)\quad 0\quad 0\right\}^T \tag{11}
$$

$$
J = \begin{bmatrix}
\frac{\partial f_1}{\partial \phi_1} & \frac{\partial f_1}{\partial \phi_2} & \frac{\partial f_1}{\partial \phi_3}\\
\frac{\partial f_2}{\partial \phi_1} & \frac{\partial f_2}{\partial \phi_2} & \frac{\partial f_2}{\partial \phi_3}\\
\frac{\partial f_3}{\partial \phi_1} & \frac{\partial f_3}{\partial \phi_2} & \frac{\partial f_3}{\partial \phi_3}
\end{bmatrix} = \begin{bmatrix}
\frac{r_2\cos q}{\cos^2\phi_1} & 0 & 0\\
-r_3\sin\phi_1 & -r_4\sin\phi_2 & 1\\
r_3\cos\phi_1 & r_4\cos\phi_2 & 0
\end{bmatrix} \tag{12}
$$

The first order influence coefficients then can be obtained as follows:

$$
g = \begin{Bmatrix} g_1\\ g_2\\ g_3 \end{Bmatrix} = \left\{\begin{array}{c}
\frac{r_2\cos(q-\phi_1)}{D}\\
-\frac{r_2 r_3\cos(q-\phi_1)\cos\phi_1}{r_4\cos\phi_2 D}\\
\frac{r_2 r_3\cos(q-\phi_1)\sin(\phi_1-\phi_2)}{\cos\phi_2 D}
\end{array}\right\} \tag{13}
$$

Here, $D = a\sin(\phi_1) + r_2\cos(q-\phi_1)$. By using first order influence coefficients the velocities of the dependent links can be calculated with following equation.

$$
\dot{\phi}_i = g_i\dot{q} \quad \left(i = 1,2,3\right) \tag{14}
$$

The velocity of the center of gravity for the links can be expressed with the first order influence coefficient;

$$
\begin{aligned}
&v_{G_i} = \left(\sqrt{v_{G_i}^{x\,2} + v_{G_i}^{y\,2}}\right)\dot{q};\\
&v_{G_i}^x = \frac{\partial x_i}{\partial q} + \sum_{j=1}^{3}\frac{\partial x_i}{\partial \phi_j}g_j;\quad v_{G_i}^y = \frac{\partial y_i}{\partial q} + \sum_{j=1}^{3}\frac{\partial y_i}{\partial \phi_j}g_j
\end{aligned}
\tag{15}
$$

$$
\begin{aligned}
v_{G_2}^x &= -c_2\sin q\\
v_{G_2}^y &= c_2\cos q\\
v_{G_3}^x &= \left(-c_3\sin\phi_1\right)g_1\\
v_{G_3}^y &= \left(c_3\cos\phi_1\right)g_1\\
v_{G_4}^x &= -\left(r_3\sin\phi_1\right)g_1 - \left(c_4\sin\phi_2\right)g_2\\
v_{G_4}^y &= \left(r_3\cos\phi_1\right)g_1 + \left(c_4\cos\phi_2\right)g_2\\
v_{G_5}^x &= -\left(r_3\sin\phi_1\right)g_1 - \left(r_4\sin\phi_2\right)g_2\\
v_{G_5}^y &= 0
\end{aligned}
\tag{16}
$$

The second order influence coefficient can be obtained by using Equation (17) as:

$$
g_i' = \frac{\partial g_i}{\partial q} + \sum_{j=1}^{3}\frac{\partial g_i}{\partial \phi_j}g_j \quad \left(i = 1,2,3\right) \tag{17}
$$

$$
g_1' = -\frac{a r_2\left[g_1\cos q + \sin(q-\phi_1)\sin\phi_1\right]}{D^2} \tag{18}
$$

$$
\begin{aligned}
g_2' = &\frac{r_2 r_3\left[\begin{array}{l} a\cos(q-\phi_1) - a\sin(q-\phi_1)\sin\phi_1\cos\phi_1\\ +r_2\cos^2(q-\phi_1)\sin\phi_1\end{array}\right]}{r_4\cos\phi_2 D^2}g_1\\
&-\frac{r_2 r_3\cos(q-\phi_1)\cos\phi_1\sin\phi_2}{r_4\cos^2\phi_2 D}g_2\\
&+\frac{a r_2 r_3\sin(q-\phi_1)\cos\phi_1\sin\phi_1}{r_4\cos\phi_2 D^2}
\end{aligned}
\tag{19}
$$

$$g_3' = -\frac{r_2 r_3 \begin{bmatrix} r_2 \cos^2(q-\phi_1)\cos(\phi_1-\phi_2) \\ +a\cos(q-\phi_1)\cos(\phi_1-\phi_2)\sin\phi_1 \end{bmatrix}}{\cos\phi_2 D^2} g_1$$
$$-\frac{ar_2 r_3 \begin{bmatrix} \cos(q-\phi_1)\sin(\phi_1-\phi_2)\cos\phi_1 \\ +a\sin(q-\phi_1)\sin(\phi_1-\phi_2)\sin\phi_1 \end{bmatrix}}{\cos\phi_2 D^2} g_1$$
$$-\frac{r_2 r_3(\cos(q-2\phi_1)+\cos\phi_1)}{(\cos(2\phi_2)+1)D} g_2$$
$$-\frac{ar_2 r_3 \sin(q-\phi_1)\sin(\phi_1-\phi_2)\sin\phi_1}{\cos\phi_2 D^2} \quad (20)$$

By using second order influence coefficients the accelerations of the dependent links can be calculated as follows:

$$\ddot{\phi}_i = g_i'\dot{q}^2 + g_i\ddot{q} \quad (i=1,2,3) \quad (21)$$

The acceleration of the center of gravity for the links can be expressed with the influence coefficients as:

$$a_{G_i} = \left(\sqrt{a_{G_i}^{x\,2} + a_{G_i}^{y\,2}}\right)\dot{q}^2 + \left(\sqrt{v_{G_i}^{x\,2} + v_{G_i}^{y\,2}}\right)\ddot{q}$$
$$a_{G_i}^x = \frac{\partial v_{G_i}^x}{\partial q} + \sum_{j=1}^{3}\frac{\partial v_{G_i}^x}{\partial \phi_j} g_j \;;\; a_{G_i}^y = \frac{\partial v_{G_i}^y}{\partial q} + \sum_{j=1}^{3}\frac{\partial v_{G_i}^y}{\partial \phi_j} g_j \quad (22)$$

$$a_{G_2}^x = -c_2\cos q$$
$$a_{G_2}^y = -c_2\sin q$$
$$a_{G_3}^x = -c_3\cos\phi_1 g_1^2 + \sin\phi_1 g_1'$$
$$a_{G_3}^y = -c_3\sin\phi_1 g_1^2 - \cos\phi_1 g_1'$$
$$a_{G_4}^x = -r_3\cos\phi_1 g_1^2 - c_4\cos\phi_2 g_2^2 - c_4\sin\phi_2 g_2' - r_3\sin\phi_1 g_1' \quad (23)$$
$$a_{G_4}^y = -r_3\sin\phi_1 g_1^2 - c_4\sin\phi_2 g_2^2 + c_4\cos\phi_2 g_2' + r_3\cos\phi_1 g_1'$$
$$a_{G_5}^x = -r_3\sin\phi_1 g_1^2 - r_4\cos\phi_2 g_2^2 - r_3\sin\phi_1 g_1' - r_4\sin\phi_2 g_2'$$
$$a_{G_5}^y = 0$$

The kinetic energy of the mechanism can be written as:

$$E_k = \frac{1}{2}\sum_i \left(m_i g_i'^2 + I_{G_i} g_{\theta_i}'^2\right)\dot{q}^2 \quad (i=1,2,3) \quad (24)$$

Equivalent inertia is

$$\Im = \sum_i \left(m_i g_i'^2 + I_{G_i} g_{\theta_i}'^2\right) \quad (i=1,2,3) \quad (25)$$

Equivalent force including gravity, cutting and friction forces and torques can be expressed as:

$$\mathbf{Q} = \sum_i \left(\mathbf{F}_i g_i' + \mathbf{T}_i g_{\theta_i}'^2\right) \quad (i=1,2,3) \quad (26)$$

For any mechanism, reducing the inertia of all links to the input link provides great convenience in terms of controllability of the mechanism. The generalized equation of motion of any reduced mechanism is given by Paul [13],

$$\Im\ddot{q} + C\dot{q}^2 = Q \quad (27)$$

Where C is called centripetal coefficient and calculated as:

$$C = \frac{1}{2}\frac{d\Im}{dq} \quad (28)$$

The mathematical model and the output torque of a DC motor with a reducer can be written as:

$$\frac{di_m}{dt} = \frac{1}{L_m}\left(V_m - R_m i_m - nK_g\dot{q}\right) \quad (29)$$

$$T_o = n\left(-nJ\ddot{q} - nB\dot{q} + K_m i_m - T_f\right) \quad (30)$$

Where i_m, L_m, V_m, R_m, K_g, J, B, K_m, T_f and n are the current, inductance, input voltage, resistance, motor voltage constant, mass moment of inertia, viscous damping, motor torque constant motor torque losses and reducer speed ratio respectively.

The only torque acting on the mechanism is T_0 applied to the crank. With calling all the available external forces as Q_0, then Q becomes,

$$Q = Q_0 + T_0 \quad (31)$$

By rearranging the Equations (26-31), one can obtain the following equation

$$\ddot{q} = \frac{-n^2 B_m\dot{q} - C\dot{q}^2 + nK_m i_m - nT_f + Q_0}{\Im + n^2 J} \quad (32)$$

The state space equations are expressed as:

$$z_1 = q;\; z_2 = \dot{q};\; z_3 = i_m \quad (33)$$

$$\dot{z}_1 = z_2$$
$$\dot{z}_2 = \frac{-n^2 B_m z_2 - C z_2^2 + nK_m z_3 - nT_f + Q_0}{\Im + n^2 J} \quad (34)$$
$$\dot{z}_3 = \frac{1}{L_m}\left(V_m - R_m z_3 - nK_g z_2\right)$$

4. CONTROLLER DESIGN

Sliding mode control is an extremely robust control technique that can provide the desired dynamic behavior despite the uncertainties, parameter changes and disturbances in the physical systems. Since it is an effective control method and easy to implement, it is widely used in many control studies. With the development of switching technology, its popularity and usage area has developed considerably.

In this study, the sliding mode control technique was used to rotate the crank of the presented mechanism, which was designed optimally, at a constant speed. The block diagram and equations of this control method are given below (Figure 5).

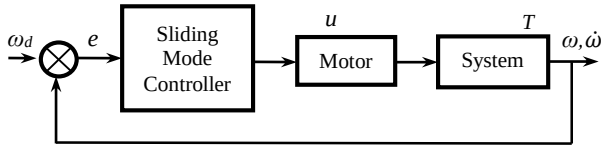

Figure 5. Sliding mode controller block diagram

In Fig. 5 ω_d, u, T, ω and $\dot{\omega}$ are the desired angular velocity of the crank, control signal, torque, output velocity and acceleration of the crank respectively.

The sliding surface s of the controller is defined as:

$$s(x,t) = \lambda e_1(t) + e_2(t) \tag{35}$$

Here, λ is the slope of the sliding surface, e_1 and e_2 represent the tracking errors which are given below.

$$\begin{aligned} e(t) &= \left[e_1(t) \quad e_2(t) \right] \\ &= \left[\omega_1(t) - \omega_{1d}(t) \quad \dot{\omega}_1(t) - \dot{\omega}_{1d}(t) \right] \end{aligned} \tag{36}$$

The control signal (voltage supplied to DC motor) of the sliding mode controller system is obtained as:

$$\begin{aligned} u(t) = &\left[\begin{array}{l} \left(-\lambda \left(\Im + J \right) \dot{e}_1 + B_m z_2 + T_f - Q_0 + C z_2^2 \right) \dfrac{R_m}{K_m} \\ + K_g z_2 + L_m \dot{z}_3 \end{array} \right] \\ &- K sign(s) \end{aligned} \tag{37}$$

Here, K is a positive constant and usually determined with trial error method. The control simulations in this study were made by using Matlab software. The physical parameters of the DC motor used in simulation were taken from ref. [1] as given in Table 2.

TABLE II
THE PHYSICAL PARAMETERS OF THE DC MOTOR

Parameter	K_g (Vs/rad)	R_m (Ω)	B_m (Nms/rad)	K_m (Nms/A)	Lm (H)	J(kgm²)
Value	0.678	0.4	0.226	0.678	0.05	0.0565

The crank of the mechanism is supposed to rotate with a constant angular velocity of 5 rad/s. While applying constant input voltage of 48 V with a transmission ratio of 10 the output angular velocity of the crank fluctuates between 6.1-6.4 rad/s (Fig. 6). The small peaks after settling time are due to cutting force interactions. After applying sliding mode control its fluctuations are reduced significantly. In control applications, K and λ are determined as 1000 and 50 respectively. The cutting force is supposed to be 50 N. The steady state error of crank velocity is calculated as 0.2% (zoomed area of Figure 6). Input voltage is bounded between -48 V and +48 V. A section of input voltage is given in Figure 7.

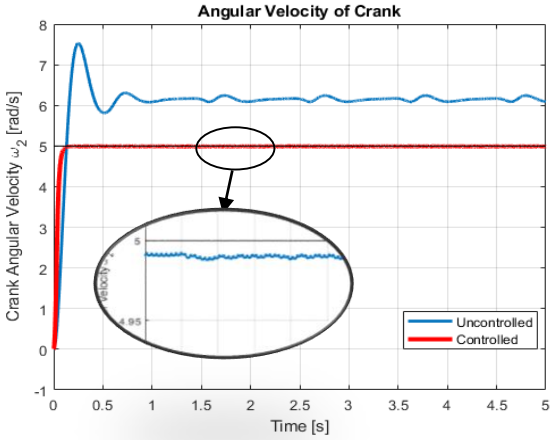

Figure 6. Crank angular velocity

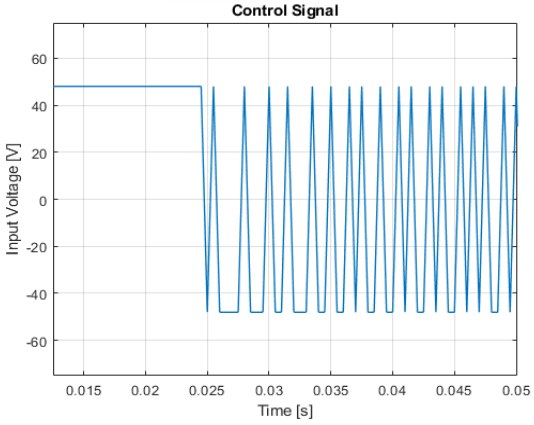

Figure 7. Input signal

5. CONCLUSION

In this study, an optimum design and control of a quick return mechanism used in a jewelry welding powder production machine are presented. For optimum design of the mechanism with a cost function, some constraints as transmission angle, time ratio and lengths of the links of the mechanism were defined with design variables. Matlab fmincon algorithm was used for the optimization and minimum lengths of the mechanism were determined. For obtaining the equation of motion of the mechanism Eksergian's Equation of Motion method was used and all the inertias of the mechanism were reduced on the crank. For controlling the crank of the mechanism in constant angular velocity sliding mode control method was used. After the controlling, the fluctuation of the angular velocity of the crank was reduced to admissible level.

REFERENCES

[1] R. F. Fung, K. W. Chen, "Constant speed control of the quick return mechanism driven by a DC motor," JSME International Journal 1997; 40(3).

[2] B. El-Kribi, A. Houidi, Z. Affi, L. Romdhane, "Application of multi-objective genetic algorithms to the mechatronic design of

a four bar system with continuous and discrete variables," Mechanism and Machine Theory 2013; 61, 68–83.

[3] J. Tao, J. P. Sadler, "Constant speed control of a motor driven mechanism system," Mechanism and Machine Theory 1995; 30(5), 737-748.

[4] J. L. Ha, R. F. Fung, K. Y. Chen, S. C. Hsien, "Dynamic modeling and identification of a slider-crank mechanism," Journal of Sound and Vibration 2006; 289, 1019-1044.

[5] R. J. Wai, F. J. Lin, "A fuzzy neural network controller with adaptive learning rates for nonlinear slider-crank mechanism," Neuocomputing 1998; 20, 295-320.

[6] F. J. Lin, R. J. Wai, "Adaptive and fuzzy neural network sliding-mode controllers for motor-quick-return servomechanism," Mechatronics 2003; 13, 477-506.

[7] P. R. Ouyang, Q. Li, W. J. Zhang, L. S. Guo, "Design, modeling and control of a hybrid machine system," Mechatronics 2004; 14, 1197-1217.

[8] Ö. Gündoğdu, K. Erentürk, "Fuzzy control of a dc motor driven four-bar mechanism," Mechatronics 2005; 15, 423-438.

[9] Z. Affi, B. El-Kribi, L. Romdhane, "Advanced mechatronic design using a multi-objective genetic algorithm optimization of a motor-driven four-bar system," Mechatronics 2007; 17, 489-500.

[10] H. S. Yan, G. J. Yan, "Integrated control and mechanism design for the variable input-speed servo four-bar linkages," Mechatronics 2009; 19, 274-287.

[11] A. K. Tanyıldızı, O. Çakar, "Velocity control of a slider crank mechanism using moving sliding mode control," 15. Ulusal Makine Teorisi Sempozyumu 2011; 449-457.

[12] O. Çakar, A. K. Tanyıldızı, "Application of moving sliding mode control for a DC motor driven four-bar mechanism," Advances in Mechanical Engineering 2018; 103, 1-13.

[13] P Burton, "Kinematics and dynamics of planar machinery," Upper Saddle River, NJ: Prentice Hall, 1979.

BIOGRAPHIES

Osman Yiğid is Research Assistant in Mechanical Engineering Department at Firat University, Elazig, Türkiye. He received his MSc. degree from Northeastern University, Boston, USA. He is continuing his PhD. at Firat University. His research interests include particle damping, structural dynamics, vibration analysis, machine design, machine theory and dynamics.

Murat Şen is Dr. Research Assistant in Mechanical Engineering Department at Firat University, Elazig, and Türkiye. He received his PhD.in Mechanical Engineering from Fıirat University. His research interests include structural dynamics, vibration analysis, machine theory and dynamics, rotordynamics and machine design.